Quantum Hall states in the Harper-Hofstadter model:
existence, stability and novel phase transitions

A thesis submitted for the degree of
Doctor of Philosophy

Author:
Leon SCHOONDERWOERD

Supervisor:
Dr. Gunnar Möller

University of Kent
School of Physical Sciences
United Kingdom

September 2020

Declaration

I declare that the content of this thesis, titled "Quantum Hall states in the Harper-Hofstadter model: existence, stability and novel phase transitions" is entirely my own, and has not been submitted for the purposes of a qualification at any other institution or for any other degree. The content comprising chapters 5 and 6 has been adapted and extended from Schoonderwoerd, Pollmann, and Möller (2019). All data is my own, unless explicitly stated otherwise. All instances where use has been made of other work have been cited.

Signed: Leon SCHOONDERWOERD

Date: 30 September 2020

Abstract

The quantum Hall effect (QHE) (chapter 2) describes the quantisation of the Hall conductivity (conductivity perpendicular to external magnetic and electric fields in a two-dimensional sample) and related observables such as conductivity and resistivity. The search for a theoretical description of quantum Hall (QH) physics has been an important driver of developments in theoretical physics, leading to the development of topological concepts in condensed matter physics. A vast 'zoo' of different QH states have been described.

The Harper-Hofstadter model (chapter 4) describes particles on a two-dimensional lattice, subject to a magnetic field. It is widely known for its fractal energy spectrum, the 'Hofstadter butterfly'. The model, under addition of interaction terms, supports a range of exotic many-body states, including integer and fractional QH and Chern insulator (CI) states.

In this thesis, we study fractional quantum Hall (FQH) states, and their lattice analogues known as fractional Chern insulator (FCI) states, as occurring in the Harper-Hofstadter model using Matrix Product States (MPSs) and the Density Matrix Renormalization Group (DMRG) (chapter 3). In particular, we focus on FQH states supported on the lowest 'tail' of the Hofstadter butterfly, at flux densities n_ϕ where this tail consists of multiple sub-bands.

We demonstrate the existence and stability of the $\nu = 1/3$ Laughlin state over a range of n_ϕ (where the lowest Landau level (LLL) consists of multiple magnetic sub-bands) in chapter 5. Along the way, we improve on the method commonly used in literature for the extrapolation of the entanglement entropy to find the topological entanglement entropy, by combining results for various flux densities and setting $\ell_B = \sqrt{\hbar/eB}$ as the relevant length scale. This allows us to obtain many more data points, and therefore a higher accuracy, at a relatively small increase in computational cost.

We show extensive numerical evidence for the existence of a class of phase transitions between integer and fractional CI states in chapter 6. These transitions occur in the Harper-Hofstadter model when there is a competition between states supported by different subsets of sub-bands in the lowest Landau level (LLL) tail. As the Hall conductivity σ_H changes discontinuously through these transitions, we label them plateau transitions. Our numerics indicate some signs of criticality at the transition, such as a divergence of the correlation length, as well as a central charge c that varies with cylinder circumference. No presently known theory is able to capture these plateau transitions.

Acknowledgements

First and foremost, I want to extend my gratitude to my supervisor, Gunnar Möller, for always believing we could do great physics together. You have never failed to challenge and guide me, and I deeply value our collaboration. Thanks also go to Frank Pollmann for his deep involvement with my research, and for always patiently explaining our methods to me. To Paul Strange, my second supervisor, I am grateful for providing continuous calmness and wisdom. I thank Sam Carr, Jorge Quintanilla, Silvia Ramos, and all other members of the PQM group for many interesting meetings, discussions and social events.

I thank the University of Kent, and the School of Physical Sciences, for providing the funding for this PhD, and all administrative, technical and academic staff for providing all the help they have, and giving me as warm an 'academic home' as I could have hoped for. Special thanks go to Tim Kinnear for his help with many, many technical issues. Thanks also go to Suzanne Balabil, Steve Cope, and Gareth Hopkins, for helping me get through difficult times.

For many interesting and fruitful discussions, as well as their helpful feedback on a draft of this thesis, I thank Bartholomew Andrews and Johannes Hauschild. I also thank Johannes and the TeNPy collaboration for letting me be part of the team. Of course, I deeply appreciate the many other people who I have had the pleasure of discussing physics with at summer schools, conferences and other meetings.

To those who shared part of my PhD experience, within SPS and beyond, I am especially grateful. Special mentions go to Adrian, Andy, Gonzalo, Henry, John, Oni, Sarah, Steve, Tyler, and Tym. My Kent tenure would have been wholly different without these people.

As the epigraphs[1] in this thesis will demonstrate, music has been an enormous part of my life at Kent, through rehearsals, performances, and social activities. For this, I will be eternally grateful to all members of the University of Kent Music Department and the University of Kent Music Society, which encompass a group of amazing people too big to list. Nonetheless, special mentions go to Alex D.-V., Alex H., Charlotte, Dan, David, Ian, Jeni, Maddie, Matt, Meg, Molly, Owen, Robert, Sophie, Sue, and Tom.

Finally, and most importantly, I want to thank my family, without whose support I would have accomplished nothing. I want to express my gratitude in particular to Lydia, my sister Eva, and my parents. I am so lucky to know you.

[1] All epigraphs are pieces I performed as part of the University Symphony Orchestra, or studied with my clarinet tutor, Ian Swatman.

Contents

List of Figures

List of Abbreviations

AKLT Affleck-Kennedy-Lieb-Tasaki

CF composite fermion

CFT conformal field theory

CI Chern insulator

DMRG Density Matrix Renormalization Group

ES entanglement spectrum

FCI fractional Chern insulator

FQH fractional quantum Hall

FQHE fractional quantum Hall effect

FS Fermi surface

FSM Finite State Machine

ICI integer Chern insulator

iMPS infinite Matrix Product State

IQH integer quantum Hall

IQHE integer quantum Hall effect

LL Landau level

LLL lowest Landau level

MPO Matrix Product Operator

MPS Matrix Product State

MUC magnetic unit cell

QH quantum Hall

QHE quantum Hall effect

SVD Singular Value Decomposition

TN Tensor Network

List of Symbols

$\hat{a}^\dagger, \hat{c}^\dagger (\hat{a}, \hat{c})$	creation (annihilation) operator
$\mathbf{A}$	vector potential
$\mathcal{A}_i$	Berry connection
B, $\mathbf{B}$	magnetic field (strength, vector)
c	central charge
C	Chern number
e	quantum of electric charge
E, $\mathbf{E}$	electric field (strength, vector)
E_F	Fermi energy
$\mathcal{F}_{ij}$	Berry curvature
$h, \hbar$	Planck constant, reduced Planck constant ($\hbar = h/2\pi$)
$\hat{H}$	Hamiltonian
$\ell_B = \sqrt{\hbar/eB}$	magnetic length
L_x, L_y	system dimensions
n	(particle) density
$\hat{n}$	density operator
n_s	density of states
n_ϕ	flux density
N	(particle) number
q	(electric) charge
S	entropy
S_E	entanglement entropy
S_{topo}	topological entanglement entropy
$\mathbf{v}$, $\hat{\mathbf{v}}$	vector, unit vector.
V	interaction strength
γ	Berry phase
λ_i	singular values
ν	filling fraction
ξ	correlation length
$\Delta\xi$	entanglement gap
ρ	density matrix
ρ_{xy}	transverse resistivity (Hall resistivity)
ρ_{xx}	linear resisitivity
σ_H, σ_{xy}	Hall conductivity
ϕ, Φ	magnetic flux
Φ_0	Quantum of magnetic flux, $\Phi_0 = \frac{2\pi\hbar}{e}$
χ	MPS bond dimension
χ_F	fidelity susceptibility
ψ	wave function
ω_B	cyclotron frequency, $\omega_B = eB/m$

Chapter 1

Introduction

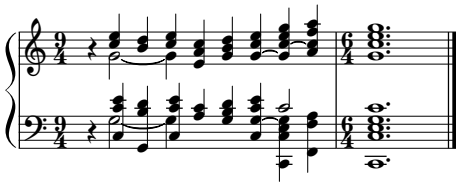

Camille Saint-Saëns, *Symphony No. 3 in C minor, Op. 78*

Within the field of condensed matter physics, the study of (strongly) correlated phases of matter has long held a prominent position. Strongly correlated materials exhibit electronic and magnetic properties that are often unusual, as well as useful for the development of new technologies. The study of strongly correlated electron systems is complicated by the fact (implied by the term 'strongly correlated') that such a system cannot be described accurately in terms of non-interacting component systems, i.e., that the physics of the system is dominated by interactions between particles.

The elucidation of topological order and topological phases has grown to be a prime field of study, with the 2016 Nobel Prize in Physics[1] demonstrating the maturity of this field. These phases pushed out the boundaries of many-body physics, for example by fundamentally changing the understanding of phase transitions (as we will elaborate on in section 1.1.3). Although out of scope for this thesis, recent developments in quantum computing have shown more potential for the application of topological phases (in particular the phenomenon of *topological protection*, meaning the stability of a topologically non-trivial state under smooth deformations of the underlying system).

A first example of a topologically non-trivial state of matter was given by the discovery of the quantum Hall effect (QHE) (resulting in two Nobel Prizes, in 1985[2] and 1998[3]). The QHE describes the quantisation of the Hall conductivity (conductivity perpendicular to external magnetic and electric fields in a two-dimensional sample) and related observables such as conductivity and resistivity. In essence, it is a quantised description of the Hall effect as discovered by Edwin Hall in 1878. Apart from its significance to the study of topological phases, the QHE allows for a straightforward measurement of the fine structure constant e^2/hc, and was used to calibrate the value of the SI unit Ohm until the 2019 redefinition of SI units (fixing the value for h and e). This thesis thus fits in a

[1] Awarded to David J. Thouless, F. Duncan M. Haldane and Michael Kosterlitz, "for theoretical discoveries of topological phase transitions and topological phases of matter".

[2] Awarded to Klaus von Klitzing, "for the discovery of the quantized Hall effect".

[3] Awarded to Robert B. Laughlin, Horst L. Störmer and Daniel C. Tsui, "for their discovery of a new form of quantum fluid with fractionally charged excitations".

long history of the study of topological phenomena in physics in general, and the QHE specifically.

1.1 Phase transitions in quantum physics

We now give a general discussion of phase transitions in quantum physics, as the study of quantum phase transitions (specifically, the subset of topological phase transitions formed by quantum Hall transitions) forms the main research subject of this thesis. We note that a full description of the theory of quantum phase transitions lies far beyond the scope of this thesis. Rather, we focus on a few crucial elements, namely the 'order' of a phase transition, universality and critical scaling, and topological phase transitions. A discussion of the particularities and challenges specific to the *numerical* study of phase transitions will be given in section 3.7, so that we can provide an overview of our numerical methods before diving into this topic.

We here understand a quantum phase transition to be a phase transition between two distinct quantum phases. Contrary to classical phase transitions, the quantum transitions occur at zero temperature, and thus are driven by some other parameter. The parameter value at which the transition occurs is called the *critical point*.[4] We distinguish two broad classes of quantum phase transitions: *first-* and *second-order* transitions.

1.1.1 Order of a quantum phase transition

A first-order transition is characterised by the coexistence of the two phases at a range of values for the parameter driving the transition, as well as finite-range[5] correlations at the transition. In the classical case (with the most common example being the ice-water transition at normal pressure), first-order transitions also involve *latent heat*, i.e., energy is absorbed or released by the system without a change in temperature (see for example Kardar (2007) for an introduction to classical phase transitions).

In contrast, a second-order transition exhibits no latent heat, no coexistence of the two phases, and has a divergence in the range of correlations at the critical point. Correlations typically fall off as a power law for parameter values away from criticality. Second-order transitions are also called *continuous* transitions, due to the internal energy of the system varying continuously with the driving parameter. Second-order transitions are somewhat easier to study than first-order transitions due to the appearance of *universal scaling*.

1.1.2 Universality and critical scaling

A general classification of second-order transitions was introduced by (Landau, 1937), and is now known as *Landau theory*. Landau theory characterises phase transitions through an order parameter, which is zero on one side of the transition, and non-zero on the other side. The order parameter quantifies a spontaneously broken symmetry, i.e., a state which has a 'lower' symmetry than the underlying Hamiltonian.

A commonly cited example to illustrate second-order phase transitions and Landau theory is the Ising transition (Ising, 1925; Onsager, 1944), where the order parameter is the magnetisation m of the system. Here, we distinguish the disordered phase at $T > T_c$ (with $m = 0$) from an ordered phase at $T < T_c$ ($m \neq 0$). In the ordered phase, the Hamiltonian is invariant under a global spin-flip. However, the magnetisation, and thus the phase, does not share this symmetry, instead changing sign when all local magnetic

[4] Technically, a true critical point can only occur in a second order transition.
[5] I.e., non-divergent.

moments are inverted. This is what is meant by the state having a lower symmetry than the Hamiltonian.

Near the critical point, observables like the correlation length ξ depend on the driving parameter as a power law $|P - P_c|^k$, where P is a general parameter and k is the *critical exponent*. A system can be described in terms of a set of critical exponents, combined with their underlying observables and control parameters. These include properties like the order parameter, specific heat, and reduced temperature (T/T_c). A set of critical exponents, or alternatively the dimension of the system combined with the symmetry of the order parameter, defines a universality class of systems independent on the details of these systems, even while said details are highly different between systems. This allows for the study of one system through the study of another system, which can lead to new insights into hard-to-study models. For example, the universality class containing the Ising model also contains ferromagnetic phase transitions.

1.1.3 Topological phase transitions

As outlined above, the description of second-order quantum phase transitions, in particular second-order traditions, traditionally relied heavily on Landau theory. However, with the discovery of topologically non-trivial phases, the need to push the understanding of phase transitions beyond Landau theory arose. As noted above, quantum Hall states and the transitions between them form prime examples of topological phases and phase transitions. In fact, the quantum Hall effect provided the first example of a topologically non-trivial phenomenon in condensed matter physics.

In recent years, extensive work has been done on the classification of topological states (Wen, 1989; Wen, 1990b; Wen, 2017). As a general description of a topological phase, Wen (2017) suggests that these occur at zero temperature, exhibit a finite gap above the ground state, and can exhibit long-range entanglement, even while being apparently featureless, disordered liquids. Wen (2017) further points out a distinction between states with or without topological order, identified through entanglement measures (Kitaev and Preskill, 2006; Levin and Wen, 2006). A somewhat confusing aspect of this distinction is that states with no topological order in this sense (i.e., without long-range entanglement) can still be classified by topological invariants such as the Chern number. Some more information on these topological invariants can be found in section 2.5. We note here that both types of topology appear in this thesis, with the integer quantum Hall states having no topological order, but non-zero topological invariants, and fractional quantum Hall (FQH) states having 'true' topological order (identified in part by fractionalised excitations, as we will see later).

Between distinct topological phases, phase transitions can occur which do not break any symmetries of the underlying Hamiltonian. Such a transition is called a *topological phase transition*, and cannot be captured by Landau theory. An established mechanism for transitions between distinct topologically ordered phases to occur is given by *anyon condensation* (Burnell, 2018).

1.2 Overview of this thesis

As stated, the aim of this thesis is to push the boundaries of knowledge on (fractional) quantum Hall (QH) states and the phase transitions that can occur between them. We here describe the outline of this thesis, and indicate how it fits in with the broad theoretical landscape as described above. This thesis can broadly be divided into two parts. Firstly, to lay the theoretical groundwork, chapters 2, 3 and 4 provide introductions to the

QHE, the Harper-Hofstadter model, and Matrix Product States (MPSs) and the Density Matrix Renormalization Group (DMRG), respectively. Secondly, chapters 5 and 6 contain novel work, with chapter 7 providing a recap, conclusions and outlook for future studies.

Specifically, chapter 5 studies the existence of FQH states in the Harper-Hofstadter model 'tail', which can be adiabatically connected to the LLL. In particular, we study cases where the LLL tail consists of several magnetic sub-bands. This work solidifies the existing belief that QHE states are supported in this regime, as well as improving on previous numerical studies of the topological entanglement entropy. Additionally, the results in chapter 5 serve as a springboard for the work in chapter 6, in which the existence of FQH states on the LLL Harper-Hofstadter tail (with multiple sub-bands) is the starting point.

Chapter 6 investigates a novel class of phase transitions that occur between QH states in the Harper-Hofstadter model. Specifically, we find transitions which occur between FQH states supported on the entire (multiple-sub-band) LLL Harper-Hofstadter tail, and other QH (or Chern insulator (CI)) states supported by a subset of sub-bands. We demonstrate that no presently known theory for the transition between lattice QH states is able to explain these transitions. Therefore, we have uncovered what we believe to be a novel class of QH plateau transitions, with potentially far-reaching consequences for the understanding of the fractional quantum Hall effect (FQHE). We provide some steps toward a theoretical understanding of our transition, but leave a full theoretical description to future works.

Chapter 2

The quantum Hall effect

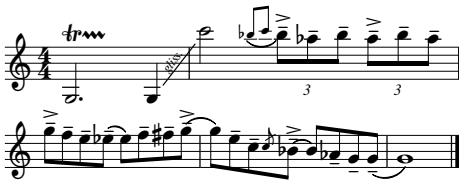

George Gershwin, *Rhapsody in Blue*

This chapter provides an introduction to the quantum Hall effect (QHE). Many more extensive introductions to the subject have been written over the years (see for example Girvin, 1999; Bergholtz and Liu, 2013; Parameswaran, Roy, and Sondhi, 2013; Tong, 2016). The goal here is not to provide a complete, comprehensive overview of the QHE, but rather to provide enough background for the reader to place the rest of this thesis in context, and to provide references for further reading, should that be desired.

2.1 History

The 'classical' Hall effect[1] has been known since its discovery in 1879 by Edwin Hall. The Hall effect effect describes the (classical) motion of electrons in a thin sheet of metal[2] (i.e., the sample is spanned by $\hat{\mathbf{x}}$ and $\hat{\mathbf{y}}$) with an electric current along $\hat{\mathbf{x}}$, subject to a magnetic field perpendicular to the material (i.e., along $\hat{\mathbf{z}}$). It can be explained by simple electrodynamics.

The magnetic field induces a Lorentz force on the electrons, which causes the charge carriers to be deflected from their straight path through the metal. As a consequence, a non-zero total charge will build up on one edge of the material, which in turn causes a voltage gradient across the sample. The combined electric and magnetic fields[3] thus induce a voltage along $\hat{\mathbf{y}}$, with an associated resistivity that scales linearly with the strength of the magnetic field, $\rho_{xy} \propto B$. This resistivity is called the *Hall resistivity*. An illustration of this mechanism is given in figure 2.1.

Some 100 years later, the QHE was first observed by Klitzing, Dorda, and Pepper (1980). Their effect was later renamed the integer quantum Hall effect (IQHE), see also section 2.2. Shortly thereafter, Tsui, Stormer, and Gossard (1982) discovered the fractional quantum Hall effect (FQHE), see also section 2.3. Both QHEs have a common feature in the quantization of the Hall resistivity. That is, instead of the expected linear scaling we

[1] Henceforth we will refer to the classical (non-quantum) effect as "Hall effect", and consistently name the quantum effects quantum Hall effects (QHEs).

[2] We here assume a simple metal, where electrons are the only charge carriers.

[3] The electric field is what initially caused the current.

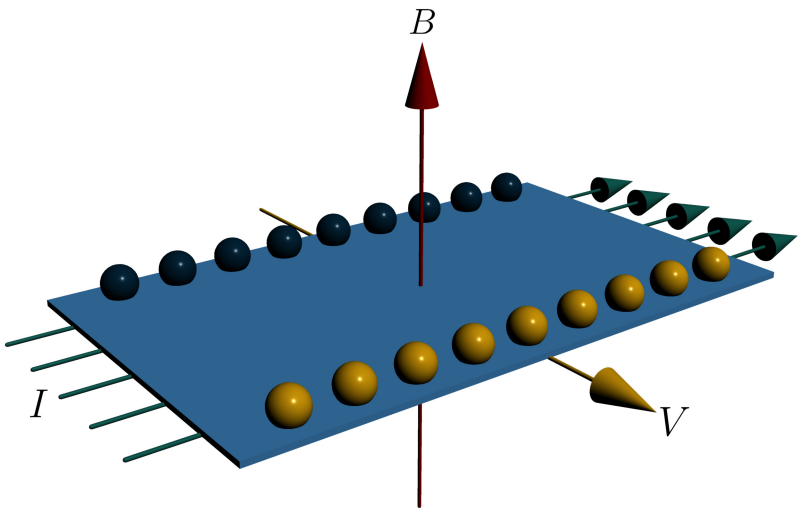

FIGURE 2.1: The classical Hall effect. A current **I** (green arrows) passes through a two-dimensional sample (blue). Under influence of a magnetic field **B** (red arrow), moving charges forming the current get deflected (blue and yellow spheres, denoting oppositely charged particles), causing a voltage (yellow arrow) perpendicular to both **B** and **I**.

just mentioned, ρ_{xy} exhibits plateaux for a range of field strengths and sudden jumps between these plateaux (see figure 2.2). These discontinuities in ρ_{xy} are accompanied by peaks in the linear resistivity ρ_{xx}, which is otherwise zero.

Theoretical explanations of the quantum Hall effects followed soon after (Laughlin, 1981; Laughlin, 1983) and the field has since grown to be as active as it is diverse. The next sections will treat the theory behind the integer and fractional QHE in more detail.

2.2 The integer quantum Hall effect

The Hamiltonian for electrons (with mass m and charge $-e$), confined to move in two dimensions $(\hat{\mathbf{x}}, \hat{\mathbf{y}})$ subject to a magnetic field $\mathbf{B} = \nabla \times \mathbf{A}$ is[4]

$$\hat{H} = \frac{1}{2m}(\mathbf{p} + e\mathbf{A})^2, \tag{2.1}$$

where $\mathbf{A}$ is the vector potential and $\mathbf{p}$ the electron's momentum. Taking the magnetic field to be perpendicular to the plane of movement of the electrons, $\mathbf{B} = B\hat{\mathbf{z}}$, leaves several gauge choices for $\mathbf{A}$. In this thesis, we will usually consider the Landau gauge $\mathbf{A} = Bx\hat{\mathbf{y}}$, unless noted otherwise. The magnetic field strength B is often expressed in units of the *magnetic flux quantum* $\Phi_0 = \frac{2\pi\hbar}{e}$, which we think of as the amount of magnetic flux piercing an area of $2\pi\ell_B^2$, where $\ell_B^2 = \hbar/eB$ defines the *magnetic length*.

2.2.1 Landau levels and perpendicular response

The Hamiltonian (2.1) can be solved straightforwardly in a gauge-invariant manner. By constructing ladder operators, the Hamiltonian takes the form of a harmonic oscillator, allowing us to obtain a spectrum (Jain, 2007)

$$E_n = \hbar\omega_B \left(n + \frac{1}{2}\right), \tag{2.2}$$

[4]The derivations in this section follow closely those in Tong (2016).

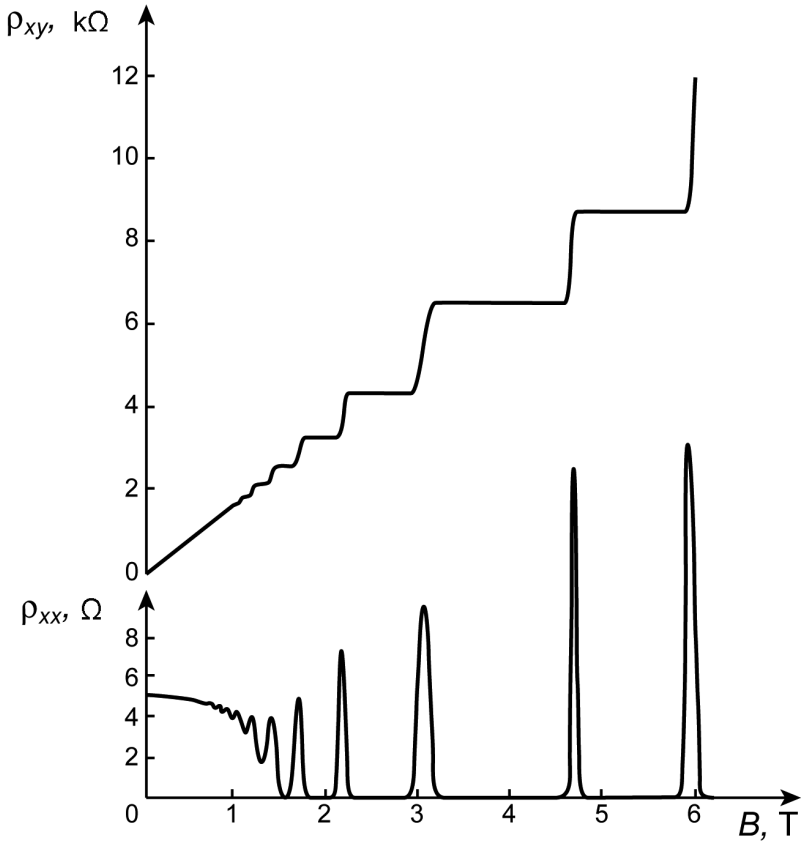

FIGURE 2.2: The quantum Hall effect. Top: Hall resistivity ρ_{xy} as a function of magnetic field strength B at $T \approx 8\,\text{mK}$, showing clearly the quantized plateaux mentioned in the main text. Classically, the relationship would be linear. Bottom: Linear resistivity ρ_{xx} as function of the magnetic field, showing a peak whenever ρ_{xy} jumps between plateaux. Figure copyright © Wikimedia Commons: Quantum Hall effect by Antikon. Licensed under CC-BY-SA 3.0. Reproduced from Gavrilenko and Ikonnikov (1986).

where $\omega_B = eB/m$ is the cyclotron frequency. The equally spaced (by a gap proportional to B) energy levels E_n are known as Landau levels (LLs).

Every LL is highly degenerate. This can be seen by solving the Hamiltonian (2.1) in the Landau gauge, which again yields the spectrum (2.2) but also gives us the corresponding (non-normalised) states

$$\psi_{n,k}(x,y) \sim e^{iky} H_n(x + k\ell_B^2) e^{-(x+k\ell_B^2)^2/2\ell_B^2}, \tag{2.3}$$

where $k \in \mathbb{R}$ is interpreted as momentum. Switching to the symmetric gauge, $\mathbf{A} = -(yB/2)\hat{\mathbf{x}} + (xB/2)\hat{\mathbf{y}}$, in the lowest Landau level (LLL) ($n = 1$) this reduces to[5]

$$\psi_{\text{LLL},m} \propto \left(\frac{z}{\ell_B}\right)^m e^{-|z|^2/4\ell_B^2}, \tag{2.4}$$

where $z = x - iy$. Note that these states are eigenstates of the angular momentum operator $\hat{J}$:

$$\hat{J}\psi_{\text{LLL},m} = \hbar m \psi_{\text{LLL},m}. \tag{2.5}$$

[5]Using the symmetric gauge rather than the Landau gauge, we lose the k-dependency, but gain a quantum number m which denotes separate degenerate states within the LLL.

Confining these states to an $L_x \times L_y$ region with periodic boundary conditions yields a quantisation of the momentum k in units of $2\pi/L_y$. Simultaneously, k is constrained to be in the range $-L_x/\ell_B^2 \leq k \leq 0$ due to the localisation of (2.3) near $x = -k\ell_B^2$. Thus, for a given value of n, the LL supports a total of

$$N = \frac{L_y}{2\pi}\int_{-L_x/\ell_B^2}^{0} \mathrm{d}k = \frac{eBL_xL_y}{2\pi\hbar} = \frac{BL_xL_y}{\Phi_0} \tag{2.6}$$

states.

We can begin to understand the quantisation of the Hall conductivity[6] starting from the Hamiltonian (2.1) once we include an electric field:

$$\hat{H} = \frac{1}{2m}(\mathbf{p} + e\mathbf{A})^2 + eEx = \frac{1}{2m}\left(p_x^2 + (p_y + eBx)^2\right) + eEx, \tag{2.7}$$

where the last equality holds in the Landau gauge. This Hamiltonian results in states and energy levels that are slight modifications (denoted with tildes) of those in (2.2) and (2.3):

$$\tilde{\psi}_{n,k}(x,y) = \psi_{n,k}\left(x + \frac{mE}{eB^2}, y\right) \tag{2.8}$$

$$\tilde{E}_{n,k} = \hbar\omega_B\left(n + \frac{1}{2}\right) - eE\left(k\ell_B^2 + \frac{eE}{m\omega_B^2}\right) + \frac{m}{2}\frac{E^2}{B^2}. \tag{2.9}$$

In (2.9), the degeneracy between states in the LL has been lifted in favour of a linear dependence of $E_{n,k}$ on k. Due to this, states in the LL now drift along $\hat{\mathbf{y}}$ with velocity $v_y = \hbar^{-1}\partial E/\partial k = -E/B$. Thus, a combination of perpendicular electric (along $\hat{\mathbf{x}}$) and magnetic (along $\hat{\mathbf{z}}$) fields causes the charge carriers to drift along $\hat{\mathbf{y}}$. This is the quantum mechanical version of the perpendicular response ρ_{xy} as introduced in section 2.1. Assuming some separation between subsequent Landau levels, the quantisation of the Hall conductivity can now be interpreted as deriving from the sequential filling of higher LLs, where each level contributes equally to the conductivity. This will be expanded on shortly, as the picture painted so far is somewhat 'cartoonish' and does not capture the IQHE in full.

2.2.2 Edge modes

It turns out that the transverse Hall conductivity σ_H (or σ_{xy}) is carried by *edge modes*, which are localised near the physical boundary of the $L_x \times L_y$ sample. We can see this by considering a LL constrained only along $\hat{\mathbf{x}}$ by some potential $V(x)$ (see figure 2.3). We can rewrite the Hamiltonian for this setup (in the Landau gauge) as

$$\hat{H} = \frac{1}{2m}(\mathbf{p} + e\mathbf{A})^2 + V(x) = \frac{1}{2m}\left(p_x^2 + (p_y + eBx)^2\right) + V(x). \tag{2.10}$$

Expanding the potential to linear order,[7] we obtain a Hamiltonian very similar to (2.7). The corresponding drift velocity along $\hat{\mathbf{y}}$ is given by $v_y \propto \partial V/\partial x$. Due to the opposite sign of $\partial V/\partial x$ at opposite edges of the sample (figure 2.3), the modes at the edge are chiral. The chirality of the edge modes in part explain the stability of the quantum Hall (QH) plateaux: for a perturbation to cause backscattering of an edge mode, it needs to

[6] Note that the conductivity $\sigma = 1/\rho$ is the inverse of the resistivity.

[7] A decent approximation as long as the potential does not vary too much within length scales on the order of ℓ_B, as without the potential, the wave functions are Gaussians of width ℓ_B.

scatter the mode into the edge mode at the opposite edge of the sample. This process is exponentially suppressed by the size of the sample bulk.

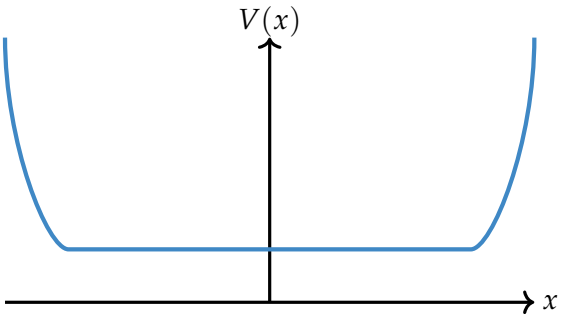

FIGURE 2.3: Confining potential along $\hat{\mathbf{x}}$.

If we imagine filling the LL up to some Fermi energy E_F, we can see an equal number of filled states on either edge of the sample. We can induce a current along $\hat{\mathbf{y}}$ on this model by introducing an offset chemical potential $\Delta\mu$ between the two edges, effectively raising E_F on one edge relative to E_F at the other edge. This results in more states being filled on one end of the sample than on the other, which through the chirality of these edge modes leads to a non-zero Hall conductivity

$$\sigma_H = \frac{I_y}{V_H} = \frac{e^2}{2\pi\hbar}, \tag{2.11}$$

where $I_y = \frac{e}{2\pi\hbar}\Delta\mu$ is the $\hat{\mathbf{y}}$-current induced by the offset chemical potential.

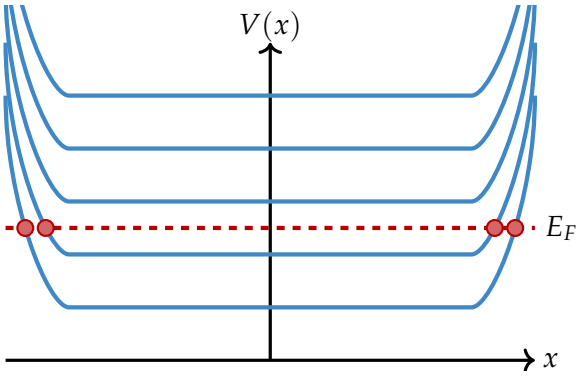

FIGURE 2.4: Fermi energy E_F between the second and third Landau levels.

We can now interpret the transition between different Hall plateaus (figure 2.2) in the following way. A single filled LL leads to a Hall conductivity $\sigma_{xy} = \frac{e^2}{2\pi\hbar}$, as explained above. Raising the Fermi energy E_F, we fill higher Landau levels, which in turn contribute similarly to the conductivity (figure 2.4). The total conductivity yielded by N filled Landau levels is thus given by $\sigma_{xy} = Ne^2/2\pi\hbar$.

2.2.3 Edge excitations and level counting

In a filled LL in its ground state, all available states up to E_F are filled, as discussed. The states are spaced equally along k (or x, due to the localisation of states at $x = -k\ell_B^2$), with a spacing $2\pi/L_y$ due to the confinement of the sample. At the edge of the LL, the dispersion relation is approximately linear. This implies that we can understand excitations on the

ground state through the 'outward' shifting of particles along the edge potential: a single step $2\pi/L_y$ increases the energy by a minimal amount.

The process of exciting more and more particles across the edge of the LL (figure 2.5) yields a rich excitation spectrum (Haldane, 1991; Wen, 1992; Haldane, 2006; Bernevig and Haldane, 2008; Li and Haldane, 2008). In particular, the (near-) degeneracies of this spectrum (i.e., the number of states at each energy) is given by the *partition counting sequence* $1, 1, 2, 3, 5, 7, \cdots$, starting from the ground state. This counting is applicable to any edge described by a $U(1)$ conformal field theory, whereas it is different for non-Abelian states such as the Moore-Read state [see for example Regnault, Bernevig, and Haldane (2009)].

The edge states and edge excitations of a QH system form a deep and varied field of research in themselves. In particular, the field theory describing the edge of the QH sample is called a *chiral Luttinger liquid*[8] (Wen, 1990a; Chang, 2003). A full introduction to these theories lies well beyond the scope of this thesis. However, some properties of the edge modes and edge excitations will be used to identify QH states in later chapters.

2.2.4 Forming plateaux: disorder

One aspect to the stability of the QH plateaux lies, as stated, in the chirality of the edge modes and the suppression of backscattering processes. This, however, does not explain how plateaux can persist over a range of the magnetic field: a small deviation from a filled Landau level at fixed particle density would result in a partially filled highest Landau level, which invalidates the reasoning above. It turns out that the stability of the plateaux can be explained by a small, random impurity potential $|V(x)| \ll \hbar\omega_B$ on top of the LL (Halperin, 1982).

The addition of the disorder potential to the Hamiltonian (2.1) has two effects. Firstly, it will split the macroscopic degeneracy of the LL into a broader band of states (figure 2.6). Secondly, it creates a distinction between extended and localised states, where only the extended states are supported on the entire width (or length) of the sample, and the localised states are confined to some smaller region (figure 2.7).

The localisation of some states can be derived by imposing the following condition on the variation of the disorder potential:

$$|\Delta V| \ll \frac{\hbar\omega_B}{\ell_B}, \tag{2.12}$$

i.e., the potential varies on length scales much bigger than the cyclotron orbit of a single particle. Thus every cyclotron orbit takes place in an essentially flat background potential and, by conservation of energy, will remain on an equipotential line in the potential landscape (figure 2.7). Therefore, only those particles that move (with their drift velocity) along equipotential lines connecting the edges of the sample will contribute to the conductivity. These equipotential lines have to be (roughly) in the vertical centre of the potential landscape; thus the extended states are in the centre of the broadened LL band (Tsukada, 1976; Ando, 1983), as shown in figure 2.6.

We can now understand the IQH plateaux as follows. Upon varying the magnetic field, the Fermi energy E_F shifts through the spectrum in figure 2.6. When E_F enters into a band, at first only localised states will be populated. It is only when E_F crosses

[8] Chiral Luttinger liquids have been reasonably well-studied experimentally. Measurements on the chiral Luttinger liquid for the $\nu = \frac{1}{3}$ Laughlin state have been performed and have been found to violate Ohm's law, instead showing a non-linear power law relation $I \propto V^{\alpha}$ (Chang, Pfeiffer, and West, 1996), in line with theoretical predictions (Kane and Fisher, 1995). Additionally, the charges carrying the edge current were measured using shot noise experiments (Saminadayar et al., 1997; de-Picciotto et al., 1997). These charges were found to be fractions $e^* = \frac{e}{3}$ of the electron charge, strengthening the Luttinger liquid picture.

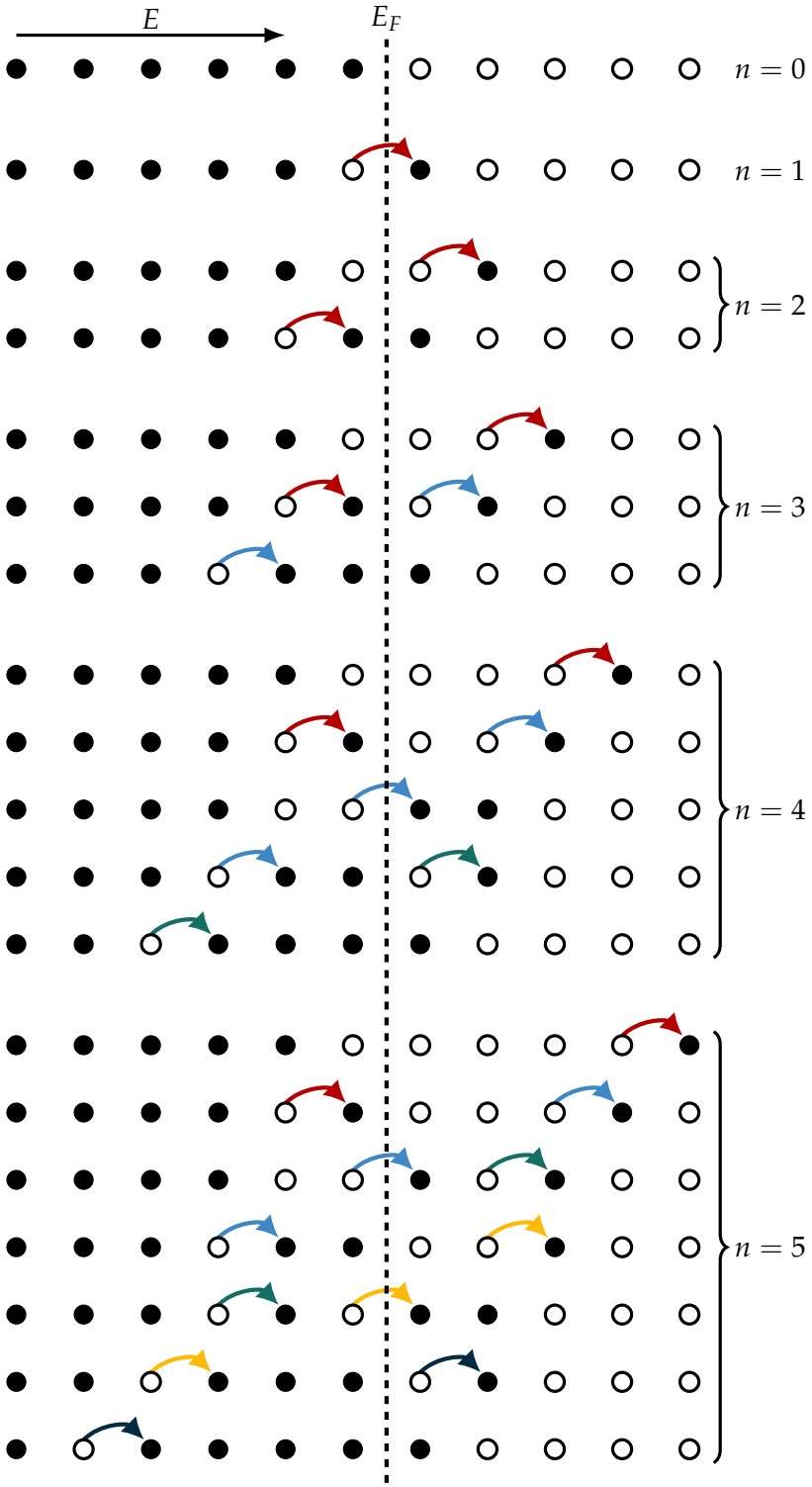

FIGURE 2.5: Edge excitations on one edge of a homogeneously filled Landau level. Differently coloured arrows denote excitations on top of different states in the previous 'generation': red (first row), blue (second row), green (third row), yellow (fourth row) and dark blue (fifth row). For example, the second state at $n = 3$ can be obtained by exciting the second-to-last particle starting from the first $n = 2$ state, or by exciting the rightmost particle starting from the second $n = 2$ state. The dispersion relation at the edge is approximately linear. The degeneracies on subsequent excitations (starting with the ground state) follow the partition counting sequence $1, 1, 2, 3, 5, 7, 11, \cdots$.

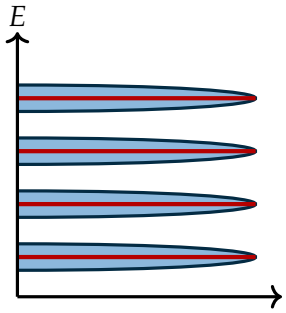

FIGURE 2.6: A small amount of disorder breaks the degeneracy within a Landau level (equation 2.2, red lines) and broadens the bands. Extended states will be found only at the center of the bands (red lines), while the rest of the band (blue) consists of localised states.

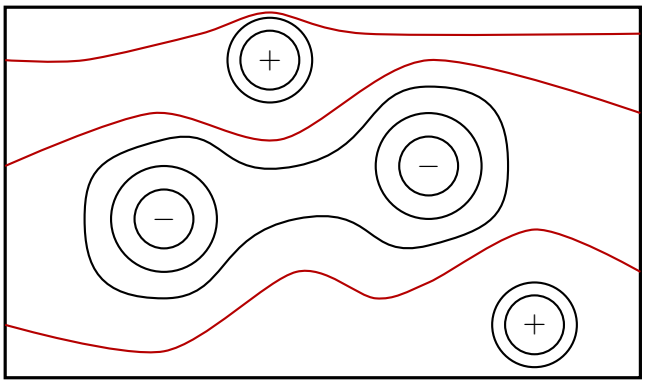

FIGURE 2.7: The (random) disorder potential creates a landscape of peaks and valleys. If $|\Delta V| \ll \hbar\omega_B/\ell_B$, particles in their cyclotron orbits will move along equipotential lines. Only a few equipotential lines (red) will connect the edges of the sample. Therefore, only the particles moving along those lines will contribute to the conductance through the sample. Upon raising the Fermi energy through this landscape, a percolation transition occurs when the extended states get populated.

the narrow region at the centre of the band that extended states get populated and the conductivity shifts. Thus, we find wide regions of stable conductivity, separated by reasonably sharp transitions, exactly like figure 2.2. Due to the way E_F 'filters through' the potential landscape, these transitions are called *percolation transitions* (Aoki and Ando, 1981; Prange and Joynt, 1982; Chalker and Coddington, 1988; Huckestein, 1995).

2.3 The fractional quantum Hall effect: Laughlin states

Section 2.2 explains the IQHE through the successive filling of Landau levels when varying the magnetic field strength. For the fractional quantum Hall effect (FQHE), this explanation is no longer sufficient: the FQHE plateaux appear at *fractional* LL filling factors. It turns out that to explain the FQHE, we need to include the interactions between particles.

A first approach to explaining the FQHE was due to Laughlin (Laughlin, 1983), with the eponymous *Laughlin states*, describing filling fractions[9] $\nu = 1/m, m \in \mathbb{N}$:[10]

$$\psi_m(\{z_k\}) = \prod_{k<j}(z_k - z_j)^m \exp\left[\sum_k \frac{|z_k|^2}{4l_B^2}\right], \tag{2.13}$$

where $z_k = x_k + iy_k$ is a coordinate for a particle in 2 dimensions. If m is odd, (2.13) describes a fermionic wave function; if m is even, (2.13) describes bosons. The Laughlin states form a superposition of single-particle LLL wave functions, with a prefactor that ensures an inter-particle separation to minimise interaction energy.

For any individual particle, labelled by z_1 without loss of generality, (2.13) is proportional to

$$\prod_{i=2}^{N}(z_1 - z_i)^m, \tag{2.14}$$

which tells us the highest power of z_1 in ψ_m is $m(N-1)$. Therefore, considering (2.4) and (2.5), the highest angular momentum of this (and indeed any) particle is $m(N-1)$, which implies the particle is localised within a ring of radius $R \approx \sqrt{2mN}\ell_B$.[11] This puts the area of the QH "droplet" at $A \approx 2\pi mN\ell_B^2$. Per (2.6), the LL supports a maximum of AB/Φ_0[12] states, which when N particles are added yields a filling fraction

$$\nu = \frac{N}{AB/\Phi_0} = \frac{2\pi\hbar N}{2\pi mNB\ell_B^2} = \frac{1}{m} \tag{2.15}$$

as was stated before.

Laughlin (1983) showed the Laughlin state to have an overlap of over 99% with the (numerically obtained three-particle $m = 3$) exact FQH ground state of the many-body Hamiltonian

$$\hat{H} = \sum_j \left[(\mathbf{p}_j + e\mathbf{A}_j)^2 + V(z_j)\right] + \sum_{j>k} U(|zj - z_k|) \tag{2.16}$$

at $V = 0$ and for $U(r)$ of the form $1/r$, $-\log r$ or $e^{-r^2/2}$. For Coulombic interactions, overlaps were lower but still large (e.g., about 98%) for the $m = 3$ state. Additionally, Trugman and Kivelson (1985) demonstrated that (2.13) is the exact ground state for Hamiltonians with shorter-range interactions of the form

$$U(\mathbf{r}) = \alpha\nabla^2\delta^{(2)}(\mathbf{r}), \tag{2.17}$$

where $\delta^{(2)}(\mathbf{r})$ is the Dirac delta function in two dimensions and ∇^2 is the Laplacian. The Laughlin state reproduces many of the exact state's properties (Fradkin, 2013). Most interestingly for this thesis, the Laughlin state gives rise to *quasiparticle excitations*.

2.3.1 Quasi-holes and -particles

A quasi-hole excitation on the Laughlin state (2.13) is given by (Laughlin, 1983)

$$\psi_{\text{hole}}(\{z_k\}; \eta) = \prod_{i=1}^{N}(z_i - \eta)\psi_m(\{z_k\}), \tag{2.18}$$

[9] Note the change in nomenclature, from filling *factor* in the IQHE to filling *fraction* in the FQHE.
[10] The product is only over the terms $(z_k - z_j)^m$, *not* over the exponent.
[11] Approximating $N \approx N - 1$ (this is many-body physics after all).
[12] Taking $A = L_x L_y$.

with the quasi-hole at $z = \eta$: at these coordinates, $\psi = 0$, i.e., there is no electron density at $z = \eta$, thus there is a 'hole' in the electron state.

A quasi-hole carries a *fractional charge* $e^* = e/m$, where the electron charge is taken to be $-e$. This can be intuited by adding m holes to the system at the same coordinates η, thereby multiplying (2.13) by

$$\prod_{j=1}^{m}(z_j - \eta)^m, \tag{2.19}$$

which corresponds to an electron-equivalent term describing the *absence* of an electron at η. Quasi-particle excitations are added to the wave function similarly, by adding a factor

$$\prod_{i=1} N\left(2\frac{\partial}{\partial z_i} - \bar{\eta}\right) \tag{2.20}$$

to (2.13).

Quasi-particles and -holes lead to a generalisation of many-body statistics to *fractional statistics*. Upon the exchange of two particles in a many-body wave function, the wave function picks up a phase

$$\psi(\mathbf{r}_1, \mathbf{r}_2) = e^{i\pi\alpha}\psi(\mathbf{r}_2, \mathbf{r}_1), \tag{2.21}$$

where $\alpha = 0$ or $\alpha = 1$ for bosons or fermions, respectively. Quasi-particles and -holes, in contrast, have $\alpha = 1/m$. Because they are therefore "neither fermions nor bosons", they are sometimes called *anyons*. Note that for a filled LL ($m = 1$), the quasi-holes are fermions (namely, actual holes), while for any $m > 1$ a collection of m quasi-holes behaves like a fermion (boson) if m is odd (even).

2.3.2 Hierarchy

We can obtain different FQH states by building a *hierarchy* of states on top of the Laughlin states (Haldane, 1983; Halperin, 1984). Starting from the Laughlin state (2.13), we can move away from a filling fraction $\nu = 1/m$ by changing the magnetic field B. If the new filling fraction ν' remains close to the original ν, this is expected to create some density of quasi-particles or -holes on top of the Laughlin state, rather than create a new state altogether.

The Laughlin state for anyons is proportional to

$$\prod_{i<j}^{N}(\eta_i - \eta_j)^{2p+\alpha}, \tag{2.22}$$

where $\eta_{i,j}$ are anyon coordinates, α is the anyon statistical parameter (cf. equation 2.21) and $p \in \mathbb{N}$ a positive integer. A given quasi-particle or -hole excitation (with $\alpha = 1/m$) has a maximum angular momentum $N(2p \pm 1/m)$.[13] Following the same reasoning from earlier in section 2.3, we replace $\ell_B^2 \to m\ell_B^2$ due to the quasiparticle charge being $|q| = e/m$ to obtain the area of the 'droplet' as $A \approx 2\pi(2p \pm 1/m)N(m\ell_B^2)$. Considering each of the AB/Φ_0 electron states in the filled LL to be made up of m quasi-objects, there are

$$N_{\text{quasi}} = \frac{mAB}{\Phi_0} = \left(2p \pm \frac{1}{m}\right) m^2 N \tag{2.23}$$

quasi-object states in a fully filled LL.

[13] The $\pm$ corresponds to the charge of the excitation.

The quasi-particles and -holes can now form a quantum Hall state themselves, which contributes to the electron filling fraction ($\nu_{\text{quasi}} = N/N_{\text{quasi}}$) by

$$\nu_{\text{quasi}} = \pm\frac{1}{2pm^2 \mp m}, \tag{2.24}$$

where $p \in \mathbb{N}$. The upper sign corresponds to a quasi-particle, while the lower sign corresponds to a quasi-hole. Thus, we find an overall filling fraction

$$\nu = \frac{1}{m} \pm \frac{1}{2pm^2 \mp m} = \frac{1}{m \mp \frac{1}{2p}}. \tag{2.25}$$

Starting from the $\nu = 1/3$ Laughlin state, setting $p = 1$ for quasi-particles (the upper sign in equation 2.25) gives $\nu = 2/5$, while $p = 1$ for quasi-holes (the lower sign) results in $\nu = 2/7$. Both these filling fractions have been observed, with $\nu = 2/5$ being particularly prominent.

This procedure can now be repeated: we imagine quasi-particle (and -hole) excitations on top of the Laughlin state formed by the first 'layer' of quasi-particles, which can then again form a Laughlin state. On top of *that* Laughlin state, we can imagine yet more quasi-excitations, repeating this process indefinitely to obtain the *hierarchy of QH states*:[14]

$$\nu = \cfrac{1}{m \pm \cfrac{1}{2p_1 \pm \cfrac{1}{2p_2 \pm \cdots}}}, \tag{2.26}$$

which reproduces many experimentally observed filling fractions.

2.3.3 Composite fermions

An alternative way of obtaining the hierarchy of (fermionic) FQH filling fractions is through the concept of *composite fermions* (CFs) due to Jain (Jain, 1989; Jain, 2007), building on work by Arovas et al. (1985) and Laughlin (1988). The core idea of this approach is that electrons couple to 'flux tubes' to form composite objects. The composite particles form an IQH state, which leads to an FQH state at the level of electrons.

In Jain's original formulation, we start from an integer LL filling factor $\nu = p \in \mathbb{N}$. In this case, there is an average flux density of Φ_0/p per electron. CFs are created by 'attaching' $\alpha\Phi_0$ flux to each electron. The exchange phase factor of the composite particles is now

$$\psi(\mathbf{r}_1, \mathbf{r}_2) = e^{i\pi(1+\alpha)}\psi(\mathbf{r}_2, \mathbf{r}_1), \tag{2.27}$$

which has contributions both from the fermionic statistics of the electron, as well as an extra Aharonov-Bohm phase resulting from the attached flux. If $\alpha = 2m, m \in \mathbb{Z}$, this reproduces a fermionic state.[15,16] As the CFs behave like fermions in a residual magnetic field, it is then argued that the IQH state without flux attachment implies the existence of

[14] Note that we can terminate the continued fraction at any point, corresponding to that particular 'layer' of quasi-objects forming a Laughlin state without excitations.

[15] Note that m here is *not* the denominator of the Laughlin state filling fraction, but rather the index for the different energy levels.

[16] The theory for fermions requires attaching an even number of flux quanta to each electron. A theory for bosons can attach an odd number of flux quanta (Möller and Cooper, 2009).

an IQH state for CFs with $2m\Phi_0$ flux attached to each electron. This latter state is denoted $\psi^{2m}_{\pm p}$, while the IQH state is $\psi_{\pm p}$.[17]

The link to the FQHE is made as follows. A uniform electron state with $\alpha\Phi_0$ flux attached to each electron is equivalent to a uniform electron state in a uniform magnetic field with a flux density $\alpha\Phi_0$ per electron. The state $\psi^{2m}_{\pm p}$ has $2m \pm p^{-1}$ flux quanta per electron, which yields a residual flux density of Φ_0/p per CF, which is exactly the density as described above for the integer case. The CF state can therefore be identified with an electron state at

$$\nu = \frac{p}{2mp \pm 1}. \tag{2.28}$$

Thus, we can describe the FQHE for electrons as the IQHE for CFs. This construction reproduces the same filling fractions as (2.26), with the (historically significant) added benefit of explaining why only odd denominators are found, as well as the order in which subsequent fractions appeared with improved sample quality.

2.3.4 Generalised Pauli principle

The Pauli principle (Pauli, 1925) states that two electrons cannot occupy the same state. In spinless many-body wave functions, this constraint is satisfied by setting $\psi(\{\mathbf{r}_i\}) = 0$ whenever $\mathbf{r}_i = \mathbf{r}_j, i \neq j$. It is this principle that is responsible for the ground state being the top row in figure 2.5, where available states are filled with exactly one particle each, up to the Fermi energy. We can write this ground state as

$$111111111111\cdots111|000\cdots,$$

with the first excitation being

$$111111111111\cdots110|100\cdots.$$

We re-emphasise that the 1s and 0s in this notation are taken to mean the occupation number of a (single-particle) state in the angular momentum basis, which corresponds to the occupation of a state within a particular radius r.

For Laughlin states (which have a particle density far below a filled LL), a *generalised Pauli principle* (Haldane, 1991; Haldane, 2006) has been derived, in which (for $\nu = 1/m$) every m subsequent states can contain at most one particle. Hence the $\nu = 1/3$ state has every third state filled on average:

$$100100100100\cdots001|000\cdots.$$

A rigorous derivation of the generalised Pauli principle can be performed by identifying the Laughlin state with *Jack polynomials* J^{α}_{λ} (Bernevig and Haldane, 2008). The J^{α}_{λ} can describe generic filling fractions $\nu = k/r$, under an admissibility constraint (Feigin et al., 2002) stating that r consecutive single-particle states cannot contain more than k particles. This maps exactly onto the generalised Pauli principle as described above.

2.4 Flux insertion and spectral flow

We now turn our attention to the relationship between flux Φ and Hall conductivity σ_H, following an idea first outlined by Laughlin (1981). Considering a particle constrained to be a distance r from the origin on the annulus in the $(\hat{\mathbf{x}}, \hat{\mathbf{y}})$-plane, with a magnetic flux Φ

[17] The sign of $\pm p$ corresponds to the direction of the magnetic field in $\mp\hat{\mathbf{z}}$.

piercing the system through the centre of the annulus ($r = 0$) in the $\hat{\mathbf{z}}$-direction. We can rewrite the Hamiltonian (2.1) to depend only on the azimuthal angle coordinate ϕ:

$$\hat{H} = \frac{1}{2mr^2}\left(-i\hbar\frac{\partial}{\partial\phi} + \frac{e\Phi}{2\pi}\right)^2. \tag{2.29}$$

This changes the spectrum from (2.2) to

$$E_m \propto \left(\hbar m + \frac{e\Phi}{2\pi}\right)^2 \propto \left(m + \frac{\Phi}{\Phi_0}\right)^2, \tag{2.30}$$

where $m \in \mathbb{Z}$. Thus, the spectrum is identical for any $\Phi = p\Phi_0, p \in \mathbb{Z}$. Upon the adiabatic insertion of flux, the energy levels will slowly evolve until the spectrum is mapped onto itself. The process of mapping the spectrum $\{ E_m \}$ onto itself when inserting flux is called *spectral flow*.

2.4.1 Spectral flow in integer quantum Hall states

The above implies that upon increasing Φ, an energy eigenstate that started at $\Phi = 0$ will evolve into a *different* eigenstate at $\Phi = \Phi_0$. This operation is equivalent to increasing the value of m in (2.30) by 1. Thus, restricting ourselves to the LLL (with wave functions given in equation 2.4) for now, we observe that a single-particle state localised near $r \approx \sqrt{2m\ell_B^2}$ shifts outwards to $r \approx \sqrt{2(m+1)\ell_B^2}$ upon insertion of a single Φ_0 through the origin:

$$\psi_m(\Phi = 0) \to \psi_m(\Phi = \Phi_0) = \psi_{m+1}(\Phi = 0), \tag{2.31}$$

where r is fixed. As this happens to every energy eigenstate, the net effect of inserting a single Φ_0 is to transport a single electron from the inside of the annulus to the outside.

This derivation generalises to higher LLs. Therefore, in an IQH state with n filled LLs, the insertion of a single flux quantum transports n electrons, yielding a conductivity $\sigma_H \propto n$,[18] as expected for the IQHE. It can be shown that in the presence of disorder (as in section 2.2.4), only the extended states undergo spectral flow, preserving the proportionality $\sigma_H \propto n$.

2.4.2 Spectral flow of Laughlin states

The Laughlin states (2.13) have the same single-particle basis as was used in the derivation above. The difference in a Laughlin state's response to flux insertion lies solely in the lower density of (usually) equally spaced particles. See section 2.3.4 for details on the spacing of single-particle states in a Laughlin state, and the notation used here.

Under flux insertion, the single particle states undergo the same shift as before. However, in the case of the Laughlin state at $\nu = 1/m$, it takes an insertion of $\Phi = m\Phi_0$ to

[18] We here identify the response of the system to flux insertion as σ_H, because it is the perpendicular (in this case radial) response to a change in magnetic field.

transport a single charge across the system:[19]

$$\begin{aligned} & 100100100100|000\cdots \\ \xrightarrow{\Phi=\Phi_0} \; & 010010010010|000\cdots \\ \xrightarrow{\Phi=2\Phi_0} \; & 001001001001|000\cdots \\ \xrightarrow{\Phi=3\Phi_0} \; & 000100100100|100\cdots . \end{aligned}$$

Thus, for Laughlin states, flux insertion reproduces a Hall conductivity $\sigma_H \propto \Delta q/\Delta\Phi = \nu$, which is consistent with FQH predictions.

2.5 Chern numbers

As we will exploit later in this thesis, there is a deep connection between the QHE and topology. This connection can be understood through the *Berry phase* (Berry, 1984), which is a phase factor picked up by a system undergoing a cyclic adiabatic process. By the adiabatic theorem, a state parameterised by some parameters $\{\lambda_i\}$ must, in the absence of level crossings,[20] return to itself up to a phase factor if the $\{\lambda_i\}$ trace a closed loop:[21]

$$\begin{aligned} \{\lambda_i\} &\xrightarrow{\text{closed loop}} \{\lambda_i\} \\ |\psi(\lambda_i)\rangle &\longrightarrow e^{i\gamma}|\psi(\lambda_i)\rangle . \end{aligned} \tag{2.32}$$

The phase factor $e^{i\gamma}$ consists of a dynamical contribution $e^{iET/\hbar}$ (where T is the time taken to shift the parameters) as well as the Berry phase. We can derive this phase starting from the time-dependent Schrödinger equation

$$i\hbar\frac{\partial|\psi\rangle}{\partial t} = \hat{H}(\lambda_i(t))|\psi\rangle , \tag{2.33}$$

where we associate an 'instantaneous ground state' $|n(\lambda_i(t))\rangle$ with the Hamiltonian $\hat{H}$ at every time t. Setting the associated ground state energy $\epsilon_0 = \hat{H}(\lambda_i(t))|n(\lambda_i(t))\rangle = 0$ will remove the dynamic contribution from our derivation.

We pick $|n(\lambda_i(t=0))\rangle = |\psi(t=0)\rangle$ and $|\psi(t)\rangle = U(t)|n(\lambda_i(t))\rangle$, where $U(t)$ is a time-dependent phase factor satisfying $U(0) = 1$. Plugging this into (2.33), we find

$$\langle\psi|\frac{\partial\psi}{\partial t}\rangle = U^*\frac{\mathrm{d}U}{\mathrm{d}t} + \langle n|\frac{\partial n}{\partial t}\rangle = 0, \tag{2.34}$$

where (2.33) results in the 0 on the right hand side due to the choice of $|\psi\rangle$ as the ground state of H. We can rewrite this using the *Berry connection*

$$\mathcal{A}_i(\lambda) = -i\langle n|\frac{\partial}{\partial\lambda_i}|n\rangle , \tag{2.35}$$

[19] Note that we place the edge of the system a few 'steps' into the vacuum here, to make the transport of charge more clearly visible

[20] More formally, we assume that the ground state of the system is non-degenerate, and that the gap above the ground state does not close at any point in the adiabatic process.

[21] Note that in the second line and following text, $\{\lambda_i\}$ has been replaced by λ_i. This is purely for easier reading, the state $|\psi\rangle$ is taken to depend on *all* parameters λ_i.

to obtain

$$U^* \frac{\mathrm{d}U}{\mathrm{d}t} = -\langle n| \frac{\partial n}{\partial t}\rangle = -\langle n| \frac{\partial}{\partial \lambda_i} |n\rangle \frac{\mathrm{d}\lambda_i}{\mathrm{d}t} \tag{2.36}$$

$$\Rightarrow \frac{\mathrm{d}U}{\mathrm{d}t} = -i\mathcal{A}_i \frac{\mathrm{d}\lambda_i}{\mathrm{d}t} U, \tag{2.37}$$

which gives us

$$U(t) = \exp\left[-i \int \mathcal{A}_i(\lambda) \frac{\mathrm{d}\lambda_i}{\mathrm{d}t} \mathrm{d}t\right]. \tag{2.38}$$

For a closed loop $\mathcal{C}$, this phase factor yields the Berry phase:

$$e^{i\gamma} = \exp\left[\oint_{\mathcal{C}} \mathcal{A}_i(\lambda)\, \mathrm{d}\lambda_i\right]. \tag{2.39}$$

This same expression can be obtained from the *Berry curvature*:

$$\mathcal{F}_{ij}(\lambda) = \frac{\partial \mathcal{A}_i}{\partial \lambda_j} - \frac{\partial \mathcal{A}_j}{\partial \lambda_i} \tag{2.40}$$

with which

$$e^{i\gamma} = \exp\left[i \iint_{\mathcal{S}} \mathcal{F}_{ij}\, \mathrm{d}\mathcal{S}_{ij}\right], \tag{2.41}$$

with $\mathcal{S}$ the (parameter space) surface bounded by $\mathcal{C}$.

It turns out that the integral in (2.41) over a closed surface $\mathcal{S}$ has to be quantised due to the Gauss-Bonnet theorem or, more generally, the Chern theorem (Chern, 1945):

$$\oiint_{\mathcal{S}} \mathcal{F}_{ij}\, \mathrm{d}\mathcal{S}_{ij} = 2\pi C, \tag{2.42}$$

where $C \in \mathbb{Z}$ is a so-called *topological invariant* (i.e., it is a quantised number unsusceptible to smooth deformations of the underlying parameter space), called the *Chern number*. We can now connect the Chern number to the QHE.

The connection between Chern numbers and QH physics becomes most clear when we place a state with Hamiltonian (2.1) on the torus $\mathbb{T}^2$. Threading fluxes Φ_x and Φ_y through both cycles of the torus corresponds to perturbing the Landau gauge:

$$\mathbf{A} = Bx\hat{\mathbf{y}} \rightarrow \frac{\Phi_x}{L_x}\hat{\mathbf{x}} + \left(\frac{\Phi_y}{L_y} + Bx\right)\hat{\mathbf{y}}. \tag{2.43}$$

These fluxes now parameterise the Hamiltonian. However, the spectrum of the Hamiltonian depends only on $\Phi_x \mod \Phi_0$ and $\Phi_y \mod \Phi_0$, as can be derived from spectral flow arguments. Thus, the parameter space is a torus too. In terms of dimensionless parameters $\theta_i = 2\pi\Phi_i/\Phi_0$, we have $(\theta_x, \theta_y) \in \mathbb{T}^2$.

Using the θ_i, we can now define a Berry connection and curvature:

$$\mathcal{A}_i = -i\langle \psi_0| \frac{\partial}{\partial \theta_i} |\psi_0\rangle \tag{2.44}$$

$$\mathcal{F}_{ij} = \frac{\partial \mathcal{A}_x}{\partial \theta_y} - \frac{\partial \mathcal{A}_y}{\partial \theta_x} = -i\left[\frac{\partial}{\partial \theta_y}\langle \psi_0| \frac{\partial \psi_0}{\partial \theta_x}\rangle - \frac{\partial}{\partial \theta_x}\langle \psi_0| \frac{\partial \psi_0}{\partial \theta_y}\rangle\right]. \tag{2.45}$$

This last expression can be identified as the Hall conductivity σ_{xy} as would be derived

from the Kubo formula. Averaging the expression over the entire parameter space $\mathbb{T}^2$, we find

$$\sigma_{xy} = -\frac{e^2}{\hbar} \iint_{\mathbb{T}^2} \frac{\mathrm{d}^2\,\boldsymbol{\theta}}{(2\pi)^2} \mathcal{F}_{ij} = -\frac{e^2}{2\pi\hbar} C, \tag{2.46}$$

with $C \in \mathbb{Z}$ per (2.42). Thus, the Hall conductivity is given by the Chern number, giving another basis for the integer quantisation of the integer quantum Hall effect.

2.6 Quantum Hall states on the lattice: Chern insulators

All of the discussion on the QHE so far has focussed exclusively on particles in the continuum. However, for most of this thesis, we will actually study particles on a *lattice*, rather than the continuum. We thus need to port our understanding of the QHEs to lattice models. Lattice generalisations of QH states are called Chern insulators (CIs), a subclass of topological insulators, which exist for both the integer and fractional case (Haldane, 1988; Hasan and Kane, 2010; Regnault and Bernevig, 2011; Bergholtz and Liu, 2013; Parameswaran, Roy, and Sondhi, 2013).

On a square lattice with lattice spacing $a = 1$, a state's lattice momentum falls within the Brillouin zone:

$$-\pi \leq k_x \leq \pi, \quad -\pi \leq k_y \leq \pi, \tag{2.47}$$

Which, with periodic boundary conditions in both dimensions, is equivalent to the torus $\mathbb{T}^2$. We can write the wave functions in Bloch form:

$$\psi_{\mathbf{k}}(\mathbf{r}) = e^{i\mathbf{k}\mathbf{r}} u_{\mathbf{k}}(\mathbf{r}), \tag{2.48}$$

where $u_{\mathbf{k}}(\mathbf{r})$ is constrained to be periodic on some unit cell.

We can now define a Berry connection (2.35) on the $\mathbb{T}^2$ Brillouin zone as

$$\mathcal{A}_i(\mathbf{k}) = -i \langle u_{\mathbf{k}} | \frac{\partial}{\partial k_i} | u_{\mathbf{k}} \rangle . \tag{2.49}$$

This, through the Berry curvature (2.40) allows us to associate a Chern number (also known as TKNN invariant, due to Thouless et al. (1982), in this case) to the band in which the $u_{\mathbf{k}}$ live:

$$C = \frac{1}{2\pi} \iint_{\mathbb{T}^2} \mathrm{d}^2\mathbf{k} \mathcal{F}_{xy}, \tag{2.50}$$

such that we can associate a Chern number $C_n \in \mathbb{Z}$ with each band n.

The Hall conductivity of a non-interacting band insulator (i.e., with the Fermi energy or chemical potential lying in the gap between two bands) can be expressed in terms of Chern numbers as

$$\sigma_{xy} = \frac{e^2}{2\pi\hbar} \sum_{n \in \mathrm{occ}} C_n, \tag{2.51}$$

where the sum is over all occupied bands.

It is a curious property of Chern insulators to still generate a QHE in the absence of a magnetic field (although time-reversal symmetry is required to be broken in another way). This is called the *quantum anomalous Hall effect* (QAHE). This thesis does not cover the QAHE as such. Rather, we will consider QH effects on the lattice as arising due to a non-zero Aharonov-Bohm phase.[22] The model describing this system is the Harper-Hofstadter model, an introduction to which will be given in chapter 4.

[22] Note that on the lattice, magnetic fields can be defined modulo a flux Φ_0 per lattice plaquette only, which precludes a fundamental distinction between cases with or without a magnetic field.

Chapter 3

Matrix Product States and the Density Matrix Renormalization Group

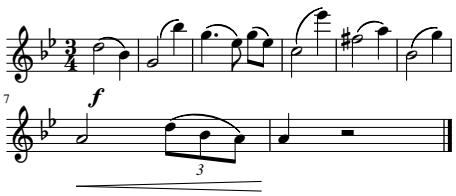

Johannes Brahms, *Clarinet Sonata, Op. 120 No. 1*

This chapter is an introduction to Matrix Product States (MPSs), Matrix Product Operators (MPOs) and the Density Matrix Renormalization Group (DMRG). In section 3.1, the (graphical) notation used to describe MPSs and MPOs, as well as the cost of tensor contractions, are introduced. Section 3.2 describes the MPS formalism in detail. Section 3.3 introduces MPOs and their construction. Section 3.4 then explains the details of the DMRG method. Finally, section 3.6 provides a protocol for how to approach problems in physics using DMRG.

3.1 Basics

In this section, we will briefly introduce the notation we use for Tensor Networks (TNs), as well as the computational cost of contracting tensors.

3.1.1 Notation

In working with MPSs and other TN representations, it is useful to adopt a graphical notation often attributed to Penrose (1971). This notation is based on representing any tensor (including scalars, vectors and matrices) as a 'shape' with 'legs'. An example of this notation is found in figure 3.1. Operations such as tensor contraction, reshaping and relabelling of the indices of a tensor (the latter two of which are mostly useful for numerical implementations, rather than for algebraic work) can then be described in this diagrammatic formalism (figure 3.2).

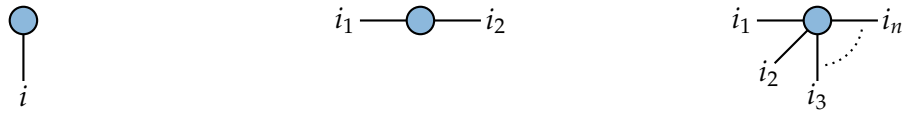

(A) A vector. (B) A matrix. (C) An order-n tensor.

FIGURE 3.1: Examples of the graphical notation for mathematical objects. 'Legs' correspond to indices i (or i_n).

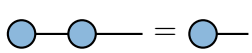

(A) Vector-matrix contraction: $\sum_i M_{ij} v_i$.

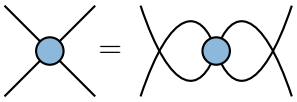

(B) Reordering the indices of an order-4 tensor: e.g., $T_{ijkl} \to T_{jilk}$.

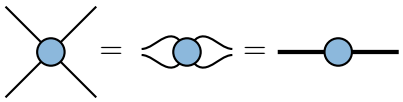

(C) Reshaping an order-4 tensor into a matrix: e.g., $T_{ijkl} \to M_{[ij],[kl]}$ with $[ij]$ ($[kl]$) denoting a 'combined index' from indices i and j (k and l). The thicker legs on the right hand 'expression' indicate that the legs are formed of a combination of two legs, and thus have a bigger dimension.

FIGURE 3.2: Elementary tensor operations in the diagrammatic formalism.

3.1.2 Cost of tensor contractions

In general, the computational cost of a tensor contraction scales as the product of the dimension of all the indices involved, including both 'open' and 'closed' (or contracted) indices. More precisely, the computational cost of the contraction of two tensors A and B with leg dimensions $\{ d_\alpha^A \}$ and $\{ d_\beta^B \}$, respectively, is

$$\text{cost} = \prod_\alpha d_\alpha^A \prod_\beta d_\beta^B \Big/ \prod_{d \in A \cap B} d, \tag{3.1}$$

where the denominator (product over all contracted legs) is there to avoid double-counting. Thus, the contraction shown in figure 3.2a would have an associated cost of $\mathcal{O}(d^2)$, assuming all legs have dimension d. The cost of contracting the leftmost two tensors in the left image in figure 3.8a (using an example from later in this chapter) would be $\mathcal{O}(d^5)$.

3.2 Matrix Product States

An MPS (Fannes, Nachtergaele, and Werner, 1992; Ostlund and Rommer, 1995; Vidal, 2003; Vidal, 2004; Perez-Garcia et al., 2007), also known as Tensor Train in more mathematically-oriented literature (Oseledets, 2011), forms an ansatz for the efficient representation of a quantum many-body state. We start by writing a general n-body state:

$$|\psi\rangle = \sum_{i_1, i_2, \ldots, i_N} c_{i_1, i_2, \ldots, i_N} |i_1, i_2, \ldots, i_N\rangle . \tag{3.2}$$

We now represent the coefficients $c_{i_1, i_2, \ldots, i_N}$ as a product of matrices (or, more accurately, tensors):

$$c_{i_1, i_2, \ldots, i_N} = A^{i_1}_{\alpha_1} A^{i_2}_{\alpha_1 \alpha_2} A^{i_3}_{\alpha_2 \alpha_3} \cdots A^{i_{N-1}}_{\alpha_{N-2} \alpha_{N-1}} A^{i_N}_{\alpha_{N-1}} \tag{3.3}$$

$$\Rightarrow |\psi\rangle = \sum_{i_1, i_2, \ldots, i_N} A^{i_1} A^{i_2} \cdots A^{i_{N-1}} A^{i_N} |i_1, i_2, \ldots, i_N\rangle , \tag{3.4}$$

where in the first line we used implicit summation over all duplicated indices (i.e., the Einstein convention), and in the second line we completely omitted the indices α_i for brevity.[1]

This decomposition of the many-body coefficients into a product of a set of tensors can be represented graphically using the notation from section 3.1.1 (figure 3.3). The legs in the figure again correspond to the indices of the tensors; when discussing tensor networks the legs are often called *bonds*.

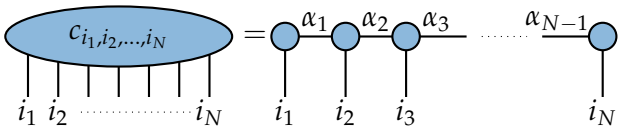

FIGURE 3.3: The decomposition of a many-body state into an MPS (equation 3.3). We follow the convention that an MPS with its legs down corresponds to a state (or ket state) $|\psi\rangle$, whereas an MPS with its legs up (the vertical mirror image of what is shown here) is a costate (or bra state) $\langle\psi|$, where we assume implicit complex conjugation of the bra tensors.

3.2.1 MPS dimensions

The different bonds/indices in an MPS (figure 3.3 and equation 3.4, respectively) have different dimensions. The vertical bonds, labelled with the i_n, are the *physical* legs (corresponding to the local Hilbert space of the actual physical system), which carry *physical dimension* d. The horizontal bonds, created by the construction of the MPS, are *virtual* or *auxiliary* bonds of *bond dimension* (sometimes called *bond order*) χ. The auxiliary bonds carry all information about correlations between the sites of the physical system.

To describe a generic many-body state exactly using an MPS, the bond dimension typically scales exponentially with the length of the chain. This can easily been shown by considering the decomposition in figure 3.3 and equation 3.4 as arising from sequential SVDs, as will be discussed in section 3.2.3. Assuming all physical dimensions $d_i = d$ are equal, we will obtain $\chi_1 = d, \chi_2 = d^2, \cdots, \chi_{N/2} = d^{N/2}, \cdots, \chi_{N-2} = d^2, \chi_{N-1} = d$. To avoid the computational cost this would incur, the bond dimension is *truncated* down to a fixed value $\chi_{\max}$. The process by which this is done and the justification for this procedure will be explained in section 3.2.3. However, we will first introduce an example of a system with an exact MPS representation at $\chi = 2$.

3.2.2 Example: the AKLT model

The Affleck-Kennedy-Lieb-Tasaki model (Affleck et al., 1987; Affleck et al., 1988) is a particular construction of a spin-1 model satisfying the Hamiltonian

$$H_{\text{AKLT}} = \sum_i \mathbf{S}_i \cdot \mathbf{S}_{i+1} + \frac{1}{3}\left(\mathbf{S}_i \cdot \mathbf{S}_j\right)^2 \tag{3.5}$$

on a chain, where the $\mathbf{S}$ are spin-1 operators. In the ground state of this model (by construction), each spin-1 site on the chain is formed of two spin-$\frac{1}{2}$ states, where the spin-$\frac{1}{2}$ states of neighbouring sites form a singlet state $\frac{1}{\sqrt{2}}(|\uparrow\downarrow\rangle - |\downarrow\uparrow\rangle)$. This singlet state is

[1] Note that we here describe a state with open boundary conditions, i.e., the state 'ends' at the first and last tensor A. This is why A^{i_1} and A^{i_N} only have a single index α_i. For periodic boundary conditions, the product of matrices in (3.3) and (3.4) is replaced by a trace $A^{i_1}_{\alpha_0\alpha_1} \cdots A^{i_N}_{\alpha_{N-1}\alpha_0}$, where the MPS bond effecting the boundary condition is labelled by α_0 and the trace is implicit by the summation convention.

sometimes called a *valence bond*, which is the reason the many-body state is also called a *valence bond solid*. A graphical depiction of the Affleck-Kennedy-Lieb-Tasaki ground state is given in figure 3.4.

The spin-1 states can be described in terms of the spin-$\frac{1}{2}$ states:

$$\begin{cases} |+\rangle &= |\uparrow\uparrow\rangle \\ |0\rangle &= \frac{1}{\sqrt{2}}\left(|\uparrow\downarrow\rangle + |\downarrow\uparrow\rangle\right) \\ |-\rangle &= |\downarrow\downarrow\rangle\,, \end{cases} \tag{3.6}$$

which allows us to define a projector from the spin-1 space onto the spin-$\frac{1}{2}$ triplet subspace resulting from the decomposition $\frac{1}{2} \otimes \frac{1}{2} = \text{singlet} \oplus \text{triplet}$, with the triplet states given in the right hand side of (3.6) and the singlet state being the familiar $\frac{1}{\sqrt{2}}\left(|\uparrow\downarrow\rangle - |\downarrow\uparrow\rangle\right)$. Denoting the spin-1 states with a σ, we have

$$M^{\sigma}_{ab}\,|\sigma\rangle\,\langle ab|\,, \tag{3.7}$$

where

$$M^{-} = \begin{pmatrix} 0 & 0 \\ 0 & 1 \end{pmatrix}, \quad M^{0} = \begin{pmatrix} 0 & 1/\sqrt{2} \\ 1/\sqrt{2} & 0 \end{pmatrix}, \quad M^{+} = \begin{pmatrix} 1 & 0 \\ 0 & 0 \end{pmatrix}. \tag{3.8}$$

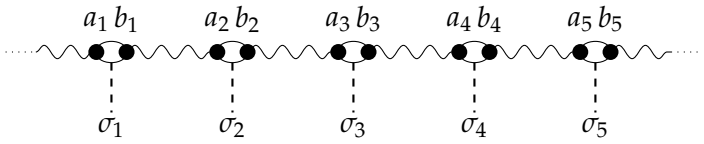

FIGURE 3.4: The Affleck-Kennedy-Lieb-Tasaki (ground) state. Squiggly lines denote the spin-$\frac{1}{2}$ singlet states $\frac{1}{\sqrt{2}}(|\uparrow\downarrow\rangle - |\downarrow\uparrow\rangle)$, while ellipses give the composite spin-1 states $|+\rangle, |-\rangle$ or $|0\rangle$. Every spin-$\frac{1}{2}$ is labeled by either an a_i or a b_i, the spin-1 states are labeled by the σ_i. The map between the spin-$\frac{1}{2}$ and the spin-1 states is given in equation (3.8)

We can now generically describe the full state as

$$|\psi\rangle = \sum_{\{a\},\{b\}} c_{\{a\},\{b\}}\,|\{a\},\{b\}\rangle\,, \tag{3.9}$$

where the $\{a\}$ and $\{b\}$ denote the full set of all spin-$\frac{1}{2}$ states and $c_{\{a\},\{b\}}$ is a coefficient depending on these local states (compare equation 3.2). The singlet states coupling every b_i with an a_{i+1} are

$$S^{[i]} = \sum_{b_i, a_{i+1}} S_{b_i, a_{i+1}}\,|b_i\rangle\,|a_{i+1}\rangle\,, \tag{3.10}$$

with

$$S = \begin{pmatrix} 0 & 1/\sqrt{2} \\ -1/\sqrt{2} & 0 \end{pmatrix}. \tag{3.11}$$

The ground state lies within the space of (products of) singlet states:

$$|\psi_{\mathrm{GS}}\rangle = \sum_{\{a\},\{b\}} S_{b_1,a_2} S_{b_2,a_3} \ldots S_{b_{L-1},a_L} S_{b_L,a_1}\,|\{a\}\rangle\,|\{b\}\rangle\,. \tag{3.12}$$

Applying the map from equation 3.8 to the state in equation 3.12, we get a spin-1 state

$$|\tilde{\psi}_{\mathrm{GS}}\rangle = \sum_{\{\sigma\}} \sum_{\{a\},\{b\}} M^{\sigma_1}_{a_1 b_1} S_{b_1,a_2} M^{\sigma_2}_{a_2 b_2} S_{b_2,a_3} \dots M^{\sigma_L}_{a_L b_L} S_{b_L,a_1}, \tag{3.13}$$

which, under the identification $A^{\sigma_i}_{a_i a_{i+1}} = M^{\sigma_i}_{a_i b_i} S_{b_i,a_{i+1}}$, becomes

$$|\tilde{\psi}_{\mathrm{GS}}\rangle = \sum_{\{\sigma\}} \mathrm{Tr}\left(A^{\sigma_1} A^{\sigma_2} \dots A^{\sigma_L}\right) |\{\sigma\}\rangle\,, \tag{3.14}$$

in which we recognize a MPS of the form in equation 3.4. Because all matrices M, S and A are 2×2, this MPS has bond dimension $\chi = 2$.

Several notes about the construction above should be pointed out. Firstly, at no point during the derivation was an explicit attempt made to normalise the ground state (and in fact, it is not normalised when using the exact matrices described). However, it is fairly straightforward to calculate normalization factors. Secondly, note that (3.12) and (3.13) have explicitly periodic boundary conditions (resulting in the trace in (3.14)), while in (3.3) open boundary conditions were used. The derivation works in general for both boundary conditions.

The ground state (3.14) is unique for the model on periodic boundary conditions. In contrast, the state for an open chain (with the trace in (3.14) replaced by a sum, and the first and last tensors in (3.8) and (3.13) having one fewer index) gives rise to a ground state degeneracy. This degeneracy is due to the spin-$\frac{1}{2}$states at the edges of the system (compare figure 3.4) being unbounded by a singlet state (or valence bond), and is four-fold in the limit of large chains (where the edge spins decouple). An early use of DMRG was to directly observe these edge states (White and Huse, 1993).

3.2.3 Schmidt decomposition, SVD and entanglement entropy

To understand why MPSs are useful, we have to take a closer look at the bond dimension and its connection with the entanglement entropy. To do this, we first investigate an alternative way to construct an MPS. This method relies on the Singular Value Decomposition (SVD), which is a decomposition of a matrix

$$M = USV^\dagger, \tag{3.15}$$

where U and $V^\dagger$ are *isometries*, satisfying $U^\dagger U = V^\dagger V = \mathbb{1}$ (but not necessarily $UU^\dagger = \mathbb{1}$ or $VV^\dagger = \mathbb{1}$). The matrix S is a diagonal matrix containing the *singular values*, s_i, which are real and non-negative ($s_i \geq 0$). Typically, the s_i are ordered in descending order, such that for any $i < j$, we have $s_i \geq s_j$.

Starting again from the many-body coefficient of equation 3.3 and figure 3.3, we can perform a sequence of SVDs to create the MPS. This process is described in figure 3.5.

The singular values are equal to the Schmidt coefficients of a decomposition of the state in two halves, which has the form

$$|\psi\rangle = \sum_i s_i\, |\chi^L_i\rangle \otimes |\chi^R_i\rangle\,. \tag{3.16}$$

For this, the cut of the system into a left and a right half has to be done at the bond where the singular values were obtained. (Alternatively, one can interpret the singular values as the square roots of the eigenvalues of the reduced density matrix ρ_L.)

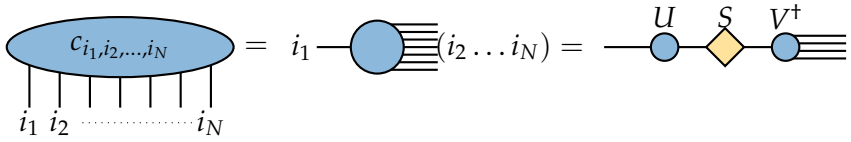

(A) A single SVD is performed by first grouping together all but one legs of the tensor (first step), to change the tensor into a matrix. This matrix is then decomposed into a product $USV^\dagger$ (second step), where U and $V^\dagger$ are unitary matrices and S is diagonal, real and positive.

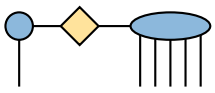

(B) After the first Singular Value Decomposition, the indices of the rightmost tensor can be split up again by grouping the left (virtual) leg and leftmost physical leg, then performing another SVD as in figure 3.5a.

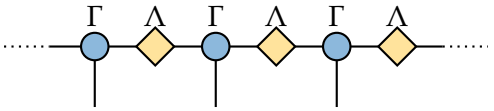

(C) The final result after a sequence of SVDs. The tensors have been relabelled Γ and Λ conform the literature.

FIGURE 3.5: Creating an MPS by successive SVDs.

The identification with Schmidt coefficients allows us to directly compute the entanglement entropy across a given cut from the singular values, which quantifies the information shared between the two halves of the system separated by the cut. Different expressions for the entanglement entropy are possible:

$$S = -\sum_i s_i^2 \log s_i^2 \qquad \text{Von Neumann} \qquad (3.17a)$$

$$S_\alpha = \frac{1}{1-\alpha} \log \left(\sum_i s_i^{2\alpha} \right). \qquad \text{Rényi,} \qquad (3.17b)$$

Where the Rényi entanglement entropy reduces to the Von Neumann entanglement entropy in the limit $\alpha \to 1$.

Because of the ordering of the singular values, the 'first' singular values contribute more to the entanglement entropy than the 'later' values. The goal is now to truncate the spectrum of singular values at a fixed bond dimension χ so as to avoid the exponential growth mentioned at the end of section 3.2.1, while keeping most of the entanglement information. This translates to making a 'cut' in the Schmidt spectrum (3.16) or limiting the dimension of the singular value matrix S in (3.15), such that only comparatively small values are discarded.

Luckily, there have been rigorous proofs that gapped, local[2] Hamiltonians for 1D systems obey an *area law* (Hastings, 2007; Eisert, Cramer, and Plenio, 2010), which states that after some initial growth, the scaling of entanglement entropy with system size is constant: $S(L) \sim c$. This allows us to truncate all bonds at a finite bond dimension for any system size while retaining a good approximation to the exact state (Verstraete and Cirac, 2006). In terms of the singular values or Schmidt spectrum, these proofs show an exponential decay of the values with their index, ensuring only the smallest values are ignored.

The downside to the effectiveness of this truncation is that it does not hold for gapless (critical) systems, where $S(L) \sim \log L$, or for 2D systems, where $S(L_x, L_y) \sim L_y$[3] (if the

[2] By "local", we here mean any interaction that results in an exponentially decaying correlation length.
[3] Here, we assume a system that is infinite along $\hat{\mathbf{x}}$. See section 3.4.4 for details.

Hamiltonian is gapped; for gapless Hamiltonians the scaling is even worse). Therefore, for these systems the MPS approximation is somewhat limited.

A measure for how well an MPS represents the actual state can be given by the *truncation* error:

$$\epsilon = \sum_{i>\chi_{\max}} s_i^2. \tag{3.18}$$

This quantifies the total weight of the discarded singular values upon truncating at $\chi_{\max}$.

3.2.4 Transfer Matrix

For many applications, it is more useful to work with a *transfer matrix* than with the MPS itself. This is particularly true if one wants to study infinite systems (Ueda, Gendiar, and Nishino, 2010). To get to the transfer matrix, we first rewrite the MPS as[4]

$$\begin{aligned} |\psi\rangle = \sum_{\{\sigma,\alpha,\beta\}} \Big(\cdots \Gamma^{\sigma_{i-1}}_{\alpha_{i-1},\beta_{i-1}} \Lambda_{\beta_{i-1},\alpha_i} \Gamma^{\sigma_i}_{\alpha_i,\beta_i} \Lambda_{\beta_i\alpha_{i+1}} \\ \times \Gamma^{\sigma_{i+1}}_{\alpha_{i+1},\beta_{i+1}} \Lambda_{\beta_{i+1},\alpha_{i+1}} \cdots \Big) |\{\sigma\}\rangle , \end{aligned} \tag{3.19}$$

which we already encountered in graphical form in figure 3.5c. From the Γ's and Λ's we can now define the transfer matrix:

$$T_{i;\alpha,\beta,\alpha',\beta'} = \sum_{\sigma_i} \Gamma^{\sigma_i}_{\alpha_i\beta_i} (\Gamma^{\sigma_i}_{\alpha'_i\beta'_i})^* \Lambda_{\beta_i,\alpha_{i+1}} \Lambda^*_{\beta'_i,\alpha'_{i+1}}, \tag{3.20}$$

where i labels the position of the transfer matrix in the chain, and the α and β are the open indices. See figure 3.6a. By including the Λ's to the left of the Γ's in the transfer matrix instead of the ones to the right (i.e., replacing $\Lambda_{\beta_i,\alpha_{i+1}}$ with $\Lambda_{\beta_{i-1},\alpha_i}$ and similar for the conjugate), one obtains the 'opposite' transfer matrix; the two different transfer matrices are generally called the *left* and *right* transfer matrices T_L and T_R.

Using transfer matrices, one can define the *canonical form* of an MPS. A transfer matrix of a canonical form MPS has an eigenvector $\mathbb{1}$ with eigenvalue 1 (figure 3.6b). We can distinguish between *left canonical*, *right canonical* and *mixed canonical* forms. An MPS in left canonical form has all transfer matrices satisfying the exact expression in figure 3.6b. A right canonical MPS satisfies the same expression, but for its right transfer matrices T_R, i.e., it satisfies the mirror image of figure 3.6b. An MPS in mixed canonical form satisfies the left canonical condition for all transfer matrices to the left of some 'central' site i, and the right canonical condition for all transfer matrices to the right of this site.

The canonical form allows for some simplifications of the DMRG method (see section 3.4) later on, as well as for relatively straightforward work with (projective) symmetries (Pollmann and Turner, 2012). Additionally, the transfer matrix allows for easy computation of correlation lengths (McCulloch, 2008) through the spectrum of the matrix:

$$\lambda_2 = \exp\left[-\frac{1}{\xi}\right], \tag{3.21}$$

where ξ is the correlation length and λ_2 is the second eigenvalue of the transfer matrix (assuming the MPS is properly normalised, and thus the first eigenvalue is $\lambda_1 = 1$).

[4] Note that the physical state depends only on the physical spin indices denoted by σ, and not on the virtual indices denoted by α and β.

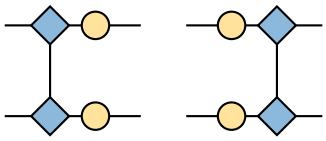

(A) Left and right transfer matrices T_L and T_R (equation 3.20), built up from two copies of Γ and Λ each (bottom row Γ is complex conjugate of top row Γ).

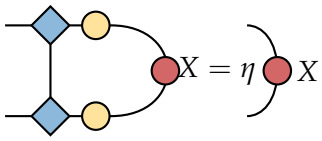

(B) The transfer matrix acting on eigenvector X yielding an eigenvalue η. If the transfer matrix is in canonical form, the pair $(\eta, X) = (1, \mathbb{1})$ satisfies this equation.

FIGURE 3.6: Diagrammatic representations of the MPS and transfer matrix.

3.2.5 Entanglement spectrum

Entanglement spectra have been hailed as a method to extract more information from the entanglement properties of a state than is available by looking only at the entanglement entropy (Li and Haldane, 2008). We can easily extract the entanglement spectrum from an MPS following from the Schmidt decomposition (3.16), as the spectrum is defined as the set $\{-\log \lambda_i\}$, where the λ_i are related to the Schmidt coefficients via $s_i^2 = \exp(-\lambda_i)$. Additional insights into the state can be obtained by resolving the quantum numbers of the eigenstates (akin to the 'splitting' into three sectors in Li and Haldane (2008)). This is easily done when the MPS is block diagonal in the quantum number sectors as explained in section 3.2.6.

3.2.6 Conservation of quantum numbers

Calculations with MPS are sped up by making the MPS and other relevant tensors respect the conservation of quantum numbers (e.g. spin and particle number) or 'charges'. These charges are the eigenvalues of any unitary operator U that commutes with the Hamiltonian, which allows for U and $\hat{H}$ to be diagonalised simultaneously, in turn enabling a description of $\hat{H}$ in terms of 'blocks' corresponding to the eigenvalues of U. Most commonly, $U(1)$ operators such as total spin or particle density are used (Singh, Pfeifer, and Vidal, 2010; Singh, Pfeifer, and Vidal, 2011), although other symmetries of the Hamiltonian (most notably $SU(2)$ symmetries) have been studied as well (Weichselbaum, 2012; Schmoll et al., 2020).

In practice, we associate quantum numbers with all indices of the MPS tensors (figure 3.7). The additive property of 'good' quantum numbers then allows us to only store those entries in the MPS tensors that obey this additivity (see figure 3.7 and table 3.1), as any other entry is necessarily zero. Through this procedure, we will obtain highly sparse tensors (of which only non-zero entries are stored) in both the MPS (table 3.1) as well as operators (section 3.3) that are block diagonal in the quantum number basis. This sparsity can be used to increase the memory efficiency of storing the MPS and to speed up calculations (by solving any linear algebra problems for the quantum number blocks rather than the full matrix).

3.2.7 Other tensor network state representations

While MPSs are widely known and used, they are not the only tensor network method for representing quantum many-body states. Three others are Tree Tensor Networks (TTN) (Shi, Duan, and Vidal, 2006; Tagliacozzo, Evenbly, and Vidal, 2009), the Multiscale Entanglement Renormalization Ansatz (MERA) (Vidal, 2007; Evenbly, 2010; Vidal, 2010; Evenbly and Vidal, 2009) and (infinite) Projected Entangled Pair States (or (i)PEPS)

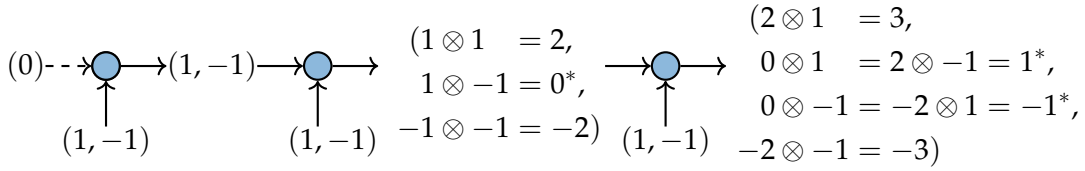

FIGURE 3.7: Conservation of quantum numbers (or 'charges') in MPS tensors. Shown are the first three MPS tensors from the left. The numbers in brackets indicate the set of quantum numbers corresponding to each bond. This system is a two-level system (e.g. a spin-$\frac{1}{2}$system, with the value of the spins normalized to ± 1 instead of $\pm\frac{1}{2}$). The leftmost bond is a 'dummy' bond, carrying a trivial charge of 0. At each site, two values for the quantum number are 'added' to the system: these are the values for the local up- and down state. Duplicate values on the auxiliary bonds are denoted with asterisks. The values at the rightmost bond can be interpreted as the total charge (in this case, the total magnetization) in the system. In fact, the values at each auxiliary bond correspond to the total quantum number for the part of the system to the left of that bond. It should be noted that for a generic 2-level system, the bond dimensions are expected to be $\chi = \{2, 4, 8, \dots\}$, which is still the case here. The gains from implementing conservation of quantum numbers are then not immediately visible in the MPS dimensions, but result from an induced sparsity of the MPS tensors. Any tensor element in e.g. the centre tensor pictured here that would 'couple' values $(1, 1)$ in the left and bottom incoming bond, respectively, to a value other than 2 on the right outgoing bond, would have to be 0 to respect the conservation law. This is perhaps more clear using tensor product notation: $1 \otimes 1 = 2$, while $1 \otimes 1 \neq 0$. All values of the centre tensor are listed in table 3.1, from which it is clear that only 6 out of the 16 elements are nonzero.

Left (in)	1	1	1	1	1	1	-1	-1	-1	-1	-1	-1
Bottom (in)	1	1	1	-1	-1	-1	1	1	1	-1	-1	-1
Right (out)	2	0	-2	2	0	-2	2	0	-2	2	0	-2
Value	$\neq 0$	0*	0	0	$\neq 0$*	0	0	$\neq 0$*	0	0	0*	$\neq 0$

TABLE 3.1: Indicating which entries in the centre tensor in figure 3.7 are (non-)zero. Values with an asterisk in the bottom row occur twice due to the duplicity of the value 0 on the right bond. Highlighted columns denote potentially non-zero entries. We can clearly see that there are (at most) 6 non-zero values out of a total of 16.

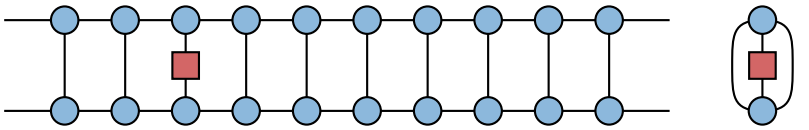

(A) One-body operator. In the right image the problem is simplified using the mixed canonical form.

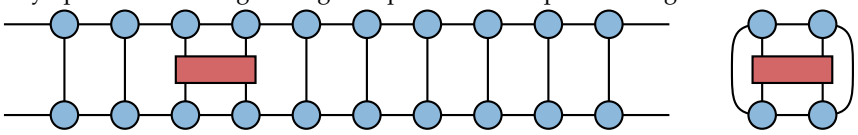

(B) Two-body operator. In the right image the problem is simplified using the canonical form.

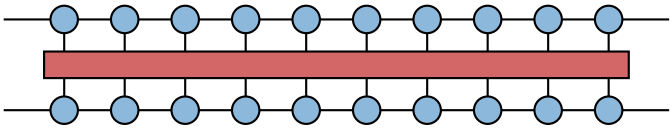

(C) Global operator. Simplification using the canonical form is not possible in this case.

FIGURE 3.8: Expectation values $\langle\psi|O|\psi\rangle$, consisting of an operator 'sandwiched' between two copies of an MPS.

(Nishino and Okunishi, 1996; Verstraete and Cirac, 2004; Corboz et al., 2010; Bauer et al., 2011; Orús, 2014).

TTN and MERA both rely on explicit real-space course-graining through the use of tensor *isometries* that map the state on one real-space 'level' to a state on a course-grained level. TTN consist only of these isometries, while MERA contains additional unitary *disentanglers*, designed to renormalise the entanglement between sites at each real-space level. Due to their structure, both methods are more expensive to use than MPS, but are better suited to study critical (gapless) systems. (In fact, while MPS can only describe systems with exponentially decaying correlation lengths accurately, MERA can describe power law decaying correlation lengths to the same precision.) Both methods can readily be generalized to two dimensions.

(i)PEPS is a two-dimensional analogue to MPS. It typically consists of rank-5 tensors on a (square) lattice, where four of the indices are auxiliary indices along the lattice and the fifth is the physical index (just like in MPS). (i)PEPS is capable of working in the thermodynamic limit in both of the two dimensions (rather than MPS, which is limited to a finite size in one of the dimensions), but calculations with (i)PEPS tend to be significantly more expensive than calculations with MPS. Several ways of working with (i)PEPS are known, most commonly the *boundary MPS* (Cirac et al., 2011) and the *Corner Transfer Matrix* (CTM) method (Nishino and Okunishi, 1996; Nishino and Okunishi, 1997), which is based on early work by Baxter (Baxter, 1968; Baxter, 1978).

3.3 Matrix Product Operators

Now that we have a matrix product description of many-body quantum states, the natural next step is to consider operators. Figure 3.8 shows diagrammatic expressions for the expectation value for several operators (one-body, two-body and global). While for local operators, the calculation is simplified a lot by using the canonical form of the MPS, the computation gets increasingly more expensive for longer range operators and is not possible at all for global operators. The contraction of figure 3.8c would have a computational cost that scales exponentially with system size.

Because Hamiltonians (at least when taken at surface value) tend to be global operators, it is clear that it would be beneficial to define an MPS analogue of operators.

This analogue is given by Matrix Product Operators (MPOs) (Verstraete, García-Ripoll, and Cirac, 2004; McCulloch, 2007; Pirvu et al., 2010; Fröwis, Nebendahl, and Dür, 2010), which look diagrammatically like figure 3.9.

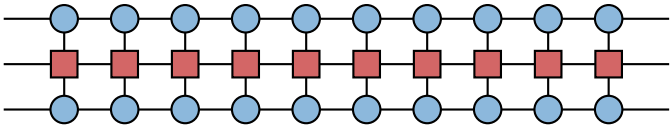

FIGURE 3.9: An expectation value $\langle\psi|O|\psi\rangle$, where the operator O is represented as an Matrix Product Operator.

3.3.1 Finite State Machines

The question now is how to turn a Hamiltonian into an MPO, preferably as an exact representation. While this can sometimes be done by direct inspection of the Hamiltonian, the procedure can be made more rigorous by using a Finite State Machine (FSM) (Crosswhite and Bacon, 2008).[5] This is best explained with an example, which we will take to be the XXZ Heisenberg model. This model is described by Hamiltonian

$$H = \sum_i \frac{J}{2}\left(\hat{S}_i^+\hat{S}_{i+1}^- + \hat{S}_i^-\hat{S}_{i+1}^+\right) + J_z\hat{S}_i^z\hat{S}_{i+1}^z + h\hat{S}_i^z, \tag{3.22}$$

where there are a large number of implicit identity operators included, which can become apparent when writing out the sum in excruciating detail. The first term of (3.22) then becomes

$$\begin{aligned}\frac{J}{2}\Big(\hat{S}_1^+\otimes\hat{S}_2^-\otimes\mathbb{1}_3\otimes\mathbb{1}_4\otimes\cdots + \mathbb{1}_1\otimes\hat{S}_2^+\otimes\hat{S}_3^-\otimes\mathbb{1}_4\otimes\cdots \\ +\mathbb{1}_1\otimes\mathbb{1}_2\otimes\hat{S}_3^+\otimes\hat{S}_4^-\otimes\cdots+\cdots\Big).\end{aligned} \tag{3.23}$$

We now imagine a 'machine' that moves along the chain from right to left (or left to right), generating the terms of the Hamiltonian above. On every site it encounters, it places one of the operators from the Hamiltonian. The machine keeps track of which operators it has already placed as its 'internal state', which influences the operators it is 'allowed' to place on the next site. Therefore, the FSM generating the XXZ Heisenberg Hamiltonian has 5 internal states (R, 1, 2, 3 and F, with R (F) corresponding to the 'Ready' ('Finished') state and states 1, 2 and 3 labelling the intermediate states in which one of the local operators $(J/2)\hat{S}^-$, $(J/2)\hat{S}^+$ or $J_z\hat{S}^z$ has been placed) with a total of 9 'transfer amplitudes' between these states (figure 3.10a). Each of the terms in (3.23) is now generated by a possible sequence of arrows followed through the Finite State Machine, with the entire Hamiltonian being a 'superposition' of all possible routes.

To generate the first term in (3.23), the Finite State Machine places $(J/2)\hat{S}^+$ on the first site, taking it to internal state 2. It can then only place $\hat{S}^-$ on the second site, bringing it to state F, where it will remain, placing identity operators $\mathbb{1}$ on all subsequent sites. For the second term in (3.23), the first operator placed is $\mathbb{1}$, which has the Finite State Machine remaining in state R. Then $(J/2)\hat{S}^+$ is placed on site 2 after which the process continues as described for the first term (only shifted by one site). Thus, by following all 'paths' where the Finite State Machine starts in state R and ends in state F *simultaneously*, the entire Hamiltonian (3.23) is generated.

[5] These are sometimes also known as Finite State *Automata*.

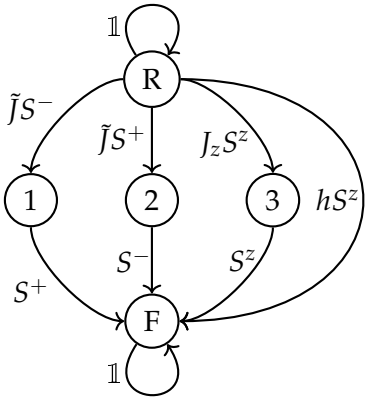

(A) Finite State Machine diagram for the XXZ Heisenberg Hamiltonian (equation 3.22). The circles denote the internal state of the Finite State Machine, to the left of each edge is the associated operator. States R and F are the 'Ready' and 'Finished' states, states 1, 2 and 3 are intermediate states. We have denoted $\tilde{J} = J/2$ for brevity.

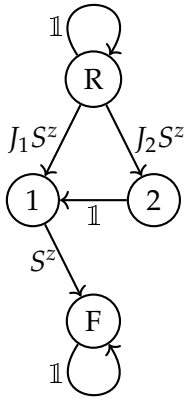

(B) Finite State Machine diagram for the next-nearest-neighbour Hamiltonian in equation 3.27.

FIGURE 3.10: Two examples of Finite State Machine diagrams.

The MPO tensors can now be constructed by taking the internal states of the FSM as a basis for a matrix of operators. Operators are then put into this matrix according to the transfer amplitudes from the FSM diagram. Choosing the basis ordering $(R, 1, 2, 3, F)$, the MPO tensor is

$$W = \begin{array}{c} \\ R \\ 1 \\ 2 \\ 3 \\ F \end{array} \begin{array}{c} \begin{array}{ccccc} R & 1 & 2 & 3 & F \end{array} \\ \begin{pmatrix} \mathbb{1} & & & & \\ (J/2)\hat{S}^- & & & & \\ (J/2)\hat{S}^+ & & & & \\ J_z\hat{S}^z & & & & \\ h\hat{S}^z & \hat{S}^+ & \hat{S}^- & \hat{S}^z & \mathbb{1} \end{pmatrix} \end{array}, \tag{3.24}$$

where only non-zero elements are shown for easier reading. We can clearly see that this matrix reproduces all processes in figure 3.10a. We take all the products in a given matrix $W^{[i]}$ to act only on site i.

It should be noted that the MPO tensor in equation 3.24 is a 5×5 matrix containing 2×2 operators. Thus, it corresponds to an MPO with auxiliary bond dimension 5 and physical bond dimension 2. Finally, it should be clear that a product of tensors $W^{[i]}$, one for each system site, generates the Hamiltonian in the form of 3.23.

This construction of the MPO works immediately for periodic or infinite boundary conditions. For finite boundary conditions, some extra work needs to be done at the edges of the system: the MPO tensors there need to be *vectors* rather than matrices. One way to do this is to bookend the 'chain' of matrices $W^{[i]}$ by vectors ensuring only sets of local operators starting in the R-state and ending in the F-state will be included in the MPO:[6]

$$\hat{H} = \begin{pmatrix} 0 & 0 & 0 & 0 & 1 \end{pmatrix} \cdot W^{[1]} W^{[2]} \cdots W^{[L]} \cdot \begin{pmatrix} 1 & 0 & 0 & 0 & 0 \end{pmatrix}^T \tag{3.25}$$

[6]Here the FSM is taken to traverse the system from right to left, as can be inferred from the leftmost vector having a 1 in the position corresponding to state F, and the rightmost vector having a 1 in the position corresponding to state R. For the FSM to move left-to-right, the $W^{[i]}$ in (3.24) would be transposed everywhere.

Equivalently, $W^{[1]}$ and $W^{[L]}$ can be replaced with, respectively, the transposed bottom-most (leftmost) row (column) of the $W^{[i]}$ in vector form:

$$\begin{aligned}\hat{H} = &\begin{pmatrix} h\hat{S}^z & \hat{S}^+ & \hat{S}^- & \hat{S}^z & \mathbb{1} \end{pmatrix} \cdot W^{[2]} W^{[3]} \cdots W^{[L-1]} \\ &\cdot \begin{pmatrix} \mathbb{1} & (J/2)\hat{S}^- & (J/2)\hat{S}^+ & J_z\hat{S}^z & h\hat{S}^z \end{pmatrix}^T,\end{aligned} \tag{3.26}$$

which we can also obtain by multiplying out the the first and last product in (3.25).

3.3.2 Long-range Hamiltonians

The FSM method for generating MPOs can also be used for longer-range interactions (Crosswhite, Doherty, and Vidal, 2008). This will typically induce operators deeper in the 'bulk' of the MPO matrix (compare (3.24), where all operators are on the 'edge' of the matrix). An example of this is shown here for the (next-nearest-neighbour) Hamiltonian

$$\hat{H} = J_1 \sum_i \hat{S}_i^z \hat{S}_{i+1}^z + J_2 \sum_i \hat{S}_i^z \hat{S}_{i+2}^z, \tag{3.27}$$

which corresponds to the FSM in figure 3.10b. This FSM generates the following matrix in the basis $(R, 1, 2, F)$:

$$W = \begin{array}{c} \\ R \\ 1 \\ 2 \\ F \end{array} \begin{array}{c} \begin{array}{cccc} R & 1 & 2 & F \end{array} \\ \begin{pmatrix} \mathbb{1} & 0 & 0 & 0 \\ J_1\hat{S}^z & 0 & \mathbb{1} & 0 \\ J_2\hat{S}^z & 0 & 0 & 0 \\ 0 & \hat{S}^z & 0 & \mathbb{1} \end{pmatrix} \end{array}, \tag{3.28}$$

which implies that this Hamiltonian has an MPO representation with bond dimension 4.

3.4 The Density Matrix Renormalization Group

3.4.1 Description of the method

DMRG (White, 1992; White, 1993; McCulloch, 2007; Schollwöck, 2011; Hauschild and Pollmann, 2018) is, at its core, a variational ground state algorithm. While originally developed without the use of MPS notation (White, 1992; White, 1993), we here consider the method only from the perspective of MPS, although a number of references consider the original form. The goal is to find the variational ground state of a given Hamiltonian, i.e., to minimize $\frac{\langle\psi|H|\psi\rangle}{\langle\psi|\psi\rangle}$. We can rewrite this as a differential equation and get rid of the denominator using a Lagrangian multiplier:

$$\begin{aligned}\frac{\mathrm{d}}{\mathrm{d}|\psi\rangle} \frac{\langle\psi|H|\psi\rangle}{\langle\psi|\psi\rangle} &= 0 \\ \Rightarrow \frac{\mathrm{d}}{\mathrm{d}|\psi\rangle} \left(\langle\psi|H|\psi\rangle - \lambda \langle\psi|\psi\rangle\right) &= 0.\end{aligned} \tag{3.29}$$

We now cast this expression into the graphical MPS picture (figure 3.11).

From here, we take the following steps. Firstly, while the derivative in (3.29) and figure 3.11 technically applies to every component of the state $|\psi\rangle$, we approximate the problem by considering the derivative only with respect to a single MPS tensor. This

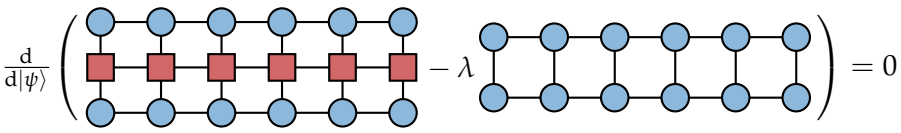

FIGURE 3.11: The variational problem (equation 3.29).

constitutes a linearising approximation to the global and highly non-linear problem. Secondly, the derivative $\partial/\partial A^*_{iab}$ (where A^*_{iab} is the (bra-state) MPS tensor at site i, with auxiliary bonds a and b) results in taking out this tensor from the diagram. We consider exemplarily that this particular tensor is the second tensor from the left in the bottom copy of the MPS to end up with the expression in figure 3.12.

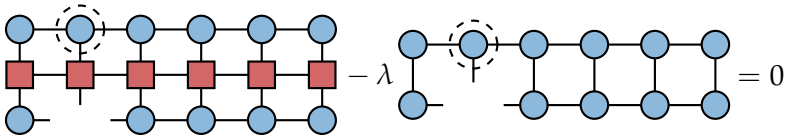

FIGURE 3.12: Evaluating the derivative in figure 3.11 removes a single MPS tensor from the network. The problem now is to solve this expression, where the variable is the circled tensor. This corresponds to solving a generalized eigenvalue problem $\tilde{H}\mathbf{v} - \lambda A\mathbf{v} = 0$, where $\tilde{H}$ and A are matrices. This equivalence becomes clearer in figure 3.13.

This changes the problem from a differential equation to a matter of finding the circled tensor so as to satisfy the equation in figure 3.12. The second term in the problem simplifies by using the canonical form of the MPS (figure 3.6b). This reduces the problem to an eigenvalue problem of the form $\tilde{H}\mathbf{v} - \lambda\mathbf{v} = 0$, where $\tilde{H}$ (denoted this way as it is the Hamiltonian in the local Schmidt basis) is a matrix with eigenvalue λ and corresponding eigenvector $\mathbf{v}$ (figure 3.13).

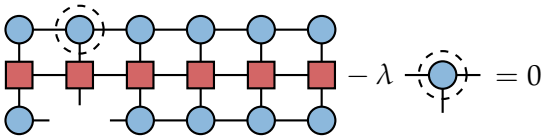

(A) The problem of figure 3.12 reduced by applying the canonical form of the MPS.

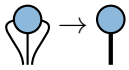

(B) Reshaping the MPS tensor into a vector.

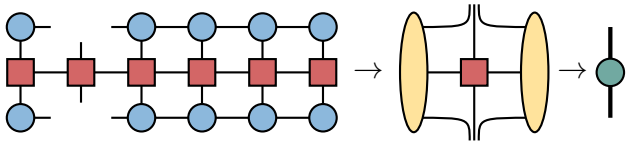

(C) Reshaping the DMRG network into a matrix. The intermediate step consists of contracting the left and right halves of the big network into single *environment* tensors. To save computation time, it is these environment tensors that are used for most DMRG steps, rather than the MPS and Matrix Product Operator themselves.

FIGURE 3.13: The expression from figure 3.12 simplifies into a regular eigenvalue problem $\tilde{H}\mathbf{v} - \lambda\mathbf{v} = 0$. The equivalence of subfigure 3.13a to an eigenvalue problem is illustrated by subfigures 3.13b and 3.13c.

The eigenvalue problem can now be solved using any suitable algorithm. The Lanczos algorithm (Lanczos, 1950) is one of the most commonly used algorithms, mainly due to it only requiring the implementation of a matrix-vector product. Additionally, the Lanczos algorithm is very fast for sparse matrices (which arise when utilising the conservation of quantum numbers as in section 3.2.6) and is optimised to calculate (multiple)

extremal eigenvalues and -vectors, which is ideal for ground state calculations. The solution to the eigenvalue problem gives us an eigenvector (which is then the 'best guess' for the MPS tensor) and an eigenvalue (which is the best guess for the ground state energy). The optimized tensor is placed back into both copies (A and A^*) of the MPS.

To get a global solution for the ground state problem, we repeat this procedure on all sites of the MPS by 'sweeping' through the system. By sweeping here, we mean optimising the tensor on all sites sequentially from left to right, then going back from right to left. This ensures the MPS remains in canonical form throughout the calculation. Sweeping is repeated until a convergence of both the ground state energy and the entanglement entropy (section 3.2.3) is reached.

The method described here is called *single-site update* DMRG, because only a single site is optimized at a time. This method is known to suffer from getting stuck in local minima. To resolve this issue, a *mixer* gets introduced to the algorithm (see section 3.4.2). Alternatively, a variant of the algorithm utilising a two-site update was historically developed first, and is more robust against getting stuck in local minima.. This is a completely equivalent algorithm, but instead of optimizing a single MPS site, two neighbouring tensors are first contracted together. The eigenvalue problem is then solved for this two-site tensor, after which it is split back into its single-site components using an SVD as in figure 3.5. One can also imagine combinations of one- and two-site updates (Takasaki, Hikihara, and Nishino, 1999).

3.4.2 Mixer

As mentioned above, the single-site DMRG algorithm can suffer from convergence issues. A bigger (related) issue, however, is that the single-site algorithm has no way of increasing the bond dimension of the MPS, which makes it impossible to obtain non-trivial results when initialising the algorithm with a product state (the most common way of starting DMRG). To overcome both these issues, the idea of a *mixer* was introduced (White, 2005; Hubig et al., 2015). The mixer works by slightly perturbing the MPS at each DMRG step. This allows the MPS bond dimension to increase and, if this was not present prior to the mixing step, potentially introduces an overlap of the MPS with the ground state.

The mixer is implemented through a so-called *subspace expansion* (due to Hubig et al. (2015); see Hauschild and Pollmann (2018) and the code referenced therein for details of the actual implementation as used for this thesis). For this expansion, the 'active' MPS tensor A_i is contracted with the left (or right, depending on the direction of the sweep) environment tensor and the Matrix Product Operator tensor W_i, after which the auxiliary bond between A_i and A_{i+1} is 'expanded' using this new object. See figure 3.14. This increases the bond dimension between A_i and A_{i+1}, allowing for the DMRG algorithm to converge.

Because the mixer perturbation is only beneficial if the MPS does not yet accurately represent a ground state to the MPO, the mixer is only used at the start of the DMRG simulation. The mixer is therefore typically controlled by three parameters, setting the initial strength of the perturbation, the 'decay rate' with which to decrease the mixer's influence with each DMRG sweep, and the maximum number of sweeps that will include a mixing step. This provides opportunities to fine-tune the algorithm to the problem being studied, as will again be pointed out in section 3.6.1.

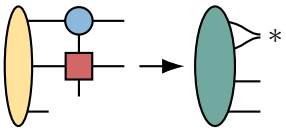

FIGURE 3.14: Contraction of the network for the mixer's subspace expansion. The yellow tensor is the left environment tensor, as shown in figure 3.13c. Note that the new tensor (green) has dimensions equal to the original MPS tensor (blue) for the bottom two legs, corresponding (bottom-to-top) to the left- and bottom leg of the MPS tensor, respectively. The new tensor is multiplied by a scalar (the *mixer amplitude*) and concatenated with the MPS tensor A_i along the new bond marked with an asterisk. The next MPS tensor A_{i+1} has the dimension of the corresponding bond extended to accommodate the expansion.

3.4.3 Infinite size DMRG

Infinite size DMRG (or iDMRG) is a variation of DMRG that is suitable for computations in the thermodynamic limit. While already included in the original formulation of DMRG (White, 1992), the method gained traction only when the mixer approach (see section 3.4.2) and a good initial guess for the Lanczos algorithm were described (Ueda, Nishino, and Kusakabe, 2008; McCulloch, 2008). iDMRG computes the ground state of a translationally invariant system in the limit $L \to \infty$. It does this by using 'regular' DMRG to optimise an MPS representing the repeating unit of the system (henceforth called the *MPS unit cell*) with respect to the Hamiltonian and some left- and right *environments*, then contracting the newly found MPS *into* the environments. See figure 3.15 for a graphical depiction of this approach. This process is repeated until enough MPS unit cells have been contracted into the environments that the 'true' edges of the system are a distance much bigger than the correlation length away from the 'active' unit cell $d_{\text{edge}} \gg \xi$. The 'active' unit cell can then be said to represent the ground state of the infinite system.

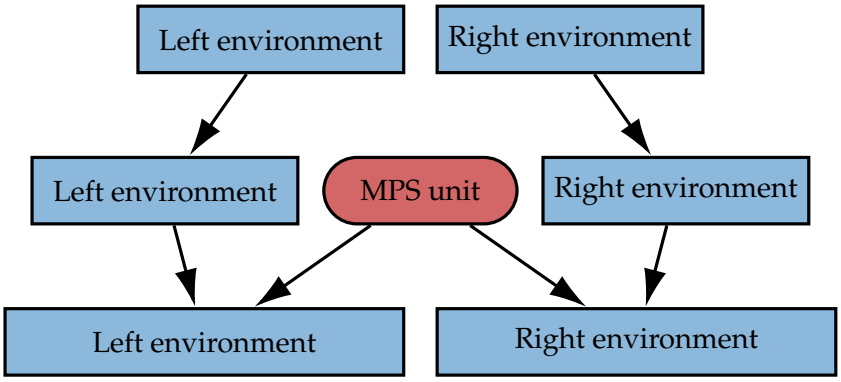

FIGURE 3.15: Graphical representation of iDMRG. The system, consisting of two environments (denoted blue), gets an MPS unit cell (denoted red) inserted in the centre. This unit cell gets optimised with respect to the Hamiltonian and the environments using finite-size DMRG. After optimisation, the unit cell is contracted into both environments, after which the cycle repeats. Note that the environments take the form of environment tensors as shown in the second step in figure 3.13c, which means the memory requirements of iDMRG are only minimally bigger than those of finite-size DMRG

3.4.4 DMRG for two-dimensional systems: snake ordering

There exist tensor network based approaches that are explicitly formulated to study two-dimensional systems, such as projected entangled pair states (PEPS, see Nishino and Okunishi, 1996; Verstraete and Cirac, 2004) and two-dimensional versions of tree tensor networks (Shi, Duan, and Vidal, 2006; Tagliacozzo, Evenbly, and Vidal, 2009; Murg et al., 2010) and MERA (Vidal, 2007; Evenbly and Vidal, 2009; Corboz and Vidal, 2009; Corboz et al., 2010). However, it is possible to use DMRG for pseudo-2D systems (Nishino, 1995; Verstraete and Cirac, 2004), which will be the method used in this thesis.

We start by defining the system on a 2D geometry where one of the dimensions is finite (and typically small), such as a cylinder or finite-width strip. We can then approximate a state of this system by a 'snake' MPS on the two-dimensional lattice (figure 3.16), which gives an effective 1D description of the 2D system. We can then apply the usual 1D DMRG to find the ground state of this system. The obvious downside to this is that the snake ordering introduces some artificial long-range interactions, which makes increasing the size of the system along one of the dimensions very expensive. An alternative way of thinking about this is the area law mentioned in section 3.2.3, which limits the effectiveness of *any* 2D tensor network method. Thus, this method is only suitable for computations with strips or cylinders, where the finite dimension is small.

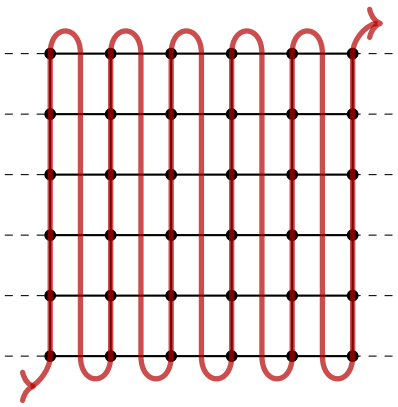

FIGURE 3.16: A 'snake' MPS looping through a two-dimensional system. Note that the system is infinite in the horizontal direction, but finite (with $L_y = 6$) in the vertical direction

3.5 A note on implementation

The code for this thesis was implemented in Python 2. Core methods and algorithms were developed by the collaboration behind Kjall et al. (2013). We have adapted the model code for the bosonic Harper-Hofstadter model (chapter 4) as used by Motruk et al. (2016) and Motruk and Pollmann (2017). We developed the fermionic model based on this code. All runtime and analysis scripts were developed by the author. For a more recent version of the code used, we refer the reader to TeNPy (Hauschild and Pollmann, 2018), an open-source Python 3 package for the simulation of strongly correlated quantum systems with tensor networks, which includes bosonic and fermionic Harper-Hofstadter model codes developed by the author of this thesis.

3.6 Protocol for using DMRG

While the above sections explain the theory of how DMRG works, and most packages (e.g., Hauschild and Pollmann, 2018) come with a guide on how to interact with the software,[7] there is often little guidance for how to approach a physics question using these methods. This section is an attempt to provide such guidance, describing a protocol on how to go from a model implementation in the MPO language, to an answered question.

Our basic workflow for a DMRG project is given here. Where necessary, individual steps will be expanded on below.

1. Confirm the correctness of the model implementation.
2. Run some low-effort tests to see whether the question seems answerable.
3. If the tests are successful, run production-quality simulations
4. Confirm that results are converged.

3.6.1 Confirming the model is correct

Although modern tools make model implementation much easier than constructing the MPO by hand, one should still ensure that the MPO represents the intended model faithfully. There are several possible ways to do this. Firstly, for sufficiently small system sizes, one can contract the entire MPO into a matrix, and inspect the matrix elements. These should reproduce the analytical Hamiltonian up to machine precision, or any other necessary cut-off (e.g., long-range interactions may be truncated at some finite distance). Secondly, if the model basis allows it, one can construct MPSs for known eigenstates of the model and evaluate whether these reproduce the correct eigenvalues upon contraction with the MPO. Finally, one can sometimes construct a basis of single- or even two-particle MPSs in some basis, and evaluate the MPO on this basis to get a representation of the single- and two-particle Hamiltonian. If the model contains only single- and two-body terms, this latter approach should reproduce all terms in the Hamiltonian.

3.6.2 Low-effort tests

As not every state can be accurately represented by an MPS, some results are outside the reach of DMRG. To prevent wasting considerable numerical resources on a fruitless project, it is recommended to run some low-effort trials first, and see whether any indication of the desired result can be found. If so, one can then go on to more computationally expensive simulations. If not, one should evaluate:

1. Whether there is a mistake in the model or simulation set-up,
2. Whether a slightly more computationally expensive test would potentially yield a result, or
3. Whether your approach is unfortunately out of reach of DMRG.

To set up low-effort trials, one should limit system size, bond dimension and the range of interactions, as well as (if possible) target a non-critical region of phase space. All these measures reduce the size of and/or entanglement entropy needing to be captured by the MPS, which yields both memory and run time advantages. Of course, one introduces a trade-off between computational cost and accuracy, which is why one should be careful to not put too much faith into results obtained at this stage.

[7] See the documentation at `https://tenpy.readthedocs.io/`.

3.6.3 Convergence

Ensuring that the results of a DMRG simulation are well-converged and thus reliable is a hugely important part of any DMRG study. Possible indications that there might be a convergence issue include:

1. The simulation shows a non-monotonous decrease of energy, and/or a non-monotonous increase of entanglement entropy. An increase of energy or decrease of entanglement entropy on subsequent steps within a sweep, or between subsequent sweeps, are particularly suspicious.

2. The simulation does not halt because it reached a convergence criterion, but because it reached its maximum number of sweeps.

3. Results vary wildly under small changes of parameters. In particular, if a small change in χ yields a big change in results, one should be suspicious of the data.

To combat convergence issues of the DMRG algorithm, several strategies (short of switching to a different method) can be attempted:

1. Ensure that there are no errors in the model (see section 3.6.1) or the simulation set-up.

2. Increase the maximum bond dimension.

3. Ramp up the maximum bond dimension during simulation, rather than starting at the highest value. I.e., define a schedule wherein the first N_{sweeps} run at some $\chi_1 < \chi_{\text{max}}$, the next N_{sweeps} at $\chi_1 < \chi_2 < \chi_{\text{max}}$, etc.

4. Increase the maximum number of sweeps the algorithm is allowed to make.

5. Change the mixer settings to in- or decrease the effects of the mixer.

6. Change convergence criteria. This will not overcome convergence issues in itself, but can help fine tune the DMRG simulation if it takes a long time to converge (relax the convergence constraints), or if the simulation finishes too soon (tighten the constraints).

7. Increase the minimum number of sweeps taken by the algorithm. Again, this will not resolve issues due to bad convergence, but might prevent bad results due to premature convergence.

8. Change the size and shape of the MPS unit cell (where possible), in case an artificially enforced translational invariance prevents the algorithm from finding a true ground state which is incommensurate with this periodicity. For example, a chain system which has a true ground state that is periodic in three sites, will not be accurately represented by a two-site MPS unit cell, as the latter enforces two-site periodicity.

In some instances, it is essentially unavoidable to encounter convergence issues. In particular, a simulation of a critical state can cause problems with DMRG convergence, as these states violate the area law underlying an accurate MPS approximation. In these cases, one should acknowledge the difficulties imposed by the method and take care to be very careful in interpreting the data.

3.7 Numerically resolving phase transitions

As the main results of this thesis (see chapter 6) revolve around the study of a phase transition using DMRG, we here give some background information on resolving phase transitions numerically. MPS have been used extensively to study phase transitions in a wide range of settings (Wolf et al., 2006; Cozzini, Ionicioiu, and Zanardi, 2007; Asoudeh, Karimipour, and Sadrolashrafi, 2007; Verstraete, Murg, and Cirac, 2008; Ueda and Maruyama, 2012; Pillay, 2020)

Naively, to identify a phase transition, one would look for divergences or discontinuities in observables such as the energy density, correlation length, and entanglement entropy. The MPS construction of our states allow us to read off several of these observables straightforwardly (Schollwöck, 2011; Hauschild and Pollmann, 2018). Observables indicating critical phenomena are of particular interest. The main study of critical phenomena in this thesis relies on a divergence of the correlation length, as well as the extraction of a *central charge c*, as will be outlined below. However, studying a phase transition using MPS is subject to some limitations native to the method, which we will describe first.

3.7.1 Limitations

There are two main limitations that restrict the efficacy of numerical methods in resolving phase transitions (in particular the order of said transition). Firstly, it is generally impossible to smoothly cover any parameter space numerically. Thus, we are forced to discretise the parameter space, which can lead to misidentification of a critical point, or even the absence of critical behaviour in the data, if the discretisation is too course.

The second challenge is that at finite numerical resources, methods such as DMRG are unable to capture infinite correlation lengths. A finite bond dimension will necessarily truncate the effective correlation length found in numerical studies, as an MPS description of a system with $\xi \to \infty$ would require $\chi \to \infty$.[8] This is problematic for two reasons. Firstly, if the correlation length at the critical point cannot grow indefinitely, it may be difficult to discern the critical point at all. Secondly, due to the truncation of the correlation length, numerical results may seem to evidence a first order phase transition, even though the physical transition may be second order. Both these problems can be mitigated to some extent by careful finite size scaling, as well as *finite entanglement scaling*.

We note here that, even when scaling analyses are performed carefully, some ambiguity about the order of a phase transition may remain. As noted, the truncation of ξ can make a second order transition appear as first order transitions. Conversely, it is conceivable that a system which shows a monotonous increase of ξ with χ for all numerically attainable χ might level off at higher, unfeasible χ.

3.7.2 Finite size and finite entanglement scaling

Finite size scaling is most useful for numerical methods that are not able to perform in the thermodynamic limit, but can provide calculations for a range of system sizes. These results can then be extrapolated to obtain an estimate of the behaviour at infinite system size. In our numerics, we are able to simulate cylinders of infinite length. However, entanglement constraints severely limit the cylinder circumferences we can accurately represent. In chapter 5, we use some finite size scaling to study the topological entanglement entropy associated with a bisected cylinder. The range of cylinder circumferences

[8] This problem is specific to the MPS approach. Other tensor network approaches, such as TTN or MERA (section 3.2.7) *are* able to represent infinite ξ with finite numerical resources.

there ranges from 4 to 10 lattice sites, although we introduce a rescaling of this dimension to obtain more distinct data points. In chapter 6, most results are restricted to $6 \leq L_y \leq 8$, which is the reason we do not use finite size scaling for the analyses in that chapter.

Finite entanglement scaling (Tagliacozzo et al., 2008; Pollmann et al., 2009) is a technique unique to methods like MPS, where the correlation length is constrained by a finite bond dimension. By obtaining results for various bond dimensions χ, and potentially extrapolating these to $\chi \to \infty$, one can obtain an estimate of the physics in the absence of this constraint. In this thesis, we will use finite entanglement scaling to investigate the phase transitions in chapter 6. We do not use the scaling approach to obtain any specific values in the thermodynamic limit. Rather, we study the behaviour of the system (particularly the increase of the correlation length ξ and entanglement entropy S_E) with increasing bond dimension. This has two reasons. Firstly, as ξ and S_E are expected to diverge at a critical point, it makes little sense to attempt to obtain a finite value. However, a monotonous increase of these observables with χ is taken as evidence for such a divergence. Secondly, studying the simultaneous scaling of S_E and ξ allows us to estimate the central charge associated with a conformal field theory describing the system at its critical point. This is further explained in section 3.7.3.

3.7.3 Obtaining the central charge

« What is a central charge? » A central charge is a property of a conformal field theory (CFT), which measures the number of degrees of freedom in the system (Francesco, Mathieu, and Sénéchal, 1997). We obtain the central charge from the scaling behaviour of $S_E(\chi)$ and $\xi(\chi)$, which are expected to relate by $S_E \sim c/6 \log \xi$ at the critical point (Calabrese and Cardy, 2009). We therefore perform a finite entanglement scaling procedure, obtaining S_E and ξ for various χ, and compare a straight line to the results, obtaining an estimate for c in $S_E(\chi) \sim c/6 \log \xi(\chi)$. While the finite entanglement scaling procedure was originally developed for 1D systems (Tagliacozzo et al., 2008; Pollmann et al., 2009), it has recently been applied successfully to 2D systems as well (Geraedts et al., 2016; Gohlke et al., 2017).

A heuristic picture of why this technique works in 2D is that on the cylinder near the critical point, the correlation length is much larger than the circumference $\xi \gg L_y$ (for sufficiently large χ and increasing with χ). For increasing ξ (driven by an increasing χ), degrees of freedom further and further away from the cut in the cylinder will become entangled. At large ξ, the cylinder therefore looks effectively one-dimensional and is described by the same critical scaling as a 1D system. In terms of CFT, this statement is equivalent to stating that the CFT limit of our 2+1D system near the critical point is given by a 1+1D theory. For more formal CFT studies of the scaling of the entanglement entropy on a cylinder geometry, see for example Chen et al. (2017) and Zhu et al. (2018).

Chapter 4

The Harper-Hofstadter model

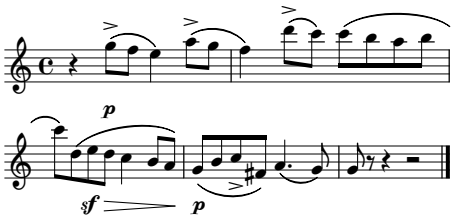

Felix Mendelssohn, *Symphony no. 4 in A major, Op. 90*

4.1 The Harper-Hofstadter model

The Harper-Hofstadter model (Fig. 4.1), sometimes referred to as Azbel-Harper-Hofstadter model (Harper, 1955; Azbel, 1964; Hofstadter, 1976) describes particles confined to a two dimensional lattice, subject to a magnetic field. It is given by a Hamiltonian[1]

$$\hat{H}_{\text{Hof}} = -t \sum_{\langle ij \rangle} \left[e^{i\phi_{ij}} \hat{a}_i^\dagger \hat{a}_j + \text{H.c.} \right] + V \sum_{\langle ij \rangle} :\hat{n}_i \hat{n}_j:, \tag{4.1}$$

where t is the hopping amplitude, $\hat{a}^\dagger(\hat{a})$ a creation (annihilation) operator[2], V is the interaction strength between particles and $\hat{n}_i = \hat{a}_i^\dagger \hat{a}_i$ are number operators. $\langle ij \rangle$ denotes nearest-neighbour pairs of sites (in the fermionic case) or on-site interactions (in the bosonic case), hence $:\hat{n}_i \hat{n}_j:$ denotes normal-ordered interaction term. The parameter ϕ is obtained through *Peierls substitution*. It enters here as a complex-valued hopping phase which models a magnetic field perpendicular to the 2D plane, i.e., an Aharonov-Bohm phase.

To describe the Aharonov-Bohm phase, we use a gauge expression $\phi_{ij} = \int_j^i \mathbf{A} \cdot \mathrm{d}\mathbf{l}$, where we typically use the Landau gauge $\mathbf{A} = xB\hat{\mathbf{y}}$. Here, the field strength is given by $B = n_\phi \Phi_0$, with $\Phi_0 = \frac{2\pi\hbar}{e}$ the magnetic flux quantum and n_ϕ the number of flux quanta per lattice plaquette ('flux density'). We consider the lattice to be tiled by magnetic unit cells. The magnetic unit cell is the minimum set of lattice plaquettes enclosing an integer number of flux quanta.[3] In the Landau gauge with $n_\phi = p/q$, the magnetic unit cells have dimensions $q \times 1$.

[1] Note that technically, the Harper-Hofstadter Hamiltonian is a single-particle Hamiltonian consisting only of the first sum in (4.1). The interaction term, however, is crucial to the work in this thesis, and is thus added here for clarity.

[2] This operator can be bosonic or fermionic, with slightly different consequences. We will touch on this later in this chapter.

[3] We will occasionally denote this as "an integer multiple of 2π flux".

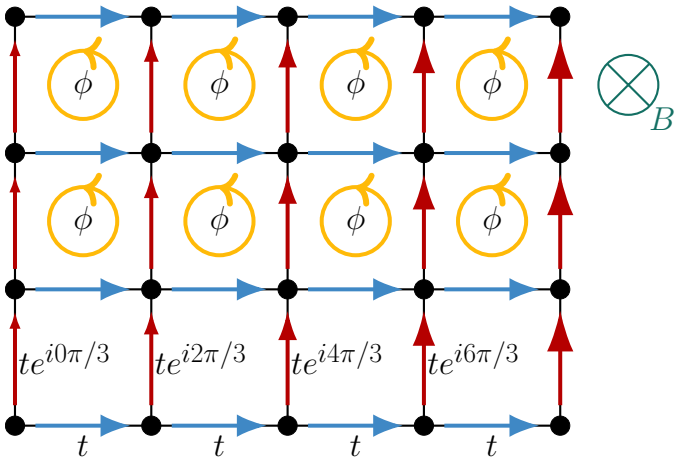

FIGURE 4.1: Schematic depiction of the Harper-Hofstadter model (4.1). In the Landau gauge, there is no phase associated with hopping processes along horizontal bonds, but particles pick up a position-dependent phase when hopping along a vertical bond. The resulting phase picked up when hopping in a closed loop simulates the Aharonov-Bohm phase picked up in a homogeneous magnetic field B.

Due to the presence of a magnetic field, there are two relevant length scales for the model, the lattice constant a (which we will set to $a = 1$ everywhere), and the magnetic length $\ell_B = \sqrt{\hbar/eB}$. The demonstration of the importance of ℓ_B will be an important part of chapter 5.

The Harper-Hofstadter model exhibits several interesting properties. One of these properties is its fractal band structure, known as the 'Hofstadter Butterfly' due to Hofstadter (1976). The band structure of the Harper-Hofstadter model will be studied in section 4.2. Another property, which is the reason for our interest in the model, is that it exhibits both the integer quantum Hall effect (Thouless et al., 1982) as well as the fractional quantum Hall effect (FQHE) (Kol and Read, 1993; Sørensen, Demler, and Lukin, 2005; Palmer and Jaksch, 2006; Möller and Cooper, 2009; Möller and Cooper, 2015). Finally, the model has recently been experimentally realized (Aidelsburger et al., 2013; Miyake et al., 2013; Aidelsburger et al., 2014), giving an added impulse to its study.

4.2 The Hofstadter butterfly

In the following, we largely follow the derivation in Hofstadter (1976). Given (4.1), the Landau gauge and setting $V = 0$ for now, we can write the time-independent single particle Schrödinger equation $H\psi(x,y) = E\psi(x,y)$ in the following form:

$$\psi(x+1,y) + \psi(x-1,y) + e^{i2\pi Bx}\psi(x,y+1) + e^{-i2\pi Bx}\psi(x,y-1) = E\psi(x,y), \tag{4.2}$$

where the action of the Hamiltonian comes in the form of a translation of the wave function combined with the Aharonov-Bohm phase. We have set[4] $e = h = c = 1$.

Note that (4.2) as written only holds in the Landau gauge $\mathbf{A} = Bx\hat{\mathbf{y}}$, which results in the Hamiltonian only depending on x: $\hat{H} = \hat{H}(x)$. In this case, k_y is a 'good' momentum (i.e., its operator commutes with the Hamiltonian), and we have

$$\psi(x, y \pm 1) = e^{\pm ik_y}\psi(x,y). \tag{4.3}$$

[4]Note, e here is the charge quantum, not the natural exponent.

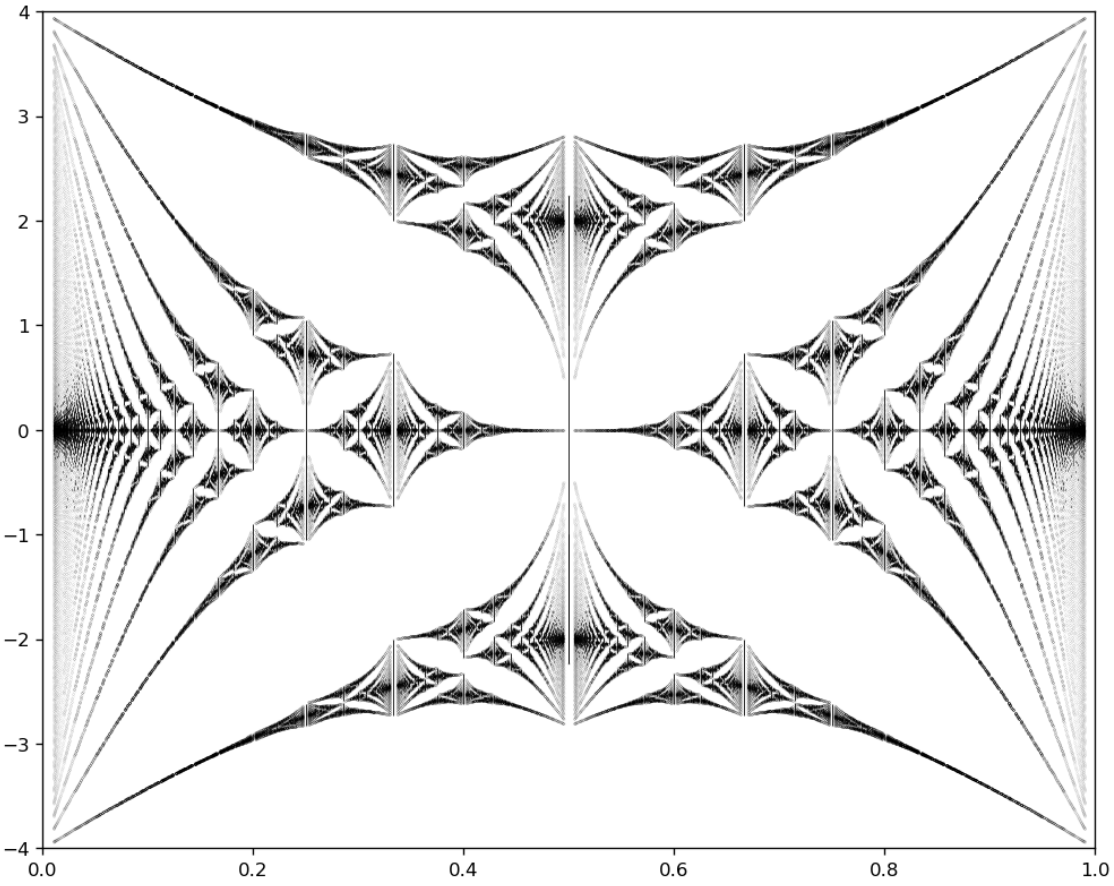

FIGURE 4.2: The Hofstadter butterfly. The vertical axis is energy, the horizontal axis is flux density n_ϕ. Note that at rational flux densities $n_\phi = p/q$, the spectrum consists of q bands, p of which lie below the main (bottom-left to top-right) diagonal. Clear example cases are $n_\phi = 1/3$ (three bands, of which one below the main diagonal) and $n_\phi = 2/5$ (five bands, of which two below the main diagonal). Note that in some cases (e.g., $n_\phi = 1/2$ or $n_\phi = 1/4$), two bands can touch, making it seem like they are indistinct.

We know from symmetry arguments that the eigenstates are plane waves along $\hat{y}$ modulated by some function $g(x)$:

$$\psi(x, y) = e^{i\nu y} g(x). \tag{4.4}$$

This turns the Schrödinger equation (4.2) into a one-dimensional difference equation, named the Harper equation after Harper (1955):

$$g(x+1) + g(x-1) + 2\cos(2\pi x p/q - \nu) g(x) = E g(x). \tag{4.5}$$

Note that we have postulated a rational flux density, $n_\phi = p/q$; this ansatz can however be derived from the physical constraints imposed on equation (4.5). The Harper equation can be rewritten in matrix form:

$$\begin{pmatrix} g(x+1) \\ g(x) \end{pmatrix} = \underbrace{\begin{pmatrix} \epsilon - 2\cos(2\pi x p/q - \nu) & -1 \\ 1 & 0 \end{pmatrix}}_{A(x)} \begin{pmatrix} g(x) \\ g(x-1) \end{pmatrix}, \tag{4.6}$$

where the matrix is now labelled $A(x)$. The Harper equation has a solution when, for the matrix $Q(\epsilon, \nu) = \prod_{x=1}^{q} A(x)$, we have $|\operatorname{Tr} Q(\epsilon, \nu)| \leq 2$. Plotting all the solutions for $0 \leq n_\phi \leq 1$ leads to the spectrum known as the Hofstadter butterfly, seen in figure 4.2.

The derivation of the Hofstadter butterfly described above is equivalent to utilising the fact that the entries in the non-interacting Hamiltonian (4.1 with $V = 0$) repeat after q lattice sites for a rational flux density $n_\phi = p/q$. This lets us state $\psi(x+q, y) = \exp[ik_x q]\psi(x, y)$. We can diagonalise (4.1) exactly in the basis of these states and find the minimum and maximum value for each band by collating solutions for a range of lattice momenta k_x and k_y.

4.2.1 Properties of the Hofstadter Butterfly

We now move on to studying the spectrum shown in figure 4.2 in more detail. A very prominent feature of the butterfly is its self-similarity, which was first described by Hofstadter (1976). If we consider the largest-scale structure to be the 'main butterfly', we can identify parts of the figure as being distorted reproductions of this main structure. Our interest lies mainly in the lower left tail of the butterfly. The repetitions of the main butterfly in this tail (or indeed any repetition of the main butterfly) are called 'subcells' (see figure 4.3). Hofstadter (1976) defines a mapping from the variables n_ϕ and E onto "local variables" describing each subset, thereby proving the self-similarity of the butterfly.

Our main motivation for studying the lower left tail of the Hofstadter butterfly (Fig. 4.3) is that this tail exhibits the behaviour of a lowest Landau level (LLL). This can be seen by considering the adiabatic connection from the 'continuum limit' $p/q \to 0$, where the Landau level description becomes exact (Qi, 2011; Scaffidi and Möller, 2012; Roy, 2014; Andrews and Möller, 2018). For a general rational flux density $n_\phi = p/q$, the full spectrum consists of q bands[5] (also called sub-bands or mini-bands in this context), p of which make up the LLL tail. The LLL-like behaviour is assumed to hold even when the tail is made up out of several (magnetic) bands. For example, at $n_\phi = 3/11$, the spectrum contains 11 bands, 3 of which are in the LLL tail. As we will see in chapters 5 and 6, a state mirroring a LLL fractional quantum Hall (FQH) state exists on a hybridization of these 3 lowest bands.

4.3 Quantum Hall states in the Hofstadter model

To see the connection between the Harper-Hofstadter model and the quantum Hall effect (QHE), we look back to section 2.6, where we discussed quantum Hall (QH) states on a lattice in the absence of a magnetic field. We now repeat this discussion with the inclusion of a magnetic field, considering a square lattice with lattice constant $a = 1$. In cases of a rational flux density ($\Phi = (p/q)\Phi_0$), we can define a generalisation of the Brillouin zone called the *magnetic Brillouin zone*:

$$-\frac{\pi}{q} < k_x < \frac{\pi}{q}, \quad -\pi < k_y < \pi, \tag{4.7}$$

where the difference between k_x and k_y stems from the use of single-particle states in the Landau gauge: these satisfy $\psi(x+q, y) = \exp[ik_x q]\psi(x, y)$, reducing the Brillouin zone for k_x to the interval $[-\pi/q, \pi/q]$. With periodic boundary conditions, this again forms a torus $\mathbb{T}^2$. Coincidentally, this provides a basis for the statement that the Hofstadter butterfly splits into q bands: on an $L_x \times L_y$ sample, each of these magnetic Brillouin zones supports $L_x L_y/q$ states.

[5] Note that occasionally, these bands touch (e.g., at $n_\phi = 1/2$), making it difficult to distinguish them.

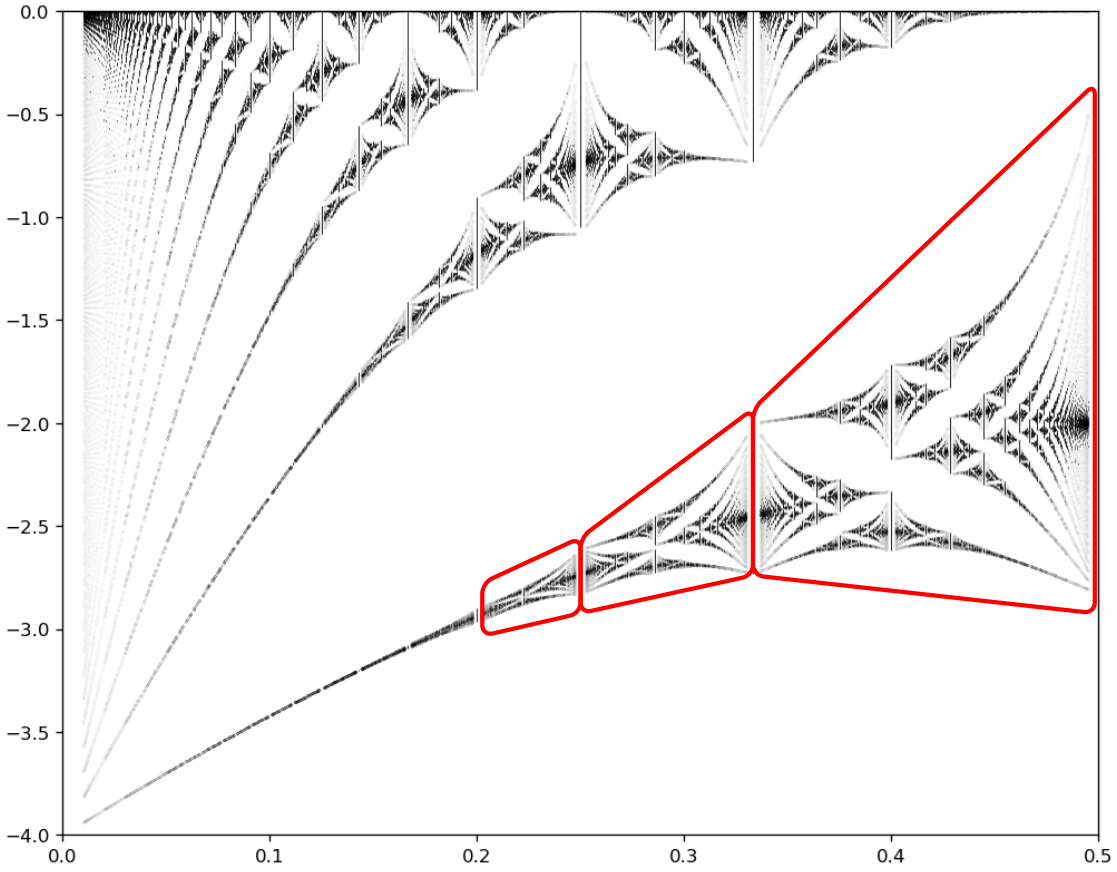

FIGURE 4.3: The lower-left quadrant of figure 4.2, showing the LLL tail of the Hofstadter butterfly. The first three subcells (enumerated right-to-left) have been marked in red.

4.3.1 Chern numbers

Starting from the magnetic Brillouin zone, one can associate a Chern number with each of the Harper-Hofstadter model's gaps and bands by a procedure similar to, but more involved than the reasoning in section 2.6 (Fradkin, 2013). A crucial role in the derivation is played by the Diophantine equation (Thouless et al., 1982)

$$r = s_r q + t_r p, \tag{4.8}$$

where r labels the gap, $p/q = n_\phi$ is the flux density as before, and $s_r, t_r \in \mathbb{Z}$. With the constraint $|t_r| < q/2$, this equation has a unique solution (t_r, s_r). The *TKNN invariant* t_r is the Chern number associated to the gap.

To associate a Chern number with each band rather than with the gaps, one just needs to compute the difference between subsequent gaps:

$$C_r = t_r - t_{r-1}, \tag{4.9}$$

where we use $t_0 = 0$ by definition, and C_r is the Chern number of the r^{th} band. A filled Harper-Hofstadter (sub-) band now has a Hall conductivity $\sigma_H \propto C_r$. For n filled bands, we obtain

$$\sigma_H = \sum_n C_n = t_n. \tag{4.10}$$

The Diophantine equation (4.8) can be rewritten in terms of the density of states n_s[6] and flux density n_ϕ, yielding an equation (Wannier, 1978)

$$n_s = t_r n_\phi + D. \tag{4.11}$$

In this expression, every gap in the Hofstadter butterfly is represented by a straight line, the slope of which corresponds to the Chern number associated with that gap. The entire Hofstadter spectrum can thus be coloured in as a phase diagram for the integer quantum Hall effect (Osadchy and Avron, 2001). This construction allows us to easily compute Chern numbers in the Harper-Hofstadter spectrum, which we will then compare to numerical results in chapters 5 and 6.

4.3.2 Flux insertion

To study QH states in the Hofstadter model, we use Laughlin's flux insertion technique (Laughlin, 1981) (see section 2.4) to obtain the Hall conductivity of a state on the cylinder. Insertion of flux threading the cylinder (figure 4.4, bottom) is achieved by adding an extra phase factor $e^{i\phi_{\text{ext}}}$ to hopping processes across the 'boundary' of the cylinder.[7] This phase factor acts like another Aharonov-Bohm phase (similar to the phase factor in 4.1). By pseudo-adiabatically increasing ϕ_{ext} from 0 to $m \times \Phi_0$ in increments $\Delta\phi_{\text{ext}}$ and recomputing the ground state at each step, we can obtain the Hall conductivity from the Matrix Product State (MPS) via the Berry phase obtained from the entanglement spectrum. A full description of this method is given in Zaletel, Mong, and Pollmann (2014).

The Berry phase (compare equation 2.39) arising from an insertion of ϕ_{ext} flux is

$$\gamma = \int_0^{\phi_{\text{ext}}} \mathrm{d}\phi \mathcal{A}(\phi) - i \log \langle \psi_0^{(0)} | \psi_0^{(\phi_{\text{ext}})} \rangle \,, \tag{4.12}$$

where $\psi_0^{(0)}$ ($\psi_0^{(\psi_{\text{ext}})}$) is the ground state at the start (end) of the flux insertion, respectively, and $\mathcal{A}(\phi)$ is the Berry connection given by

$$\mathcal{A}(\phi) = -i \langle \psi_0^{(\phi)} | \frac{\partial}{\partial \phi} | \psi_0^{(\phi)} \rangle \,. \tag{4.13}$$

With the flux implemented through the boundary conditions as described above, the Berry phase can be expressed in terms of the Schmidt coefficients as

$$e^{i\gamma} = \exp\left[2\pi i \sum_i \lambda_i^2 Q_i \right]. \tag{4.14}$$

Here, Q_i is the charge of the i-th Schmidt state $|\chi_i^L\rangle$.

This finally allows us to read off the Hall conductivity from the entanglement spectrum via

$$\sigma_{xy} = \frac{e^2}{2\pi\hbar} \int_0^{\phi_{\text{ext}}} \mathrm{d}\phi \frac{\partial}{\partial \phi} \gamma(\phi) = \frac{e^2}{\hbar} \gamma(\phi)\big|_0^{\phi_{\text{ext}}} . \tag{4.15}$$

[6] More precisely, this is the density of states *per unit area*. For a filled band, n_s is equal to the particle density.

[7] We here mean hopping processes from sites on the cylinder labelled $(x, y) = (x, L_y)$ to $(x, y) = (x, 0)$ and vice versa. There is no physical significance to this particular 'bond'. This can be regarded as a gauge freedom, as only $\oint \mathbf{A} \cdot \mathrm{d}\mathbf{l}$ is a measurable quantity.

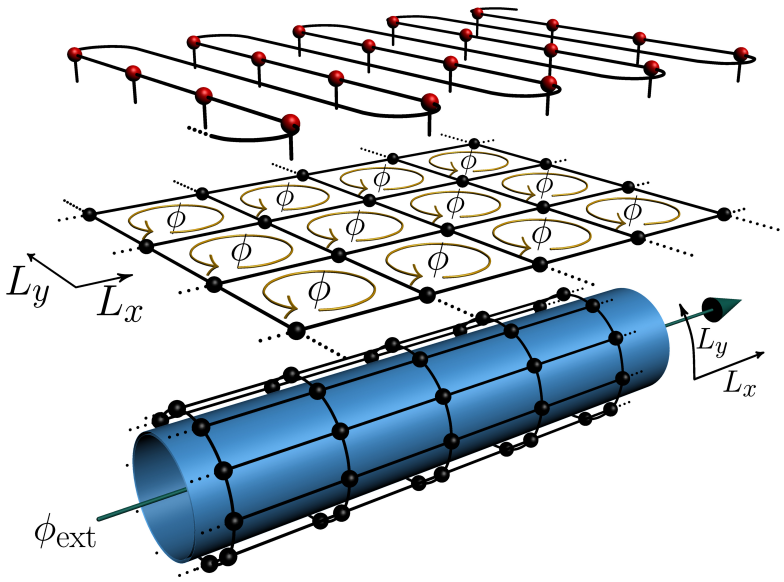

FIGURE 4.4: The Harper-Hofstadter model (centre) is modelled on a cylinder (bottom). States are represented by an MPS (top). For flux insertion (section 4.3.2), external flux ϕ_{ext} is threaded through the cylinder.

4.3.3 Fractional Chern insulator or fractional quantum Hall effect?

We here want to emphasise the distinction between two different manifestations of FQH states in the Harper-Hofstadter model. Much of this thesis will be concerned with states supported on the LLL 'tail' (see section 4.2.1), even where this tail consists of several sub-bands. As we have stated before, there exists an adiabatic connection between states on the LLL tail and states in the continuum LLL. Thus, these FQH states form some continuation on the lattice of well-known continuum states. In contrast, there exist fractional Chern insulator (FCI) states supported on only a subset of the sub-bands forming the LLL tail. We will call these states 'true' FCI states, as for these there exists no adiabatic connection to the continuum. In more general terms, the distinction between true FCI states and lattice FQH states can be cast as a distinction between fractional states on partially filled bands with $|C| > 1$ and $|C| = 1$, respectively.

There are additional arguments to be made for whether or not states supported on Harper-Hofstadter sub-bands should be labelled FCI or FQH states. In this thesis, we take an agnostic position with regard to these arguments, and will occasionally use both terms interchangeably. An overview of these arguments can be found in Andrews and Möller (2018). The interplay between lattice FQH states and true FCI states has seen some recent attention (Möller and Cooper, 2009; Möller and Cooper, 2015; Lee et al., 2018) and motivates in part our work in chapter 6.

4.4 MPO construction for the Hofstadter model

To investigate the Hofstadter model using the Density Matrix Renormalization Group (DMRG) (White, 1992; Schollwöck, 2011), we need to define the Hamiltonian as a Matrix Product Operator (MPO).[8] As MPOs are essentially one-dimensional, this starts by defining a 'snake-like' ordering of the square lattice. The ordering is shown in figure 4.5. We

[8] For a much more comprehensive introduction to MPOs and DMRG, we refer the reader back to chapter 3.

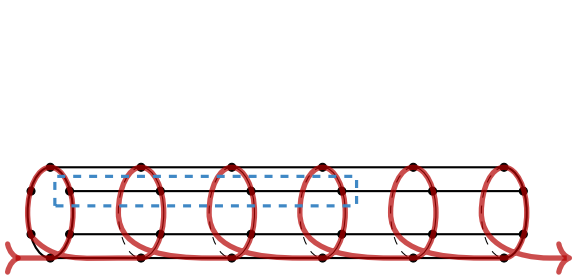

(A) The square lattice on a cylinder. The direction along the cylinder should be thought of as infinite (i.e. the cylinder continues infinitely on both sides).

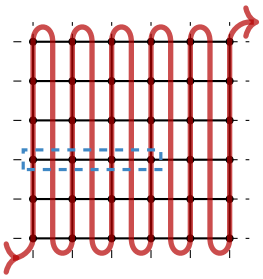

(B) The 'unwrapped' cylinder: a square lattice. Boundary conditions are infinite in the horizontal direction and periodic in the vertical direction. Note that this image is fully equivalent to figure 4.5a, and the 'direction' of the snake is always upwards on MPS sites.

FIGURE 4.5: A 'snakelike' MPS or MPO on a square lattice, for the cylinder and plane geometries. The snake is depicted by the red loop through the lattices. The magnetic unit cell (here consisting of 4 sites, corresponding to $n_\phi = \frac{1}{4}$) is depicted using a blue dashed rectangle.

use the cylinder geometry, as this is widely used in prior works (see for example Zaletel, Mong, and Pollmann (2013), Motruk et al. (2016), Gerster et al. (2017), and Lee et al. (2018)), due in part to the cylinder geometry being well-suited for the types of problems we investigate (Hu et al., 2012).

For the fermionic instance of the model, an important addition to the Finite State Machines (FSMs) shown is the inclusion of the Jordan-Wigner transformation (effecting a mapping from fermionic operators to spin operators):

$$\begin{aligned} n_j &\leftrightarrow \frac{1}{2}(\sigma_j^z + 1) \\ a_j &\leftrightarrow \exp[i\pi \sum_{l<j} n_l]\sigma_j^- \\ a_j^\dagger &\leftrightarrow \exp[i\pi \sum_{l<j} n_l]\sigma_j^+, \end{aligned} \tag{4.16}$$

where $\sigma_j^{x,y,z}$ are the Pauli matrices and $\sigma_j^\pm = (\sigma_j^x \pm \sigma_j^y)/2$. This transformation effectively results in placing "Jordan-Wigner strings" of σ_j operators on all sites between creation- and annihilation operators in the MPS/MPO ordering.[9]

Figure 4.5 also shows a magnetic unit cell for $n_\phi = \frac{1}{4}$, which in the Landau gauge from the previous section gives a 4×1 magnetic unit cell. We denote the size of the MPS unit cell as an $L_x \times L_y$ tiling of magnetic unit cells. Thus, given a flux density $n_\phi = \frac{1}{m}$, the MPS unit cell contains a total of $m \times L_x \times L_y$ sites. Different gauges, like the commonly used symmetric gauge $\mathbf{A} = \frac{B}{2}\left(-x\hat{\mathbf{y}} + y\hat{\mathbf{x}}\right)$, lead to differently shaped magnetic unit cells. In such a case, we still maintain the $L_x \times L_y$ tiling of magnetic unit cells to create the MPS unit cell. All numerical results in this thesis have been obtained in the Landau gauge.

Given the snake-like ordering of figure 4.5, we can define the MPO by using an FSM description of the Hamiltonian (Crosswhite and Bacon, 2008). FSMs for the first two sites of a ring in a cylinder of circumference 3 are shown in figure 4.6.

[9] When considering only nearest-neighbour hopping terms, this only affects 'horizontal' hopping, i.e., those terms that do not fall along the snake ordering of the MPO.

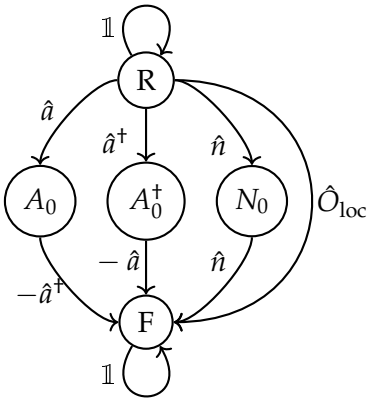

(A) First site on a ring. Processes like $R \to A_0$ signal the 'start' of a new interaction, and processes like $A_0 \to F$ 'complete' interactions from the previous site (in case of vertical interactions) or ring (in case of horizontal interactions).

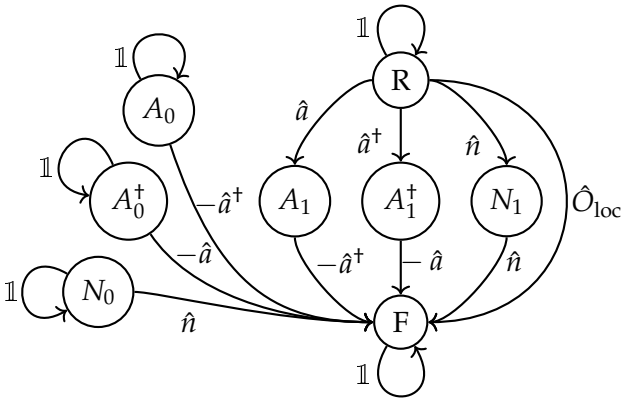

(B) Second site on a ring. Here, processes like $A_0 \to F$ signal vertical interactions being 'completed'. Processes like $R \to A_1$ signal the 'start' of a new interaction, and processes like $A_1 \to F$ 'complete' interactions from the previous ring. The 'self-interactions' for the sites with subscript 0 give rise to the intermediate operators for longer-range interactions. It is worth noting that the third side on the ring (not shown here) would add another set of 'self-interacting' states with subscript 1.

FIGURE 4.6: Finite State Machines for the Hofstadter model. The Finite State Machine is different for each site on a ring; here, we show the first two sites only. $\hat{O}_{\text{loc}}$ denotes single-site terms. On every site, the Finite State Machine contains all states $\{ R, A_i, A_i^\dagger, N_i, F \mid i \in \{ 1, 2, 3 \} \}$. Nearest-neighbour terms are created in two ways. For 'vertical' terms (i.e., differing along $\hat{\mathbf{y}}$, also termed being on the same 'ring'), an operator is placed on one site (e.g., $\hat{a}$ on site 0 in (a), which puts the FSM in state A_0), and the interaction is 'completed' on the next site [the process $A_0 \to F$ in (b)]. For 'horizontal' interactions (along $\hat{\mathbf{x}}$ or between different rings), an operator is similarly placed on one site, but is now followed by a 'string operator' on all following sites [e.g., the processes $A_0 \to A_0$ in (b)]. When the FSM reaches the same y on the next ring, the interaction is completed [by the processes $A_0 \to F$ and similar in (a)]. States not shown in these graphs are disconnected from the rest of the Finite State Machine, existing only as a process $X \to X$ mediated by an identity. Note that for the fermionic model, any operator connecting an A- or $A^\dagger$-state to itself is a Jordan-Wigner string operator rather than an identity. The FSMs shown here implicitly assume the model is bosonic (with nearest-neighbour $\hat{n}_i \hat{n}_j$ terms).

One of the consequences of the snake-like ordering of the MPS and MPO is that horizontal nearest-neighbour interactions on the lattice are turned into long-range interactions (with an interaction length equal to the circumference of the cylinder) in the MPO. This prohibits us from scaling up the circumference indefinitely, as the bond dimension of the MPO has to increase to include these interactions, while the bond dimension of the MPS has to increase to capture long-range correlations.

An additional limitation for two-dimensional systems is that the entanglement entropy in the system obeys an area law (Hastings, 2007; Eisert, Cramer, and Plenio, 2010), as was already discussed in sections 3.2.3 and 3.4.4. Thus, while gapped local one-dimensional systems can be accurately simulated with finite bond dimension for any size system, for two-dimensional systems, the required bond dimension to accurately approximate the physical state eventually tends to infinity. In our case, this corresponds to the entanglement entropy of a cut through the cylinder scaling linearly with the circumference of the cylinder, which will be crucial for the results in section 5.1.2.

Chapter 5

Existence and stability of fractional states in the lowest Hofstadter tail

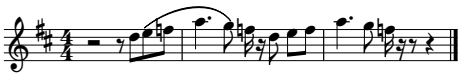

Francis Poulenc, *Gloria*

In this chapter,[1] we will study the existence and stability of a fractional quantum Hall (FQH) state in the lowest tail of the Hofstadter butterfly (see section 4.2). In many works on lattice quantum Hall effects (QHEs), it is assumed implicitly or explicitly that there is a single lowest Landau level (LLL)-like band (in the case of the Harper-Hofstadter model, this band is a single band in the LLL tail) which supports a Laughlin-like FQH state.[2] Less commonly, presumably because these cases are studied less often, whenever the LLL tail of the Harper-Hofstadter model contains several sub-bands, i.e., at flux densities $n_\phi = p/q$ with $p > 1$, it is assumed that the LLL approach is nevertheless still valid, and an FQH state supported by several sub-bands can be found. However, this assumption is rarely, if ever, confirmed explicitly. Therefore, we here investigate whether, and under what conditions, a multiple sub-band LLL supports an FQH state.

As part of this investigation, we develop a new way of extrapolating the topological entanglement entropy from finite-size scaling results (which are expected to obey an area law) for the entanglement entropy. This is a common way of diagnosing topological states. However, due to the increased computational complexity of simulations on larger system sizes, few system sizes are computationally accessible, limiting the number of potential data points. Our approach (section 5.1.2) overcomes this by collating results for various flux densities n_ϕ, which in turn affects the magnetic length ℓ_B. We thereby obtain a much denser spread of data points for systems of limited size in terms of the lattice constant, thus improving the accuracy of the extrapolation at limited numerical cost.

In light of the work presented in chapter 6, the emphasis in this chapter will be on the fermionic Harper-Hofstadter model. The existence of $\nu = 1/3$ Laughlin states in this model (on multiple sub-bands) will be investigated in section 5.1. For completeness, in section 5.2 we demonstrate that our methods are equally applicable to the bosonic model, by studying $\nu = 1/2$ Laughlin states in this model. In section 5.3, we move beyond the

[1] Part of the content of this chapter has appeared previously in Schoonderwoerd, Pollmann, and Möller (2019).

[2] While it is hard to give references for a claim like this, and such a list of references is necessarily non-exhaustive, some notable works investigating FQH or fractional Chern insulator (FCI) states on a single band include Sørensen, Demler, and Lukin (2005), Neupert et al. (2011), Regnault and Bernevig (2011), Bergholtz and Liu (2013), Parameswaran, Roy, and Sondhi (2013), Gerster et al. (2017), and Rosson et al. (2019). This should in no way be regarded as a criticism of those works.

Laughlin states, and apply our methods to demonstrate the existence of the next state in the FQH hierarchy, at $\nu = 2/5$.

5.1 Evidence for $\nu = 1/3$ Laughlin states in multiple sub-band LLLs

We know from chapter 2 that interactions stabilise FQH states. The Chern insulator (CI) insulator states in the Haldane[3] (see for example Grushin et al. (2015)) or Harper-Hofstadter models are understood to be special cases of this (section 2.6). Therefore, we should expect to need a finite $V > 0$ for fractional states to occur in the Harper-Hofstadter model. In our numerical work, we set $V = 10t$ unless otherwise mentioned.

The results in Grushin et al. (2015) exclusively consider situations where the FCI is supported by a single, fractionally filled band. In such cases, the ground state at low V is metallic. In this chapter, we will not make a distinction between the low-V states in the single-sub-band LLL case compared to the multiple-sub-band case. Rather, we will study the existence and stability of fractional states in both of these cases. However, in chapter 6, the low-V states of some multiple-sub-band cases will be studied in more detail.

In this chapter and the next, all results have been obtained by the Density Matrix Renormalization Group (DMRG) simulations (see chapter 3), using the Matrix Product Operator implementation of the Harper-Hofstadter model as in section 4.4, except where otherwise noted. To simulate the Harper-Hofstadter model at a filling fraction ν and a flux density $n_\phi = p/q$, we need a particle density $n = \nu n_\phi$. The Matrix Product State (MPS) formalism only supports an integer number of particles in the MPS unit cell. Thus, where necessary, we increase L_x (i.e., the number of magnetic unit cells tiled along the cylinder) until the MPS unit cell is commensurate with an integer number of particles at the correct filling fraction. For example, to obtain a $\nu = 1/3$ LLL filling fraction at $n_\phi = 1/7$ and $L_y = 7$ requires $n = 1/21$, and thus $L_x = 3$: this gives a total number of lattice sites $N_{\text{sites}} = qL_xL_y = 7 \times 7 \times 3 = 147$, which can satisfy $n = \nu n_\phi = 1/21$ with $N_{\text{particles}} = 7$.[4] Setting $L_x < 3$ would not allow an integer number of particles in this case. In all of the following, we have set L_x to the minimum value that allows an integer particle number.

In figure 5.1, the results of a flux insertion procedure (see sections 2.4 and 4.3.2) are shown for a range of flux densities $n_\phi = p/q$ with $p > 1$. To obtain these results, the MPS ground state is first calculated using DMRG with $\phi_{\text{ext}} = 0$. The resulting state then gets used as the initial state for a DMRG run at $\phi_{\text{ext}} = \delta\phi$, which yields a new state. The new state is then used as initial guess at $\phi_{\text{ext}} = 2\delta\phi$, and so forth. Thus, provided that $\delta\phi$ is chosen small enough, and χ large enough, this procedure constitutes the semi-adiabatic insertion of flux, without requiring (lossy) time-evolution methods. At each step in this process, the expectation value of the charge (or *charge polarisation*) $\langle q_L \rangle$ to the left of a cut in the cylinder is calculated from the MPS. While the exact value of $\langle q_L \rangle$ carries no physical meaning, a change in $\langle q_L \rangle$ indicates the transport of charge in response to flux insertion.

For figure 5.1, a total of $3 \times 2\pi$ flux (i.e., 3 quanta) is threaded through the cylinder this way, and charge transported across a bisection of the cylinder is measured. We observe that, although the details of the transport vary for for different n_ϕ, all lines converge at the start (which is trivial since all results are normalised to start at $\langle q_L \rangle = 0$) and end of

[3] The Haldane model is similar to the Harper-Hofstadter model, differing in the lattice geometry and the fact that bands carry only Chern numbers $|C| = 0, 1$.

[4] Note that $N_{\text{sites}} = qL_xL_y$ due to the Landau gauge, as explained in section 4.4. An alternative calculation which yields the same result is to realise that $\nu = N_{\text{particles}}/N_{\text{MUC}} = 7/(3 \times 7)$.

the insertion procedure. The total charge transported upon insertion of 3 flux quanta is 1 in every case, consistent with a Hall conductivity of $\sigma_H = 1/3$ which is predicted by a Laughlin state ansatz. While this data cannot tell us if the state *is* a Laughlin state, we have clear evidence for a fractional state in all cases studied. In the following section, we will review additional evidence for the existence of an FQH state.

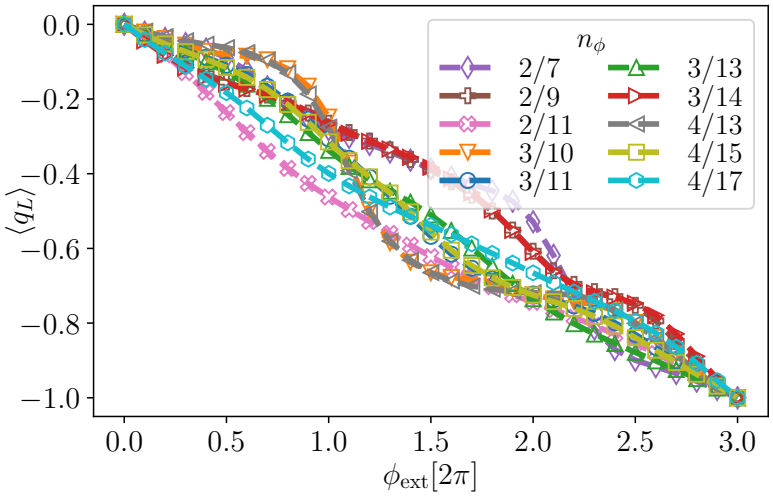

FIGURE 5.1: Flux insertion for various flux densities n_ϕ. In all cases, $L_y = 6$, $V = 10$, $\chi = 600$. Data has been normalised to start at $\langle q_L \rangle = 0$ for every n_ϕ. While the details of the transport are different for different n_ϕ, in all cases the total transport over the insertion of $3 \times 2\pi$ flux is the same and is consistent with $\sigma_H = 1/3$.

5.1.1 Momentum-resolved entanglement spectra

More evidence for the existence of FQH states at various flux densities is shown in figure 5.2. The entanglement spectrum $\{-\log \lambda_i(k_y)\}$ is given by the spectrum of the Schmidt decomposition of that state into two half-infinite states (Pollmann and Turner, 2012)

$$|\psi\rangle = \sum_{i,k_y} \lambda_i(k_y) \, |\chi^L_{i,k_y}\rangle \otimes |\chi^R_{i,k_y}\rangle \, . \tag{5.1}$$

The momentum-dependence of the Schmidt eigenstates can be extracted from eigenvalues of translations around the cylinder:

$$\hat{T}_y(a) \, |\chi^R_i\rangle = e^{-i2\pi k_y / L_y} \, |\chi^R_i\rangle \, , \tag{5.2}$$

such that a cylinder with a bigger circumference L_y also lets us obtain a finer resolution of momenta. In practice, the momentum-resolved entanglement spectrum is extracted from (the dominant eigenvector of) the transfer matrix formed by the overlap of an MPS with its conjugate, whereby the latter is translated according to (5.2).

Entanglement spectra have been hailed as a method to extract more information from the entanglement properties of a state than is available by looking only at the entanglement entropy (Li and Haldane, 2008). For quantum Hall (QH) states in particular, the entanglement spectrum is of interest as it lets us study the edge excitations of the system through a bulk observable (Regnault, 2017). Specifically, and of particular importance to future analyses in this thesis, the entanglement spectrum has been shown to have the

same level counting as the energy spectrum of edge excitations of a QH state, which we showed in section 2.2.3 (Ardonne and Regnault, 2011; Hermanns et al., 2011).

Here we show momentum-resolved entanglement spectra for cylinders with circumference $L_y = 8$. We observe that all cases (with $1 \leq p \leq 4$) show the two main indicators of an FQH state: a chiral 'tail' separated from the bulk by a so-called *entanglement gap*, as well as the partition counting associated with the edge excitations of a QH state. For comparison, figure 5.3 shows the spectrum of the model at $n_\phi = 1/9$ on a cylinder with $L_y = 12$. This latter figure shows the chiral tail more clearly than figure 5.2, but due to its large circumference is computationally expensive to produce. An extensive collection of additional momentum-resolved entanglement spectra can be found online in Schoonderwoerd (2020).

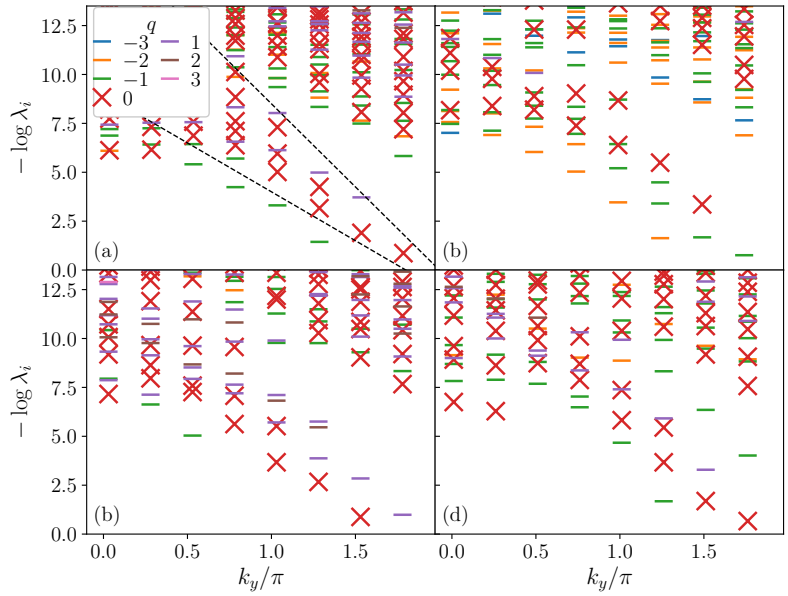

FIGURE 5.2: Momentum-resolved entanglement spectra for $L_y = 8$, $\chi = 600$. Different colours denote different quantum number sectors (with the $q = 0$ sector additionally denoted with crosses). All spectra have been shifted along k_y so that the 'chiral tail' is most clearly visible. Momenta and quantum numbers carry physical meaning only in a relative sense. (a) $n_\phi = 1/3$, (b) $n_\phi = 2/7$, (c) $n_\phi = 3/11$, (d) $n_\phi = 4/17$. At $n_\phi = 2/7$ (b), the spectrum is comparable to that at different n_ϕ under a shift in quantum number sectors, which demonstrates that only relative values of q have physical significance.

Two final pieces of evidence for the existence of a Laughlin state are shown in figures 5.4 and 5.5. In figure 5.4, we show the density-density correlation functions $\langle{:}\hat{n}_{0,y}\hat{n}_{x,y}{:}\rangle$ (where ${:}\hat{n}_{0,y}\hat{n}_{x,y}{:}$ denotes normal ordering of the fermionic operators) on an $L_y = 10$ cylinder at $n_\phi = 3/11$. The correlation functions reveal a strong correlation hole at small x, followed by a slight overshoot and rapidly damped oscillations at intermediate x. At larger values of x, an asymptotic value representative of a homogeneous fluid is reached. We observe that the correlation functions are independent of the position along the circumference of the cylinder, and that thus the state is translationally invariant along $\hat{\mathbf{y}}$. This picture is consistent with the Laughlin state, which describes a liquid with no long range order, but with strong short-range correlations maximizing typical inter-particle distances.

To demonstrate what effect the introduction of edges has on the system, we calculate the density profile for a strip geometry, where the strip is defined by infinite boundary

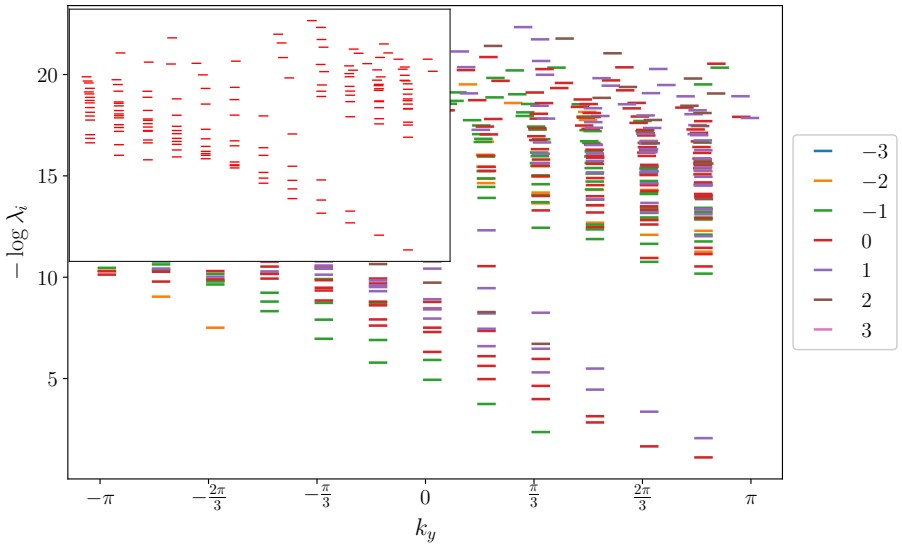

FIGURE 5.3: Momentum-resolved entanglement spectrum for the fermionic Harper-Hofstadter model at $n_\phi = 1/9$, on an $L_y = 12$ infinite cylinder. $V = 10$, $\chi = 600$. Different (charge) quantum number sectors have been marked with different colours. The spectrum has been rotated in k_y to most clearly show the 'chiral tail' of the spectrum, as only relative momenta have physical relevance. Inset: the spectrum for just the $q = 0$ sector, showing clearly the expected partition level counting $(1, 1, 2, 3, 5, 7, \dots)$.

conditions along $\hat{\mathbf{x}}$, but open boundary conditions (as opposed to the periodic boundary conditions describing a cylinder) along $\hat{\mathbf{y}}$. The results are shown in figure 5.5. This density profile shows translational invariance along the cylinder ($\hat{\mathbf{x}}$), as well as oscillations around the expected bulk value and overshoot near the edge. For a cylinder geometry (periodic boundary conditions in $\hat{\mathbf{x}}$), the density is homogeneous throughout. These results are consistent with the presence of a Laughlin state, taking into account the finite size effects seen at this relatively small value of L_y.

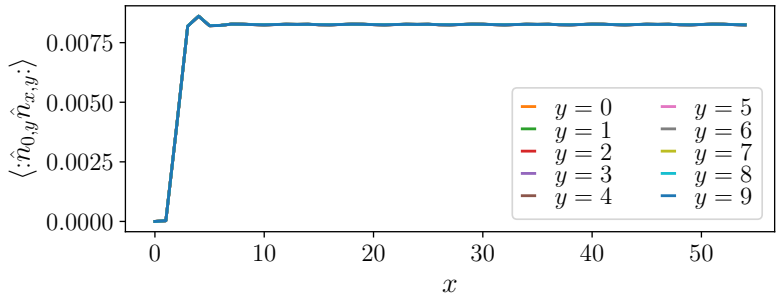

FIGURE 5.4: Real-space density-density correlation functions $\langle{:}\hat{n}_{0,y}\hat{n}_{x,y}{:}\rangle$ on an $L_y = 10$ cylinder at $n_\phi = 3/11$, $\chi = 500$.

5.1.2 Topological entanglement entropy

As was mentioned in sections 3.2.3 and 4.4, the entanglement entropy of the system under study tends to follow an area law. Thus, the entanglement entropy associated to a bisection of the Harper-Hofstadter cylinder is expected to scale linearly with the cylinder

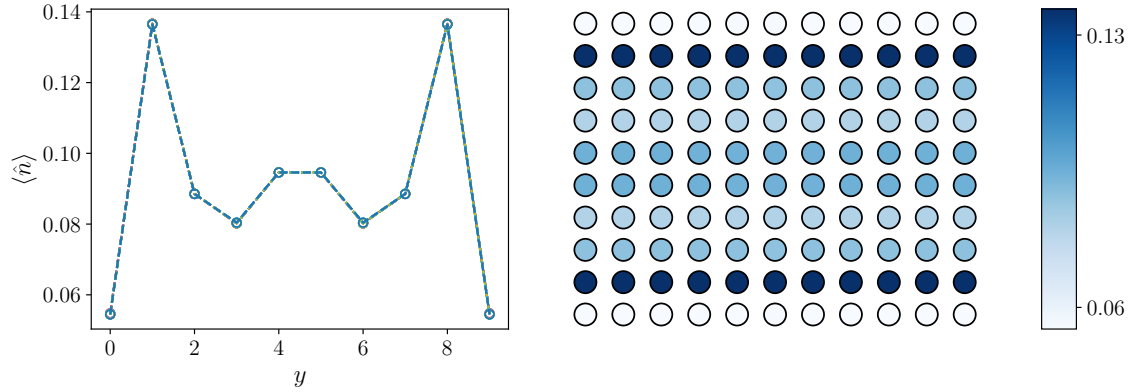

FIGURE 5.5: Density profile of an 11×10 site MPS unit cell in the $\nu = 1/3$ Laughlin state at $n_\phi = 3/11$. The plot on the left shows the density cross-section for all 11 'columns'. The figure on the right shows the on-site density for the entire unit cell. Data is obtained on a strip, rather than a cylinder (i.e., open instead of periodic boundary conditions along $\hat{y}$) to observe the effect of the edges. With periodic boundary conditions along $\hat{\mathbf{y}}$ (i.e., on the cylinder geometry), the density profile is homogeneous along $\hat{\mathbf{y}}$ (not shown).

circumference. For topologically non-trivial states, the area law scaling is expected to have an offset:

$$S_E = \alpha L_y - \gamma, \tag{5.3}$$

with γ also known as *topological entanglement entropy*, $\gamma = -S_{\text{topo}}$ (Kitaev and Preskill, 2006).

The offset γ is given by

$$\gamma = \log \mathcal{D}, \tag{5.4}$$

where

$$\mathcal{D} = \sqrt{\sum_a d_a^2} \tag{5.5}$$

is called the *total quantum dimension* of the system, and the d_a is the *quantum dimension* of particle a in the topological quantum field theory describing the system. For an Abelian theory (such as that describing Laughlin states), $d_a = 1$ for all particles in the theory. For a theory describing a Laughlin state at $\nu = 1/m$ there are m such particles, which gives us $\mathcal{D} = \log \sqrt{m}$. For the $\nu = 1/3$ Laughlin state specifically, this predicts $S_{\text{topo}} = -\ln \sqrt{3} \approx -0.549$ (Haque, Zozulya, and Schoutens, 2007; Läuchli, Bergholtz, and Haque, 2010; Zaletel, Mong, and Pollmann, 2013)

In figures 5.6 and 5.7, we show the scaling of entanglement entropy with cylinder circumference. Unlike previous (i)DMRG simulations of the Harper-Hofstadter model, we combine data for a range of flux densities n_ϕ, motivated by the computational advantages this brings in the torus geometry (Bauer, Jackson, and Roy, 2016; Andrews and Möller, 2018).

The combination of many different n_ϕ provides a significant technical improvement on earlier works: it allows us to obtain many more data points while maintaining a minimal circumference, thus reducing computational costs. Crucially, we find that when the cylinder circumference is expressed in units of ℓ_B, all data points collapse onto a single line, demonstrating that ℓ_B sets the relevant length scale for the density of entanglement

carried by the state. This technique has recently been employed on the honeycomb lattice (Andrews and Soluyanov, 2020) and has also been extended to take statistical and numerical errors into account (Andrews, Mohan, and Neupert, 2020).

Figure 5.6 shows the extrapolation of S_{topo} for flux densities $n_\phi = 1/q$. We observe a small-l_y deviation from linear scaling, visible as a 'flattening off' of the data for cylinders with $L_y < 1\ell_B$. This is likely due to finite-size effects. Figure 5.6 therefore shows two linear fits to the data, one where all data is taken into account, and a second where only data for $L_y > 1\ell_B$ is used. The latter fit provides an estimated $S_{\text{topo}} \approx -0.527$.

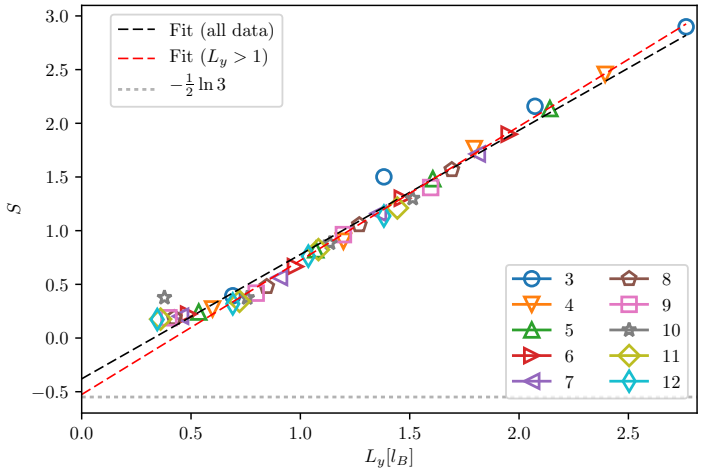

FIGURE 5.6: Entanglement entropy for the fermionic $\nu = 1/3$ Laughlin state as function of L_y (in units of ℓ_B), for several flux densities $n_\phi = 1/q$, q as shown in the legend. $V = 10$, $\chi = 500$ for all data. Also shown are two linear fits (dashed lines), one made by including all data, the second excludes data for $L_y < 1$. The extrapolated (at $L_y = 0$) value for the $L_y > 1$ fit is interpreted as the topological entanglement entropy (5.3). With the fit on $L_y > 1$, we find $S_{\text{topo}} \approx -0.527$, while the theoretical prediction (dotted horizontal line) is $S_{\text{topo}} = -\frac{1}{2}\ln 3 \approx 0.549$. The fit on all data gives $S_{\text{topo}} \approx -0.380$.

Figure 5.7 shows the extrapolation of S_{topo} for flux densities $n_\phi = p/q$. with $p > q$. In this case, no finite-size effects are observed, as $L_y[\ell_B] > 4$ everywhere. Some data have been removed prior to making this plot. We have excluded an outlier for the case of $p/q = 2/7, L_y = 5$, because its density profile differed significantly from that of a Laughlin state. We have also excluded results for the highest flux density studied, $p/q \geq 3/10$ as prior theoretical and numerical results suggest the Laughlin state is destabilized for $n_\phi \gtrsim 0.4$ (Hafezi et al., 2007). A linear fit on the data gives an estimate of $S_{\text{topo}} \approx -0.551 \pm 0.015$, which is in excellent agreement with the theoretical prediction. The uncertainty on this number is the standard deviation σ, which is computed from the variance σ^2 on the intersect value, yielded by the fit algorithm.

Combined with the results for flux insertion, momentum-resolved entanglement spectra and density-density correlation functions from section 5.1, these extrapolations provide strong evidence of the existence of a $\nu = 1/3$ Laughlin state in the LLL tail of the Hofstadter model, in both single-sub-band as well as multiple-sub-band cases.

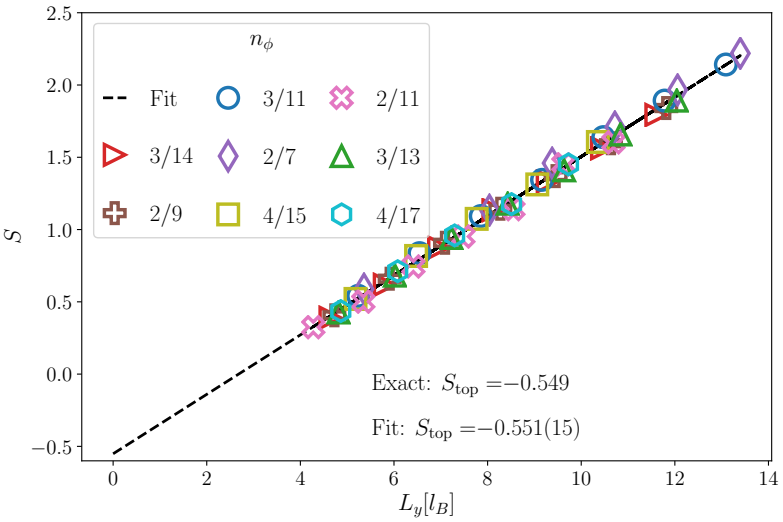

FIGURE 5.7: Entanglement entropy for the fermionic $\nu = 1/3$ Laughlin state as function of L_y (in units of ℓ_B, for several flux densities $n_\phi = p/q$ and circumferences $4 \leq L_y \leq 10$ (in units of the lattice constant). $\chi = 600$ for all data. Also shown is a linear fit (dashed line) to all data. The extrapolated (at $L_y = 0$) value for the fit is interpreted as the topological entanglement entropy (5.3). We find $S_{\text{topo}} \approx -0.551(15)$, while the theoretical prediction is $S_{\text{topo}} = -\frac{1}{2}\ln 3 \approx -0.549$).

5.2 Bosonic FQH states

As stated above, our main model of interest in this thesis is the fermionic Harper-Hofstadter model. However, a remarkable property of FQH physics is that bosons and fermions and fermions exhibit similar behaviour, with the only difference being the filling fractions ν at which QH states appear. For completeness therefore, we here show that the methods used above can also be applied to the bosonic model. We specifically investigate the $\nu = 1/2$ Laughlin state. To stabilise this state in the bosonic system, we limit the maximum occupation of any lattice site to 1, which corresponds to an infinite on-site repulsive interaction.

Figure 5.8 shows a selection of momentum-resolved entanglement spectra for the bosonic Laughlin state, all at $L_y = 10$, at various n_ϕ (i.e., a varying number of sub-bands in the LLL tail). All cases clearly show chiral modes with the expected level counting. More spectra are again available online in Schoonderwoerd (2020).

Figure 5.9 shows the extrapolation of the topological entanglement entropy. The extrapolated value (excluding the clear outlier at $n_\phi = 1/3$) $S_{\text{topo}} \approx -0.3459 \pm 0.0258$ is in excellent agreement with the theoretical prediction (5.4), which is $-\log\sqrt{2} = -0.3466$ in this case.

Figure 5.10 shows the results of flux insertion for the bosonic model for a broad selection of n_ϕ and L_y. Only results with $L_y > 7$ are shown, to keep the figure's legend to a manageable size. Only results where $\Delta\langle q_L\rangle = -1 \pm 0.01$ are shown, i.e., results where the charge transport was not quantised consistently with a $\nu = 1/2$ state are not included. The only results that are excluded in this latter way were obtained at $n_\phi = 1/3$, which is the largest flux density used and also yields anomalous results in figure 5.9. This could thus be due to the loss of stability of the Laughlin state at large n_ϕ we mentioned above, perhaps in combination with the modest bond dimension used here ($\chi = 500$). Nonetheless, it should be clear that our methods perform excellently for identifying the

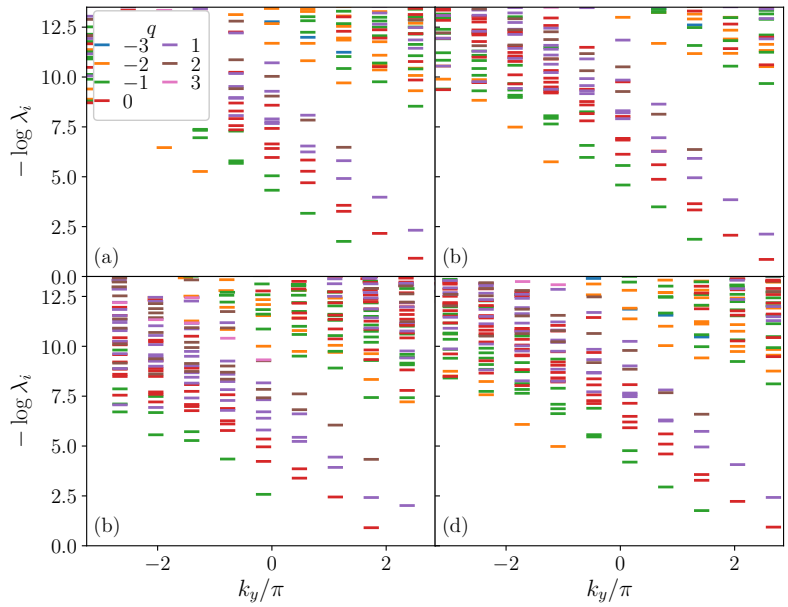

FIGURE 5.8: Momentum-resolved entanglement spectra for bosonic $\nu = 1/2$ Laughlin states, on cylinders with $L_y = 10$, for various flux densities n_ϕ. Included are (a) $n_\phi = 1/4$, (b) $n_\phi = 2/9$, (d) $n_\phi = 3/10$, (c) $n_\phi = 4/15$.

$\nu = 1/2$ Laughlin state in the bosonic Harper-Hofstadter model at various n_ϕ and L_y and moderate χ.

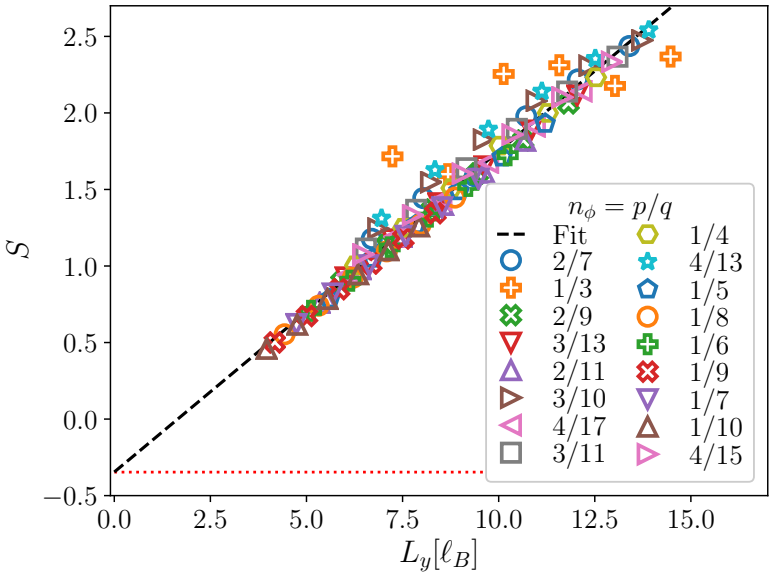

FIGURE 5.9: Extrapolation of the topological entanglement entropy S_{topo} for $\nu = 1/2$ Laughlin states in the bosonic Harper-Hofstadter model. For the extrapolation, the (clear outlier) $n_\phi = 1/3$ case has been excluded. The fit gives an extrapolation $S_{\text{topo}} \approx -0.3459 \pm 0.0258$, compared to the exact result (dotted red line) $-\log\sqrt{2} = -0.3466$.

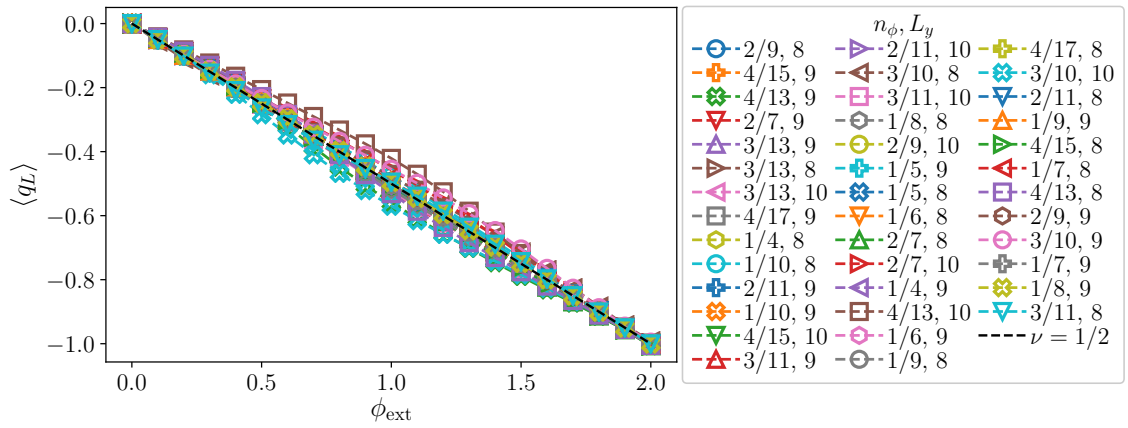

FIGURE 5.10: Flux insertion results for the $\nu = 1/2$ Laughlin state in the bosonic Harper-Hofstadter model. In all cases, $\chi = 500$ and the number of bosons per site is limited to 1, effecting infinite on-site repulsion. Data has been normalised to start at $\langle q_L \rangle = 0$ for every case. The dashed black line denotes a response of $\sigma_H = 1/2$, which is the expected behaviour for a $\nu = 1/2$ state. While the details of the transport are different for different L_y and n_ϕ, the total transport over the insertion of $2 \times 2\pi$ flux is quantised to $\Delta\langle q_L \rangle = 1$ for all cases shown. This figure shows only those cases with $L_y > 7$, where a quantised response (up to an absolute tolerance of $\Delta\langle q_L \rangle \pm 0.01$) consistent with a $\nu = 1/2$ state was found. Out of all the cases studied, only some results at $n_\phi = 1/3$ (the largest n_ϕ studied) did not yield this quantised response.

5.3 Evidence for a $\nu = 2/5$ state

We now extend the analysis above to the next state in the hierarchy (section 2.3.2), which has $\nu = 2/5$. After the appearance of Schoonderwoerd, Pollmann, and Möller (2019), similar work has been done by Andrews, Mohan, and Neupert (2020), who additionally studied the $\nu = 3/7$ state. We here report only on the flux insertion, entanglement spectrum, and topological entanglement entropy for the $\nu = 2/5$ state.

5.3.1 Flux insertion

Figure 5.11 shows the results of a flux insertion procedure (inserting $5 \times 2\pi$ external flux) for a range of n_ϕ and L_y. All cases shown demonstrate a response to the flux insertion consistent with a $\nu = 2/5$ state. I.e., all cases exhibit a transport of $\Delta\langle q_L \rangle = 2$ charge quanta, yielding a Hall conductivity $\sigma_H = 2/5$. As before, this provides a first piece of evidence for the existence of a $\nu = 2/5$ state, both in cases where $n_\phi = 1/q$ (i.e., a single sub-band forming the LLL Harper-Hofstadter tail) as well as in cases where $n_\phi = p/q$, $p > 1$ (i.e., where the LLL Harper-Hofstadter tail consists of multiple sub-bands).

It should be noted that figure 5.11 shows only those results that, up to a tolerance $\Delta\langle q_L \rangle \pm 0.01$, are consistent with a $\nu = 2/5$ state. However, flux insertions were performed for the entire range $5 \leq L_y \leq 9$ (plus $L_y = 10$ for multiple-sub-band cases), with single-sub-band flux densities $n_\phi = 1/q$, $3 \leq 10$ and a selection of multiple-sub-band flux densities $n_\phi = p/q < 1/3$, $2 \leq p \leq 4$.[5]

[5]For the cases with multiple sub-bands, only flux densities p/q where p and q are co-prime were considered. The full list of flux densities with $p > 1$ is $p/q \in \{2/7, 2/9, 2/11, 3/10, 3/11, 3/13, 4/15, 4/17\}$.

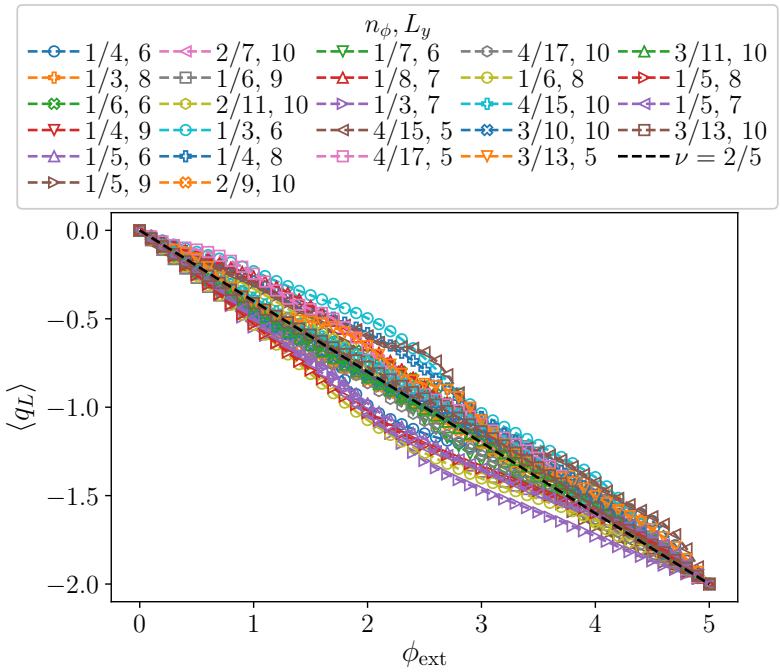

FIGURE 5.11: Flux insertion results for a $\nu = 2/5$ state at various flux densities n_ϕ and circumferences L_y. In all cases, $V = 10$, $\chi = 400$. Data has been normalised to start at $\langle q_L \rangle = 0$ for every case. The dashed black line denotes a response of $\sigma_H = 2/5$, which is the expected behaviour for a $\nu = 2/5$ state. While the details of the transport are different for different L_y and n_ϕ, the total transport over the insertion of $5 \times 2\pi$ flux is quantised to $\Delta\langle q_L \rangle = 2$ for all cases shown. It should be noted that this figure shows only those results where a quantised response (up to an absolute tolerance of $\Delta\langle q_L \rangle \pm 0.01$) consistent with a $\nu = 2/5$ state was found. As shown in figure 5.12, there are many cases for which the response was either not quantised, or not consistent with a $\nu = 2/5$ state. This is presumably due to the relatively small bond dimension used, combined with finite-size effects, as demonstrated in figure 5.15(b).

The total charge transport under flux insertion for all these cases is shown in figure 5.12(a) as function of the flux density n_ϕ, and in figure 5.12(b) as function of the circumference L_y in units of the magnetic length ℓ_B. We can clearly observe that many cases deviate from the expected behaviour of a $\nu = 2/5$ state. We also see clearly that quantisation is more precise at higher $L_y[\ell_B]$, indicating that finite-size effects may be in play at smaller circumferences.

Crucially, we see that most of the strongest deviations from $\sigma_H = 2/5$ occur at $L_y = 5$, potentially indicating an influence from finite-size effects. Additionally, convergence issues are likely to occur due to the relatively small bond dimension $\chi = 400$ used to obtain these results. However, due to the size of the MPS unit cell and the number of DMRG runs required for flux insertion simulations for these cases, an increase in bond dimension causes a large increase in computational cost and runtime. We therefore leave the refinement of these result to future studies.

5.3.2 Entanglement spectra

Here, we investigate the entanglement spectra of the candidate $\nu = 2/5$ states. For comparison, we look at the results for $n_\phi = 1/7$, $L_y = 10$, $V = 10$, which was studied at

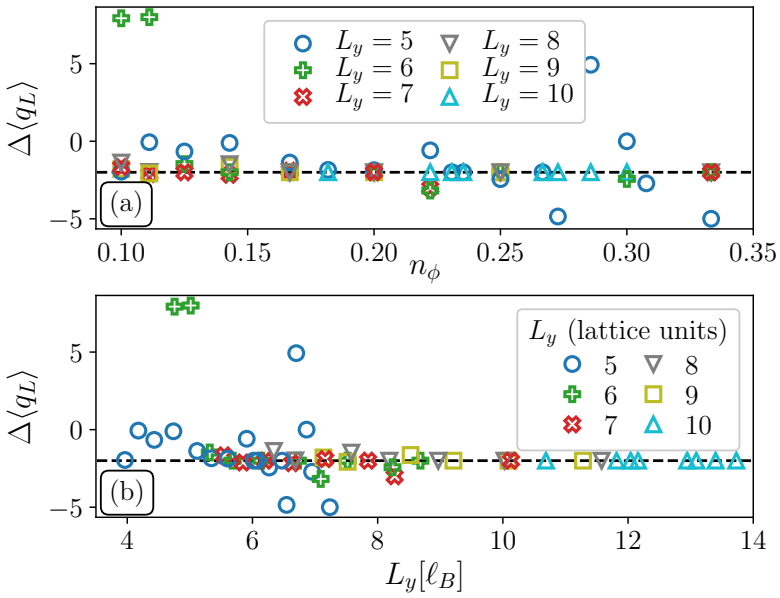

FIGURE 5.12: Total charge transported on insertion of $5 \times 2\pi$ external flux at various flux densities n_ϕ (a) and various circumferences, in units of the magnetic length ℓ_B (b). In all cases, $V = 10$, $\chi = 400$. The dashed horizontal line shows $\Delta\langle q_L\rangle = 2$, which is the expected value for a $\nu = 2/5$ state. Details of the charge transport for points within $\Delta\langle q_L\rangle = 2 \pm 0.01$ are shown in figure 5.11.

$\chi = 800$ in Andrews, Mohan, and Neupert (2020) and is replicated here. Figure 5.13(a) shows the momentum-resolved entanglement spectrum for this case.[6] The spectrum shows good qualitative agreement with the result from Andrews, Mohan, and Neupert (2020) in the $q = 0$ sector and the $q = 1$ sector (although in the latter case, the levels are shifted in k_y with respect to the $q = 0$ sector. There are differences in the $q = -1$ sector, however, and for $|q| > 1$ qualitative differences are difficult to distinguish. The density profile corresponding to this state (not shown here) is an exact match for that shown in Andrews, Mohan, and Neupert (2020) under some periodic shift along the cylinder.

Figure 5.13(b) through (d) show spectra for the $\nu = 2/5$ state at flux densities $n_\phi = p/q$ with $p > 1$, i.e., in cases where the fractional state is supported on multiple subbands. We see that all spectra look qualitatively similar, although there seems to be a reversal in the patterns of the $q = 0$ and $q = 1$ sectors between $p \leq 2$ [figures 5.13(a) and (b)], and $p \geq 3$ [figures 5.13(c) and (d)].

5.3.3 Topological entanglement entropy

A collection of data for the entanglement entropy at various flux densities n_ϕ and cylinder circumferences L_y, similar to those shown in figures 5.6 and 5.7, is shown in figure 5.14. The figure shows outliers for $n_\phi = 2/7$ and $n_\phi = 2/9$, as well as some non-linear behaviour for $L_y \lesssim 5\ell_B$. The theoretical prediction for the topological entanglement entropy of the $\nu = 2/5$ state is again given by (5.4) and (5.5), now with 5 particles with $d_a = 1$ each. Thus, we find a predicted $S_{\text{topo}} = -\log\sqrt{5} \approx -0.805$ (the dotted blue line in figure 5.14).

An extrapolation of all data with $L_y > L_y^{(\text{min})} = 10\ell_B$ (the black dashed line in figure 5.14) to find the topological entanglement entropy yields $S_{\text{topo}} \approx -0.735 \pm 0.227$. This

[6] Again, additional spectra can be found in Schoonderwoerd (2020).

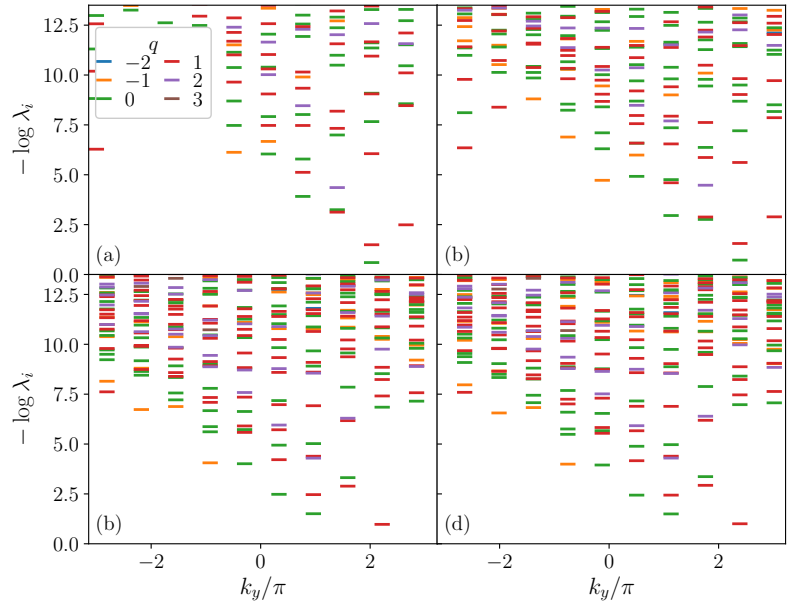

FIGURE 5.13: Momentum-resolved entanglement spectrum for $L_y = 10$, $V = 10$ at a particle density commensurate with a filling fraction $\nu = 2/5$. Flux densities are (a) $n_\phi = 1/7$, (b) $n_\phi = 2/11$, (c) $n_\phi = 3/13$ (d) $n_\phi = 4/17$. Different colours denote different quantum number sectors (with the $q = 0$ sector additionally denoted with crosses). The spectra have been shifted along k_y so that the 'chiral tail' is most clearly visible. Momenta and quantum numbers carry physical meaning only in a relative sense. For $n_\phi = 1/7$ (a), the chiral tail in the $q = 0$ sector matches with Andrews, Mohan, and Neupert (2020) [figure 2(b)]. The $q = 1$ sector also matches with that work, but seems to be shifted in k_y with respect to the $q = 0$ sector. There is a clear difference in levels for the the $q = -1$ sector, and differences or similarities in sectors with $|q| > 1$ are difficult to see quantitatively

result is highly sensitive to the selection of data points. For example, raising the cut-off to $L_y > L_y^{(\mathrm{min})} = 11\ell_B$ instead gives an extrapolated $S_{\mathrm{topo}} \approx -0.778 \pm 0.150$. A more comprehensive overview of the relation between the cut-off $L_y^{(\mathrm{min})}$ and the extrapolation for S_{topo} and its error bars is shown in figure 5.15.

To further illustrate the accuracy of our result, a dash-dotted red line has been added to figure 5.14 with the same slope as the fit on $L_y > 10\ell_B$, but with the intersect adjusted to match the theoretical prediction exactly. This adjusted fit still shows reasonable agreement with the data.

We can compare this result to that of Andrews, Mohan, and Neupert (2020), who found an extrapolated $S_{\mathrm{topo}} \approx 0.850 \pm 0.103$. That extrapolation was made using four data points above a threshold value $L_y > 9.47\ell_B$. This small number of data points was due to much more stringent selection criteria on which data points to include in the extrapolation. Regardless, there is reasonable agreement between those result and the results presented here. However, as the work in Andrews, Mohan, and Neupert (2020) uses a DMRG implementation closely related to ours (Hauschild and Pollmann, 2018), which includes a model code implemented by the author of this thesis based on the code used for this thesis, the agreement between these results and ours should not be taken as conclusive evidence.

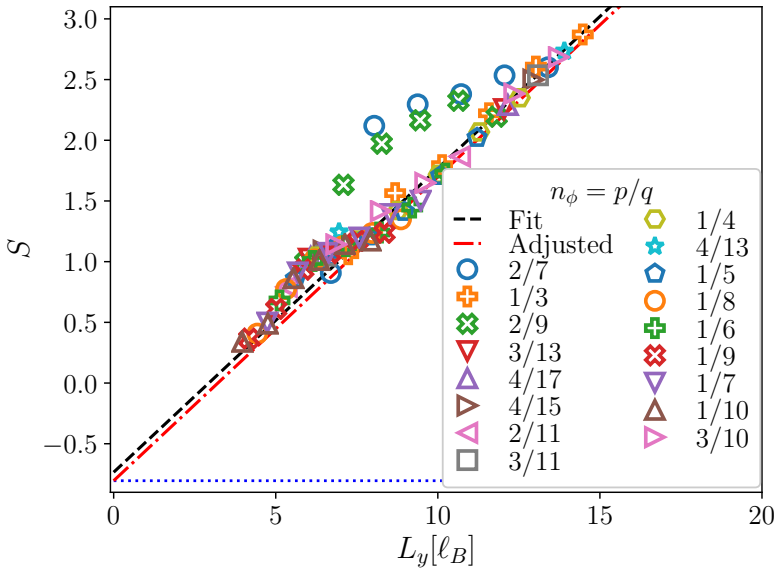

FIGURE 5.14: Entanglement entropy for the $\nu = 2/5$ state at a range of flux densities n_ϕ and circumferences L_y (in units of ℓ_B). The dotted blue line denotes the theoretical prediction $S_{\text{topo}} = -\log\sqrt{5} \approx -0.805$. The dashed black line is a fit to all data with $L_y/\ell_B > 10$ (ignoring the obvious outliers at $n_\phi = 2/7$ and $n_\phi = 2/9$). It yields an estimate for $S_{\text{topo}} \approx -0.735 \pm 0.227$. However, this estimate is sensitive to the selection of data points. For example, raising the cut-off to $L_y/\ell_B > 11$ gives an extrapolated $S_{\text{topo}} \approx -0.778 \pm 0.150$. The dash-dotted red line therefore denotes the same fit (with $L_y/\ell_B > 10$), but with the intersect adjusted to be exactly at $-\log\sqrt{5}$, to demonstrate the relative accuracy of the fit.

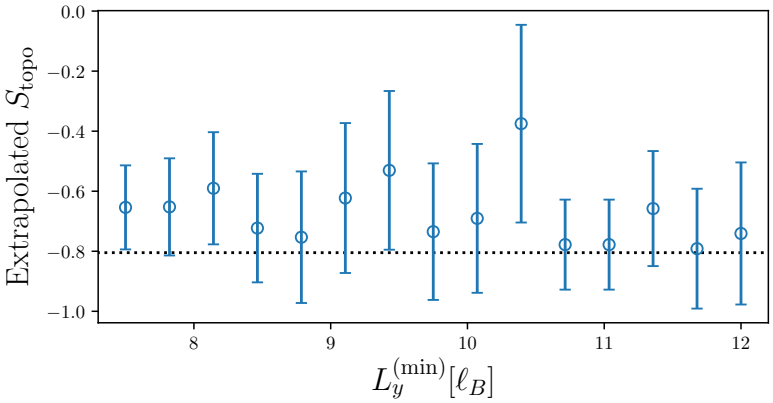

FIGURE 5.15: Values for S_{topo} for the $\nu = 2/5$ data, obtained from a linear extrapolation of the data in figure 5.14 with various cut-offs $L_y > L_y^{(\text{min})}$. Error bars show the error of the best fit at one standard deviation.

5.4 Discussion

In conclusion, this chapter has demonstrated results improving the understanding of FQH states in the Harper-Hofstadter model in two main ways. Firstly, we have shown states exhibiting properties of the $\nu = 1/3$ Laughlin state, as well as the next hierarchy state at $\nu = 2/5$, to be stable over a wide range of flux densities n_ϕ. This includes both the cases $n_\phi = 1/q$ where much prior research has been done, as well as the cases $n_\phi = p/q, q > 1$ for which this result is often assumed, but not explicitly examined previously.

Secondly, we have shown universality in the entanglement scaling behaviour of $\nu = 1/3$ Laughlin-like FCI states for all studied cases when using ℓ_B as length scale. Similar results were obtained for $\nu = 2/5$ states. These results demonstrate both that ℓ_B is the relevant length scale for the study of entanglement properties in these kinds of systems, as well as the fact that all these n_ϕ support equivalent states. Moreover, this universal scaling provides a route for improving numerical results, by combining results for several equivalent states at varying n_ϕ. In this way, the numerical cost associated with finite-circumference scaling (which is a limiting factor largely due to the area law of the entanglement entropy) can be minimised, while simultaneously obtaining a significantly larger number of data points with better coverage of the circumference axis.

There are several avenues to extending these results beyond this thesis. Firstly, an obvious extension is the study of FCI states further along the hierarchy of filling fractions (section 2.3.2) on single- and multiple-sub-band incarnations of the LLL. Secondly, it would be interesting to extend this study to FCI states that exist not on the entire LLL tail, but on one or more sub-bands within this tail. For example, the work of Andrews and Möller (2018) studies FCI states supported on single Harper-Hofstadter sub-bands with $|C| > 1$. This work could be extended by using DMRG instead of, or in combination with, the exact diagonalisation studies already performed, to study FCI states in $|C| > 1$ bands throughout the Harper-Hofstadter model.

Finally, there exists a 'zoo' of QH states described by non-Abelian theories (Wen, 1991; Moore and Read, 1991; Papić, 2014). It is conceivable that methods such as those described in this chapter can shed more light on these states.

Chapter 6

Integer-to-fractional Chern Insulator plateau transition

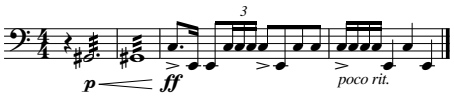

Sergei Prokofiev, *Peter and the Wolf, Op.67*

Conductivity-changing transitions between quantum Hall (QH) states have historically attracted much attention (Wei et al., 1988; Engel et al., 1990; Huckestein, 1995; Sondhi et al., 1997). These transitions are commonly called *plateau transitions* as they can be interpreted as transitions between distinct plateaus in the Hall resistivity, see figure 2.2. Conventionally, QH plateau transitions are driven by the filling of Landau levels being tuned by a change in magnetic field strength. The critical properties of such transitions can be understood in terms of the percolation of current-carrying modes (Huckestein, 1995), which are captured by network models (Chalker and Coddington, 1988) or renormalisation group approaches (Khmelnitskii, 1983; Kivelson, Lee, and Zhang, 1992).

In clean systems, i.e., systems where the transition cannot be due to some disorder (such as is the case with percolation transitions as described in section 2.2.4), several scenarios for transitions into or between fractional quantum Hall (FQH) states have also been described (Wen and Wu, 1993; Chen, Fisher, and Wu, 1993; Ye and Sachdev, 1998; Grover and Vishwanath, 2013; Barkeshli and McGreevy, 2014; Barkeshli, Yao, and Laumann, 2015; Lee et al., 2018). These transitions are often understood as transitions in the underlying composite fermion (CF) (Lee et al., 2018) or parton description (Barkeshli and McGreevy, 2014), changing the Chern number of the system. The critical point is then described by a massless multi-flavour Dirac theory coupled to a gauge field (Grover and Vishwanath, 2013; Barkeshli and McGreevy, 2014; Lu and Lee, 2014; Lee et al., 2018). A microscopic realisation was found in graphene heterostructures, where transitions between fractional Chern insulator (FCI) states within the same Jain series can be driven by tuning the strength of a periodic potential (Lee et al., 2018).

In this chapter,[1] we explore QH plateau transitions as present in the fermionic Harper-Hofstadter model. We drive these transitions using the ratio of interaction strength to the tunnelling parameter V/t.[2] In particular, we study transitions between integer and fractional QH states that are not captured by any of the scenarios listed above. In section 6.1, we describe the essential idea underlying these transitions. Section 6.2 describes our

[1] Part of the content of this chapter has appeared previously in Schoonderwoerd, Pollmann, and Möller (2019).

[2] Throughout the discussion here, we set $t = 1$, so we will refer to V and V/t interchangeably.

results for a particular case of such a transition, namely a transition between an integer Chern insulator (ICI) state with Chern number $C = +4$ and a $\nu = 1/3$ Laughlin state. Sections 6.4 and 6.5 investigate this case further, with section 6.4 looking at the behaviour of the critical point as function of circumference L_y and Matrix Product State (MPS) bond dimension χ, and section 6.5 studying the putative central charge of a theory describing the critical system. Section 6.6 gives a more comprehensive overview of the possible routes towards a theoretical description. Finally, 6.7 extends the work to the next state in the FQH hierarchy at $\nu = 2/5$.

6.1 Competing integer and fractional states in the lowest Landau level (LLL) Harper-Hofstadter tail

We consider the Harper-Hofstadter model as introduced in chapter 4 at a specific flux density $n_\phi = p/q$. At such a rational flux density, the model has q (sub-)bands, with each band containing an (areal) density of states $n_{s,\text{band}} = 1/q$. The main gap in the Hofstadter butterfly (section 4.2.1) is found at a particle density $n = n_\phi$. The p sub-bands below this gap form the lowest Landau level (LLL) 'tail'. If we treat the LLL tail as a single object, it has a density of states $n_s = pn_{s,\text{band}} = p/q = n_\phi$.

We can imagine a scenario in which the lowest m bands are completely filled with non-interacting fermions, i.e., $n = mn_{s,\text{band}} = m/q$. Such a filling would result in an ICI state.[3] At these same flux- and particle densities, we obtain a filling fraction $\nu = m/p$ in the LLL tail. Should this filling fraction equate to

$$\nu = \frac{n}{n_s} = \frac{r}{kCr+1}, \tag{6.1}$$

with $k \in \mathbb{Z}$ the number of flux quanta attached to each electron in the CF picture (section 2.3.3), and $r \in \mathbb{Z}$ the number of bands filled by the CFs, there is a candidate FCI state at this same configuration (Möller and Cooper, 2015). Thus, we find the potential for a direct competition between integer and fractional Chern insulator (CI) states at constant n and n_ϕ.

For a more concrete example, to obtain a $\nu = 1/3$ Laughlin-like state in the $C = 1$ LLL would require $r = 1$, $k = 2$. Consequently, this state would be present at $n_s = n_\phi = p/q$ when $m = p/3$, i.e., $n = m/q = p/3q$. The simplest case for an integer $m > 0$ is $p = 3$. Note that here, q is a free parameter, effectively allowing us to tune the magnetic length ℓ_B as was discussed in section 5.1.2. As q also influences the size and shape of the MPS unit cell (see section 4.4) and the MPS unit cell must contain an integer number of particles, some additional constraints may necessarily be imposed. Additionally, if q is chosen too small, the large dispersion of the sub-bands could destabilize the fractional state (Hafezi et al., 2007). In sections 6.2 through 6.5, we will focus on the case $q = 11$, i.e., $n_\phi = 3/11$.

This begs the question which of the two candidate states (the $\nu = 1/3$ Laughlin state or the $C = +4$ ICI) is favoured as we change the interaction strength V. We present the following heuristic: For a non-interacting model, the ground state is supported only by the lowest sub-band, which will be completely filled. However, upon increasing inter-particle interactions V/t, a trade-off between the particles' kinetic and interaction energy is introduced. Particles can stay in the lowest sub-band, in which their proximity will cause an interaction penalty to the ground state energy. Alternatively, particles can be excited into higher sub-bands, incurring a penalty to their kinetic energy in favour of

[3] This is what motivates our choice of a fermionic model. We require the ICI state to be stable at low, or even zero, interaction, where a bosonic system would condense into a Bose-Einstein condensate or super-solid state (Möller and Cooper, 2010).

a reduced interaction energy, as the particles can now minimise their relative distances. This heuristic predicts a critical interaction strength V_c/t at which the ICI state will no longer be a ground state, and the FQH state will be favoured.

It should be carefully noted that this heuristic is very rough, and provides no prediction for the existence or absence of any candidate intermediate states (of any kind, be it QH or a different phase) between the ICI and FCI states. In this thesis, whether or not intermediate or non-QH phases appear during the increase of V_c will be studied using numerical data. The next section will introduce results that demonstrate that such an intermediate state does not (always) appear. A more comprehensive attempt at a theoretical framework for our results will be given in section 6.6.

6.2 Integer-to-fractional plateau transition at $n_\phi = 3/11$

In section 6.1, the idea of competing QH states (integer and fractional) at the same Harper-Hofstadter flux density was introduced. In this section, we will see an example of such a competition. We will focus on the model at a flux density $n_\phi = 3/11$, where there are 3 sub-bands in the LLL tail. We tune particle density to a configuration that can either completely fill the lowest sub-band, or realise a $\nu = 1/3$ filling on the entire 3-sub-band LLL tail. The state in the lowest band is expected to realise a $C = +4$ ICI (see section 4.3). To investigate a potential phase transition between these two regimes, we observe the response of the system when tuning interaction strength V (see equation 4.1), keeping the hopping amplitude t constant. We should note that it is the relative magnitude V/t that is important here, so that we could alternatively fix V and tune t. This will not change any of the results shown below.

6.2.1 Evidence for a direct phase transition

In chapter 5, we have already observed that an FQH state exists for $n_\phi = 3/11$ at sufficiently high V. A similar investigation shows the existence of a $C = +4$ ICI for small values of V. We here examine whether a direct phase transition can be found between these two states. To the extent that our data, obtained with the Density Matrix Renormalization Group (DMRG), can capture the physics, figures 6.1, 6.4 and 6.5 (which have $L_y = 6$, $L_y = 7$ and $L_y = 8$, respectively) appear to indicate that this is indeed the case. The transition appears most clearly at $L_y = 6$, where figure 6.1 shows several observables over a range of values for V. As we will show below, the results are somewhat less clear for larger circumferences. The interaction strength V at which the transition is suspected will be denoted with V_c henceforth.

We should note here that determining the order of a quantum phase transition using MPSs is not a straightforward task. Due to the nature of the MPS representation, presuming an exact representation of the ground state requires the bond dimension χ to scale exponentially with circumference L_y. The bond dimension therefore is necessarily truncated to $\chi_{\max}$, which implies the approximate state will fail to capture long-range correlations. For a non-critical point in phase space, this is not problematic, as the correlation length in such a case scales inversely with the gap. However, if we happen to be targeting the critical point of a continuous quantum phase transition, we need to capture algebraic correlations. The exact ground state would then exhibit a correlation length tending to infinity, $\xi \to \infty$. This cannot be represented by a finite-χ MPS, so the MPS representation will behave as if the correlation length is large but finite. It is therefore difficult to discern a 'true' continuous phase transition from a first-order transition using MPS methods.

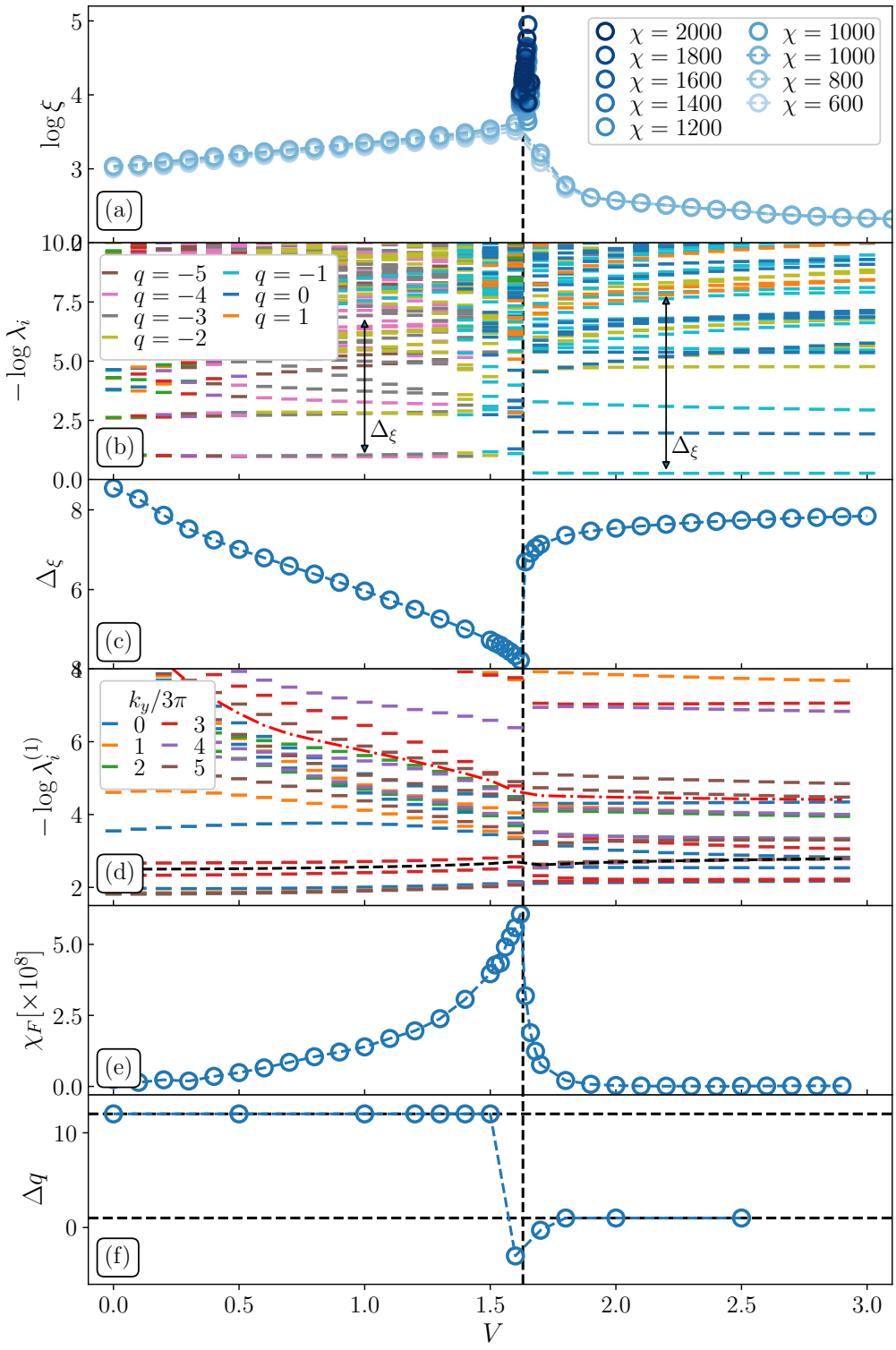

FIGURE 6.1: Several observables through the transition (dashed line) at $L_y = 6$, $n_\phi = 3/11$, $\chi = 500$ [except $600 \leq \chi \leq 1000$ in (a)]. (a) Correlation length (in lattice sites) for several values of the bond dimension. The circumference $\log L_y \approx 1.79$ falls below the range shown. (b) Momentum-space entanglement spectrum (colours denote different quantum number sectors). Also shows the entanglement gap. (c) Entanglement gap. (d) Spectrum of the single-particle density matrix. The dashed line indicates the lowest 6 (18) states on the left (right) of the transition. (e) Fidelity susceptibility $\chi_F = (|\langle\psi(V)|\psi(V+\delta V)\rangle|^2 - 1)/(\delta V)^2$. (f) Charge $\langle\Delta q\rangle$ transported along the cylinder by the insertion of $3 \times 2\pi$ flux.

The first sign of a phase transition is found in the correlation length ξ. Near V_c, our data for $\xi(\chi)$ suggest a divergence with bond dimension, as well as with $|V - V_c|$, for $L_y = 6$ and $L_y = 8$ [figures 6.1(a) and 6.5(a)]. This is consistent with a continuous quantum phase transition occurring at V_c. Some additional data for $\chi \leq 2000$ can be found in figure 6.10 (subfigure (d) for the case we discuss here). At $L_y = 7$ [figure 6.4(a-b)], however, rather than a sharp discontinuity, we observe both the entanglement entropy and correlation length varying more or less smoothly with V. We do identify a minor discontinuity at $V = 1.5$. This suggests a potential distinction between the case at $L_y = 7$, and those at $L_y = 6$ and $L_y = 8$. However, it is possible that the results at $L_y = 7$ require a higher bond dimension to fully resolve the transition.

6.2.2 Entanglement properties

A signature of the phase transition can be seen in the entanglement entropy S associated with a bisection of the infinite cylinder. Results for this at $L_y = 6$ and $L_y = 8$ at $\chi \leq 1000$ are found in figure 6.9, with results for $L_y = 7$ in figure 6.4(b).[4] Additional results with $\chi \leq 2000$ are shown in figure 6.10. In both figures, we note that, similar to the results for ξ, S shows both a discontinuity or peak, and a sharp increase with χ at $V \sim V_c$ for both $L_y = 6$ and $L_y = 8$. The feature is most pronounced at $L_y = 6$. As mentioned before, no such sharp feature is found at $L_y = 7$, where the entanglement entropy varies smoothly with V. That said, there is a region (at $1.2 \leq V \leq 1.5$) where the slope of $S_E(V)$ is steepest and appears to be increasing with χ. Hence, it could again be the case that a more pronounced transition would be found at higher χ.

Additionally, the momentum-resolved entanglement spectrum $\{-\log \lambda_i(k_y)\}$ of the Schmidt decomposition of the infinite Matrix Product State into two half-infinite states (see section 3.2.3)

$$|\Psi\rangle = \sum_{i,k_y} \lambda_i(k_y) \, |\chi^L_{i,k_y}\rangle \otimes |\chi^R_{i,k_y}\rangle \tag{6.2}$$

is shown in figures 6.1(b), 6.4(c) and 6.5(c) for $L_y = 6$, $L_y = 7$ and $L_y = 8$, respectively. To further illustrate the difference between the two phases, the full entanglement spectrum of states in the two phases at $L_y = 6$ are shown in figure 6.2. At V_c, the spectrum for $L_y = 6$ displays a sudden opening of the lowest gap, as well as other discontinuous changes at higher entanglement energies. No such sharp change can be observed at either $L_y = 7$ or $L_y = 8$, which instead are characterised by several level crossings in the lower parts of the spectrum.

In the entanglement spectrum, we define the entanglement gap Δ_ξ as the gap between the lowest two levels within the same quantum number and momentum sector. As the arrows in figure 6.1(b) show, this is *not* the smallest gap between any two states. The arrow in figure 6.2(b) further illustrates this point. Figure 6.1(c) shows a discontinuity of Δ_ξ at V_c, and a tendency of the gap to decrease for $V < V_c$ approaching the transition at $L_y = 6$. Discontinuities appear as well in the entanglement gap for $L_y = 7$ [figure 6.4(d)]

[4] For figures such as figure 6.1, figure 6.9, or any other figure showing the change of some observable as a function of V, a method very similar to that of flux insertion is used. A ground state MPS is obtained at low (or high) V, which is then used as the initial guess for a slightly larger (or smaller) $V \pm \delta V$. This pseudo-adiabatic procedure is repeated until the largest (smallest) V is reached. For results such as those in figure 6.9, in which there is both a V-dependence as well as a χ-dependence, a semi-adiabatic 'sweep' through V is performed first, after which finite entanglement scaling (essentially a pseudo-adiabatic increase in χ following the same procedure as the sweep through V) is performed independently for each of the states obtained this way. We choose this procedure because, while scaling up χ can be done in parallel for different independent values of V, a sweep can only be performed sequentially. Thus, running the sweep at large χ, where each data point takes longer to calculate, would take much more time than running the sweep at low χ.

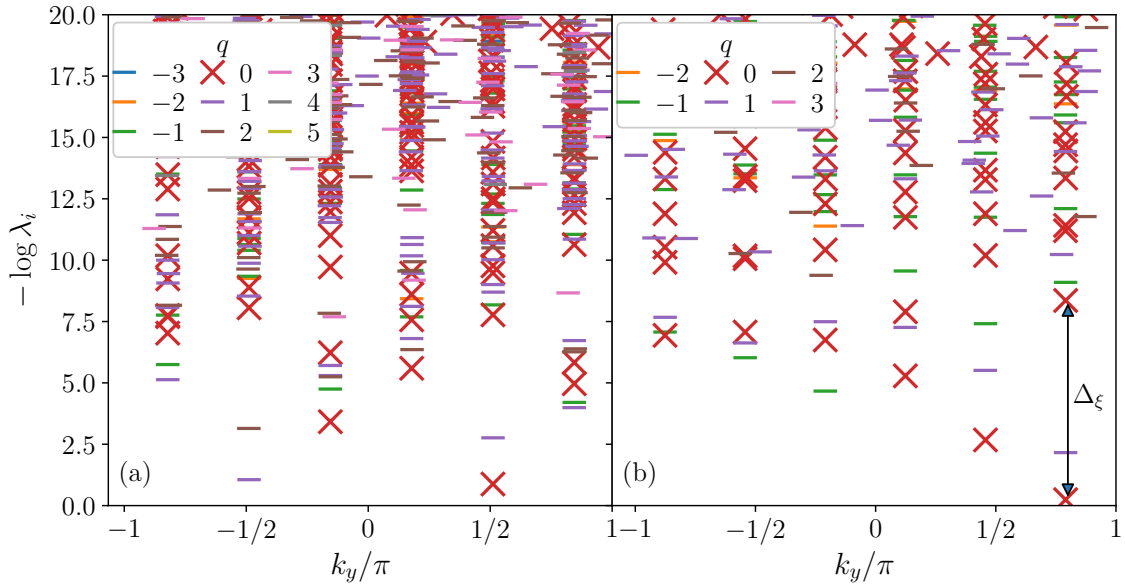

FIGURE 6.2: Momentum-resolved entanglement spectra deep in the integer (a, $V = 0.5 < V_c$) and $\nu = 1/3$ fractional (b, $V = 5 > V_c$) phases at $n_\phi = 3/11$. $\chi = 2000$, $L_y = 6$. Different quantum number sectors (denoted with different colours) carry meaning only relative to each other. We can clearly observe the chiral tail in the fractional phase (b), and the lack thereof (as well as almost-degeneracies between lowest levels in two different sectors) in the integer phase (a).

and $L_y = 8$ [figure 6.5(d)], but these can be ascribed to level crossings causing the gap to suddenly be measured within different momentum and charge sectors, rather than a closing of the gap. Nonetheless, in these cases too we find a tendency of the gap to decrease near V_c. Thus, the existence of a phase transition is also supported by the entanglement properties of the system.

6.2.3 Single-particle density matrix

We study the single-particle density matrix $\rho_{ij} = \langle\psi|c_i^\dagger c_j|\psi\rangle$, which can be transformed to momentum space using the Fourier transformation of the creation- and annihilation operators. Transforming only the y-coordinate (and thus obtaining a mixed real space-momentum basis), we have

$$\hat{c}_{x,y} = \frac{1}{\sqrt{L_y}} \sum_{k_y=0}^{L_y-1} e^{i2\pi k_y y/L_y} \hat{c}_{x,k_y}, \tag{6.3}$$

and thus

$$\langle c_{x,k_y}^\dagger c_{x'k_y'} \rangle = \frac{1}{L_y} \sum_{yy'} e^{i2\pi(k_y y - k_y' y')/L_y} \langle c_{xy}^\dagger c_{x'y'} \rangle . \tag{6.4}$$

We combine this resummation with a trivial reordering of the basis to make k_y the dominant index, leading to a matrix that is block-diagonal in momentum sectors [figure 6.3(b)]. The spectrum of the matrix remains unchanged throughout this procedure [figure 6.3(a)]. This change of basis allows us to classify each eigenvalue by its k_y sector, shown in terms of the colouring of symbols in figures 6.1(d), 6.4(e) and 6.5(e) (again, $L_y = 6$ through 8, respectively), and supporting the corresponding analysis.

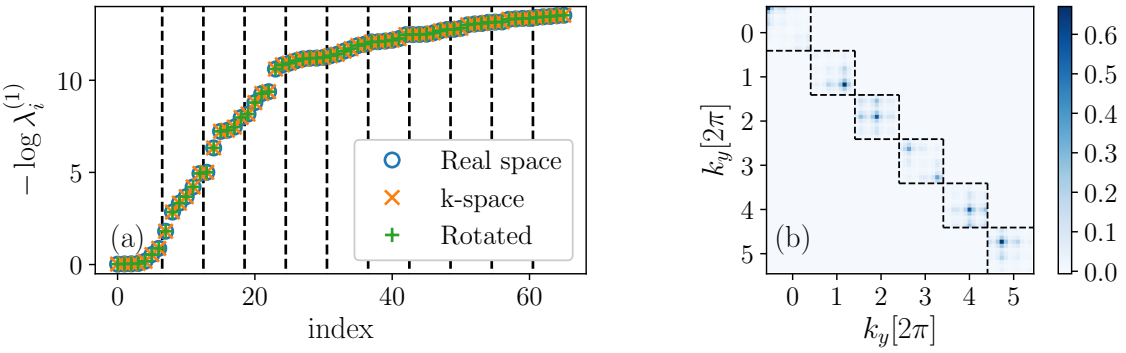

FIGURE 6.3: The single-particle density matrix at $L_y = 6$. (a) The spectrum of the matrix remains unchanged under the transformations described in the main text, and equations 6.3 and 6.4. Vertical dashed lines separate every 6 consecutive values. (b) After the final reordering of the indices, the matrix is block-diagonal in k_y. Each block contains 11×11 values, due to the size (in $\hat{\mathbf{x}}$) of the magnetic unit cell and MPS unit cell.

Figures 6.1(d), 6.4(e) and 6.5(e) display the spectrum of the single-particle density matrix $\rho_{ij}^{(1)} = \langle \hat{c}_j^\dagger \hat{c}_i \rangle$ calculated within our MPS unit cell of $1 \times L_y$ magnetic unit cells[5] for $L_y = 6$, $L_y = 7$ and $L_y = 8$, yielding L_y distinct k_y-points in reciprocal k_y-space (with k_x free).

The spectrum for the ICI phase at $L_y = 6$ is dominated by six low-lying eigenvalues and a seventh nearby. This includes at least one state for each of the k_y-points. In the FCI phase at $L_y = 6$, a gap is found above 18 low-lying states and two further nearby states. This includes at least three states for each of the k_y-points. A similar picture is found at $L_y = 8$, with the main gap in the ICI phase separating eight eigenvalues, one from each k_y sector plus one or two more, from the bulk. On the FCI side of the transition, we find a gap above 24 low-lying states (three from each k_y sector) plus another three. Apart from the additional nearby states, for which we have no explanation, these numbers are consistent with the expectation that in the ICI phase only states in the lowest band contribute significantly to $\rho_{ij}^{(1)}$. Contrarily, in the fractional phase, $\rho_{ij}^{(1)}$ is expected to involve all states in the LLL (i.e., three bands in this case) for the Laughlin state (Sterdyniak, Regnault, and Möller, 2012), which again is borne out by our results.

In contrast with the results for $L_y = 6$ and $L_y = 8$, it is much more difficult to identify a dominant gap in the spectrum of ρ_{ij} at $L_y = 7$ [figure 6.4(e)], except for $1.2 \leq V \leq 1.6$ (and perhaps at lower V as well). There is no clear gap above either the lowest 7 or the lowest 21 levels. This could be taken to suggest that the $L_y = 7$ case is qualitatively distinct from the cases at $L_y = 6$ and 8. However, as before, this difference can also be due to a numerical issue, rather than a physical one.

Looking for indications of a phase transition, we observe that at $L_y = 6$, the spectrum of $\rho_{ij}^{(1)}$ as function of V shows a discontinuous change between the ICI and Laughlin states at V_c. This is again consistent with a phase transition at V_c. Both $L_y = 7$ and $L_y = 8$ exhibit different behaviour. Neither of these cases show abrupt or discontinuous changes in the spectrum. There are some qualitative differences between the spectra at low and high V, but the spectra seem to evolve continuously as a function of V. At $L_y = 7$, a gap appears to open up for $1.2 \leq V \leq 1.6$, and some level crossings can be observed. Discontinuous changes can be conjectured at several values of V, but we are reluctant

[5] I.e., a $11 \times L_y$ MPS unit cell in terms of lattice sites at $n_\phi = 3/11$.

to identify any V as showing a strong discontinuity. At $L_y = 8$, a gap at low V closes and another gap at high V opens up (consistent with the discussion on the number of levels given above), with some level crossings occurring in the intermediate regime. It is possible that this pattern will appear sharper at higher bond dimensions.

6.2.4 Further evidence

Figures 6.1(e), 6.4(f) and 6.5(f) (for $L_y = 6, 7, 8$, respectively) show the fidelity susceptibility

$$\chi_F = \frac{1 - |\langle \psi(V) | \psi(V + \delta V) \rangle|^2}{(\delta V)^2}, \tag{6.5}$$

which provides a measure of the overlap between states separated by a small δV. At $L_y = 6$, we find that χ_F shows an upwards peak at V_c, indicating that near V_c states are changing rapidly as function of V, and thereby also supporting a direct phase transition. At $L_y = 7$, χ_F exhibits a dip around $V = 0.9$, but no sharp features otherwise. No other observable indicates a feature at this V. At $L_y = 8$, too, there are no sharp features in χ_F, although there is a clear onset of a stable phase at $V = 1.7$. This onset seems to be consistent with the end of the intermediate regime identified in the entanglement and single-particle density matrix spectra mentioned above, although it occurs at slightly higher V than where discontinuities in S_E and ξ are observed.

Finally, we measure the Hall conductance using flux insertion (Laughlin, 1981; Thouless et al., 1982). Due to the large computational cost associated with this procedure, we have only performed it for the smallest cylinder, with $L_y = 6$. A more detailed description of flux insertion was given in section 2.4; we repeat the key points here. We calculate the evolution of the ground state under an adiabatic insertion of $3 \times 2\pi$ external flux through the cylinder, and measure the charge Δq thereby transported along the cylinder. This methodology has recently been used successfully to diagnose QH physics in a range of systems (Zaletel, Mong, and Pollmann, 2014; Grushin et al., 2015; Motruk et al., 2016; Motruk and Pollmann, 2017). The total charge transported as a consequence of flux insertion is related to the Hall conductivity by $\sigma_H = \Delta q / \Delta \phi_{\text{ext}}$.

Flux insertion for $V = 0$ confirms that the system realizes an ICI state, finding a Hall conductivity proportional to the Chern number of the lowest Harper-Hofstadter band, $\sigma_H \propto C_1 = 4$ (see section 4.3.1). Figure 6.1(f) shows that this picture persists for small $V > 0$. Conversely, at interaction strengths $V > V_c$, we find $\sigma_H = 1/3$, consistent with the prediction for a $\nu = 1/3$ Laughlin state. Near V_c, the Hall conductivity $\sigma_H(V)$ discontinuously jumps between these two extremal values. It is this instantaneous and discontinuous shift in σ_H that makes the phase transition studied here a *plateau transition*.

Near V_c limited computational resources prevent us from reliably performing the flux pumping procedure. This failure is manifested in the violation of adiabaticity during the flux insertion procedure, evidenced by discontinuities in $\langle q_L(\phi) \rangle$. This is understood by the increase of the correlation length near V_c, requiring larger bond dimensions than we are able to attain to fully capture the many-body state.

6.3 Scaling of ξ and S_E with χ

In this section, we take a closer look at the scaling of our two most important observables, the correlation length ξ and entanglement entropy S_E, with bond dimension χ.[6] Here, we expand the set of scaling results to cover all circumferences, and investigate scaling with

[6] Note that scaling with the other primary parameter, V, can be seen in figure 6.10.

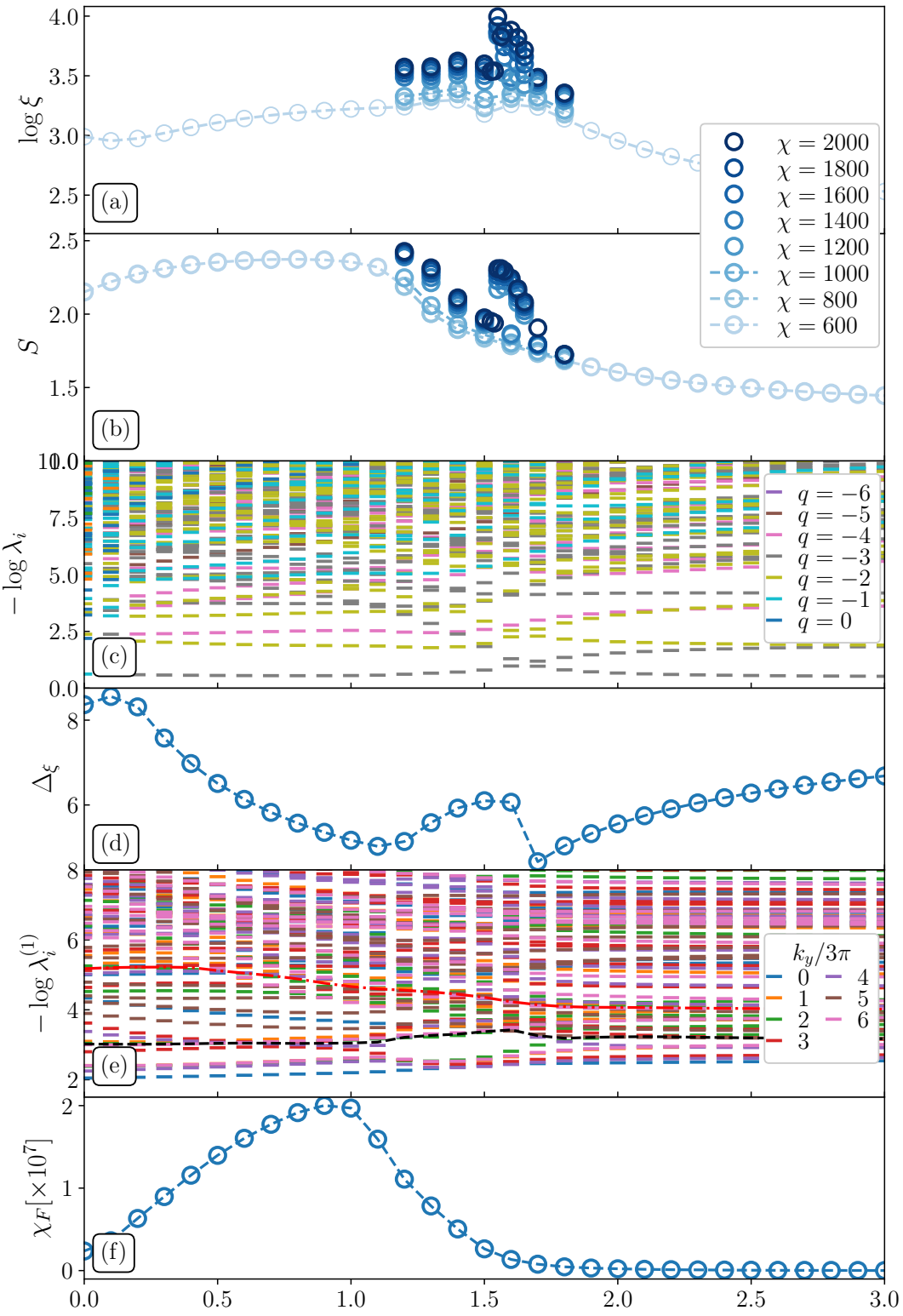

FIGURE 6.4: The plateau transition at $L_y = 7$. Shown are: (a) Correlation length in lattice sites (the circumference $\log L_y \approx 1.95$ falls below the range shown.) and (b) entanglement entropy for several values of the bond dimension $600 \leq \chi \leq 1000$ (c) Momentum-space entanglement spectrum (colours denote different quantum number sectors). (d) Entanglement gap. (e) Spectrum of the single-particle density matrix. The dashed black and dash-dotted red lines denote the lowest 7 and 21 levels, respectively. (f) Fidelity susceptibility χ_F. Subfigures (c) through (f) have $\chi = 600$.

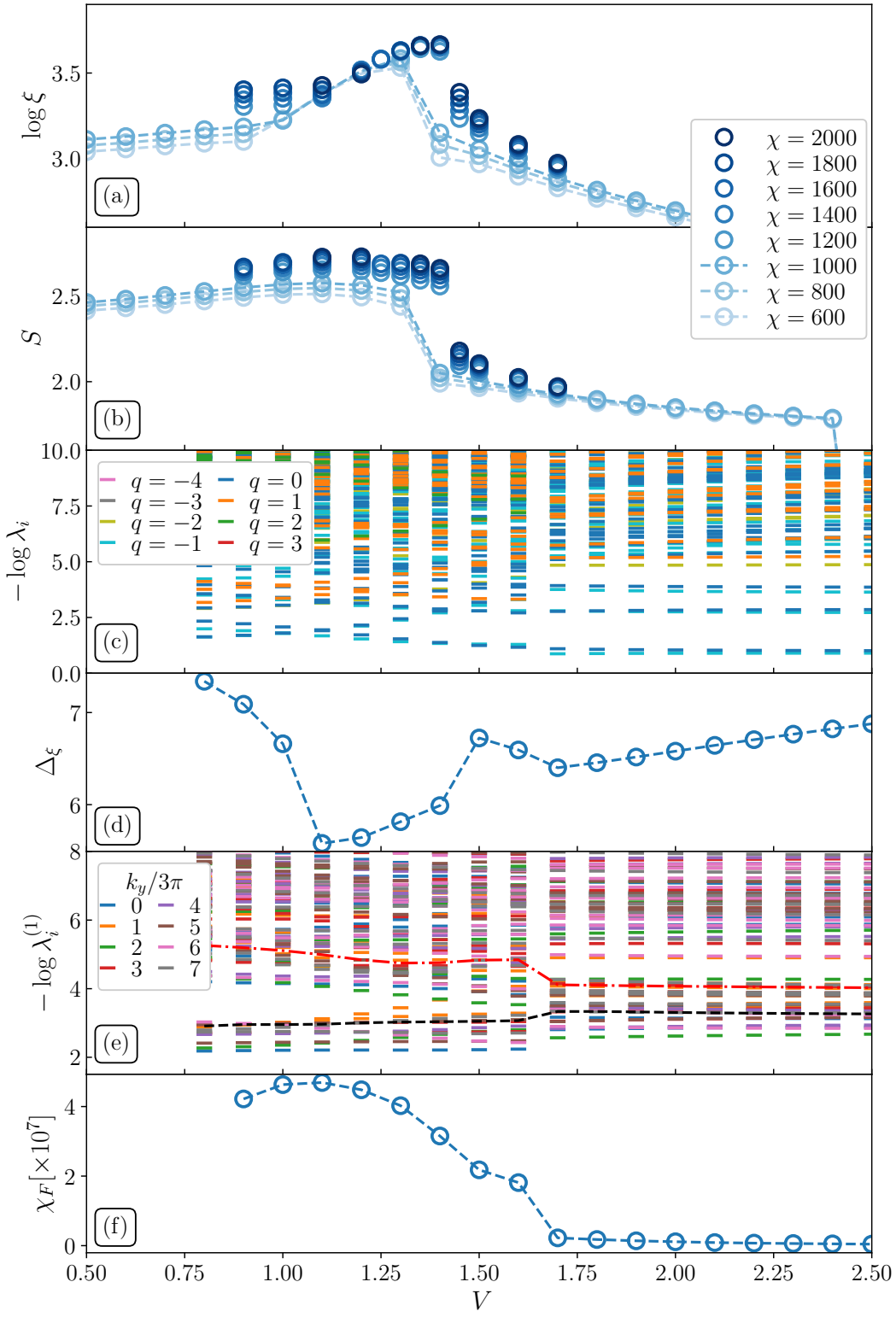

FIGURE 6.5: The plateau transition at $L_y = 8$. Shown are: (a) Correlation length in lattice sites (the circumference $\log L_y \approx 2.089$ falls below the range shown) and (b) entanglement entropy for several values of the bond dimension $600 \leq \chi \leq 2000$ (c) Momentum-space entanglement spectrum (colours denote different quantum number sectors). (d) Entanglement gap. (e) Spectrum of the single-particle density matrix. The dashed black and dash-dotted red lines indicate the lowest 8 and 24 levels, respectively. (f) Fidelity susceptibility χ_F. Subfigures (c) through (f) have $\chi = 600$.

both bond dimension χ. Figures 6.6, 6.7 and 6.8 show these results for $L_y = 6, 7$ and 8, respectively.

We turn our attention first to the results for $L_y = 6$, in figure 6.6. For some values of V, we observe values jumping between two regimes as χ increases. While we are unsure of the precise reason this happens (although we note that it occurs only in a fairly narrow band of values for V, where the system is close to criticality and thus highly susceptible to possible convergence issues), we note that the effect is reduced by the procedure of 'pushing away the boundaries', which we will further describe in section 6.5. Other than this effect, we note that both ξ and S_E appear to increase systematically with χ, as one would expect.

In figure 6.7, we observe a systematic increase of both observables with χ for most V, as well as the same behaviour as function of V we can see in figure 6.4. Of particular note is the jump in the data observed at $V = 1.6$ (and perhaps also at $V = 1.7$ in the very last data point, although it is unclear whether this is similar).

Finally, at $L_y = 8$ (figure 6.8), we see the same monotonous increase of ξ and S_E with χ as at the smaller circumferences. However, here we also see a clear distinction between the two phases, with the ICI phase having consistently higher values for both ξ and S_E than the FQH phase. We note that it is possible for data at $L_y = 6$ to show a similar distinction, if they would be obtained over a broader range of V. We believe the jump observed at $V = 1.4$ is evidence of a shift in the location of the critical point with bond dimension, as we will set out in the next section.

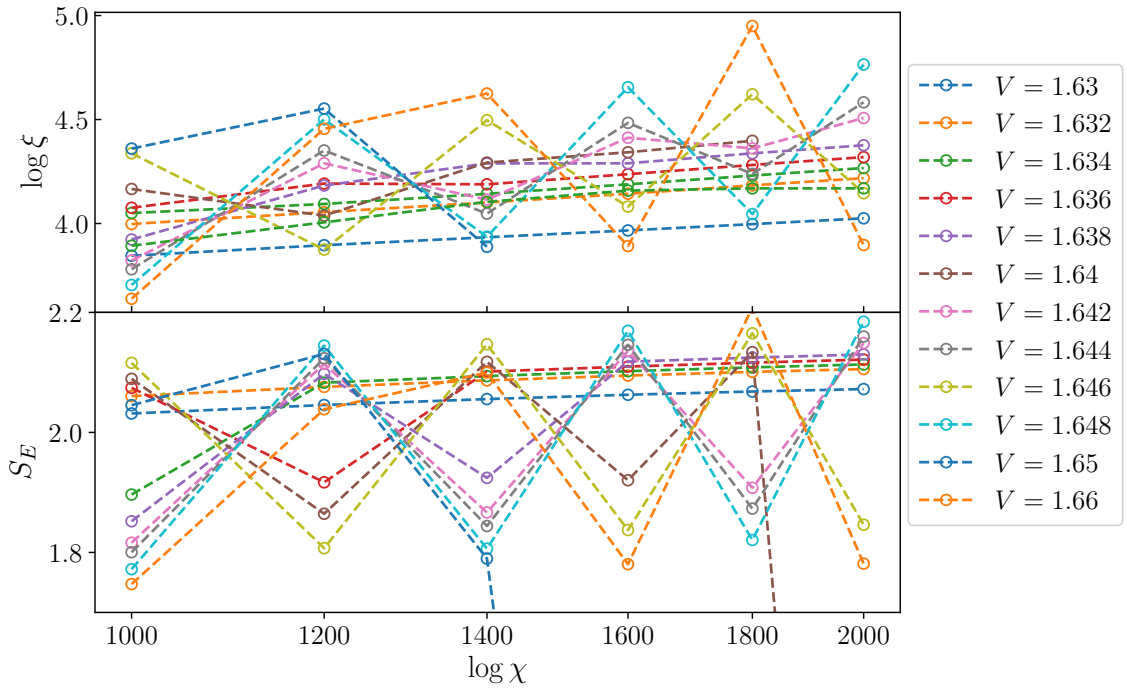

FIGURE 6.6: Correlation length (in lattice sites) $\log \xi$ (top) and entanglement entropy S_E (bottom) as function of bond dimension χ for several V near the transition at $L_y = 6$. Note that this data comes from a very narrow band of values for V.

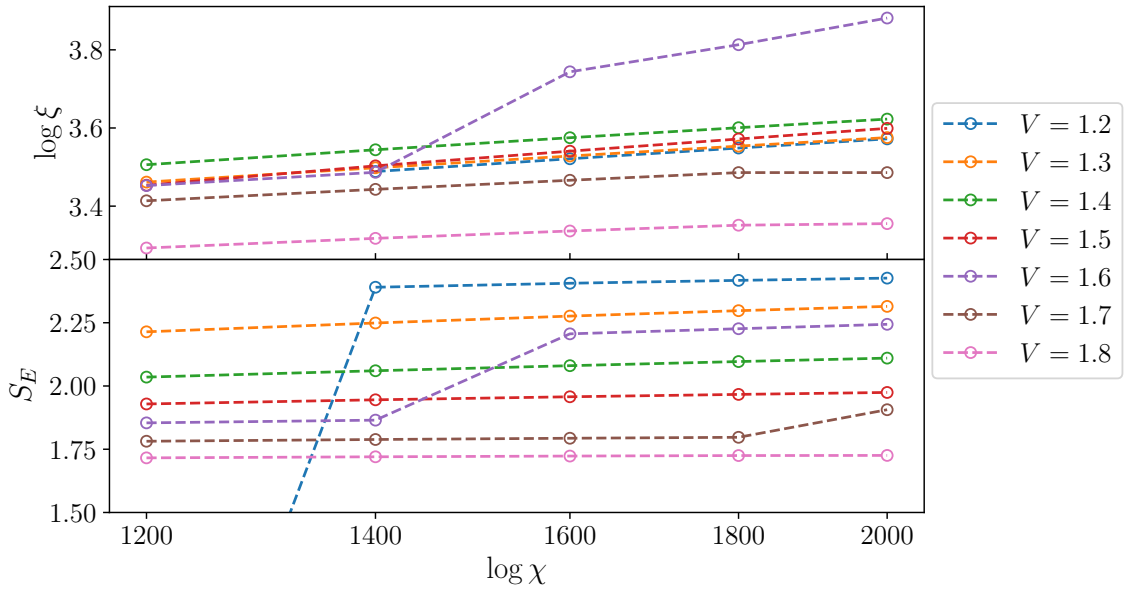

FIGURE 6.7: Correlation length (in lattice sites) $\log \xi$ (top) and entanglement entropy S_E (bottom) as function of bond dimension χ for several V near the transition at $L_y = 7$.

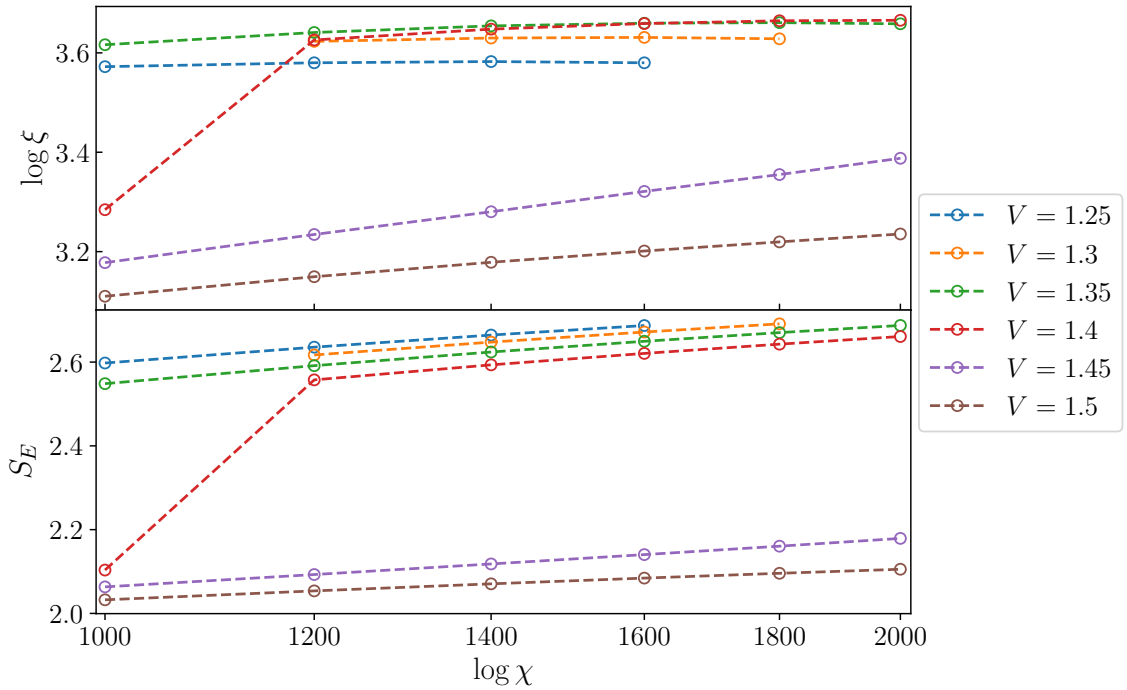

FIGURE 6.8: Correlation length (in lattice sites) $\log \xi$ (top) and entanglement entropy S_E (bottom) as function of bond dimension χ for several V near the transition at $L_y = 8$. A clear distinction between states in the fractional phase ($V > 1.4$) and states in the integer phase ($V < 1.4$) can be observed. At $V = 1.4$, we see a jump from the fractional phase at $\chi = 1000$ to the integer phase at $\chi = 1200$. This jump is explained in the text. We also observe that even at $\chi = 2000$, there is a slope in $\xi(\chi)$ for $V > 1.4$ and in $S_E(\chi)$ for all V, indicating that full convergence with χ has not yet been achieved even at this bond dimension.

6.4 Dependence of V_c on L_y and χ

The critical point for the plateau transition in the Harper-Hofstadter model at $n_\phi = 3/11$, $L_y = 6$ as described above appears to be located around $V_c = 1.64$. Figure 6.9 shows entanglement entropy data for several circumferences $4 \leq L_y \leq 10$, in an attempt to show how the transition shifts with L_y. Additionally, figure 6.10 adds data up to $\chi = 2000$ for the cases at $L_y = 6$ and $L_y = 8$, showing a further divergence of S_E with χ. We are hesitant to attach much meaning to the results for $L_y = 4$, as finite size effects could play a large role at such a small circumference. It is also clear that the bond dimensions used for $L_y = 10$ are insufficient to get an accurate representation of the states at that circumference. However, the discontinuities in figure 6.9 are pronounced enough that we can make a tentative statement on the shifting of V_c with L_y. At $L_y = 8$, we find $V_c \approx 1.4$, while at $L_y = 10$ we find $V_c \approx 1.2$, suggesting a decrease of V_c with L_y. The results in figure 6.5 corroborate a transition at $V_c \approx 1.4$. On the other hand, as we shall describe shortly, calculations at finite χ seem to yield a bias towards a lower value of V_c, which will presumably be more pronounced for larger L_y, and which could reduce the dependence of V_c on L_y as $\chi \to \infty$.

We interpret these results, especially those at $L_y = 6$, as evidence for the phase transition being continuous. Here, we again point out that due to the nature of DMRG, some ambiguity about the order of a phase transition studied using this method is likely to remain. At any fixed maximum bond dimension χ, the amount of entanglement and effective range of interactions are capped. Therefore, the correlation length ξ is effectively truncated to some finite value, even if the phase transition at $\chi \to \infty$ is continuous. While the maximum ξ will increase with χ for a continuous phase transition, one can typically not be completely certain whether an increase of χ beyond what is computationally feasible at the time of computation will continue this increase, or whether a true maximum (indicating a first-order transition) will at some point be reached. Thus, even 'truly continuous' phase transitions might appear as being first order when studied using DMRG.

Data for $L_y = 8$ gives us insight into another interesting phenomenon, namely the shift of V_c with bond dimension χ. This can be seen in figures 6.10(b) and (e), but is most clear in figure 6.8, where we show entanglement entropy S_E and correlation length $\log \xi$ as function of $1000 \leq \chi \leq 2000$ for $L_y = 8$, at several points near V_c. There is a distinct grouping between the states on either side of the transition. We see that at $\chi = 1000$, the state with $V = 1.4$ falls in the fractional phase, suggesting $V_c < 1.4$. However, for $\chi > 1000$, this state falls in the integer phase, suggesting $V_c > 1.4$. This is evidenced by the jump of the data for $V = 1.4$ in figures 6.8 and 6.14, and corroborated by the entanglement spectra shown in figure 6.11. Comparing the latter to figure 6.2, we can clearly see that the spectrum at $\chi = 1000$ resembles that of the FQH state, while at $\chi = 1200$, the spectrum looks like that of the ICI state. This implies that at $\chi = 1000$, $V_c < 1.4$, while at $\chi = 1200$, $V_c > 1.4$. We thus find a slight increase in V_c with increasing bond dimension.

A possible explanation for the scaling of $V_c(\chi)$ is found in figure 6.9, which shows that in general, the integer phase has a higher entanglement entropy than the fractional phase. Therefore, given that bond dimension puts a restriction on the maximal entanglement entropy representable by an MPS, at a finite bond dimension DMRG results might favour the lower-entanglement state, even though the interaction strength may be below the 'true' critical point, $V < V_c(\chi \to \infty)$. This shift in V_c might also explain the reversal of $\xi(\chi)$, as for any given $V < V_c$, the distance $|V - V_c|$ increases with χ, making the state 'less critical'.

These results cast some doubt on the smooth variation of results in figure 6.5. As it seems likely that numerical results near the critical point are most severely affected

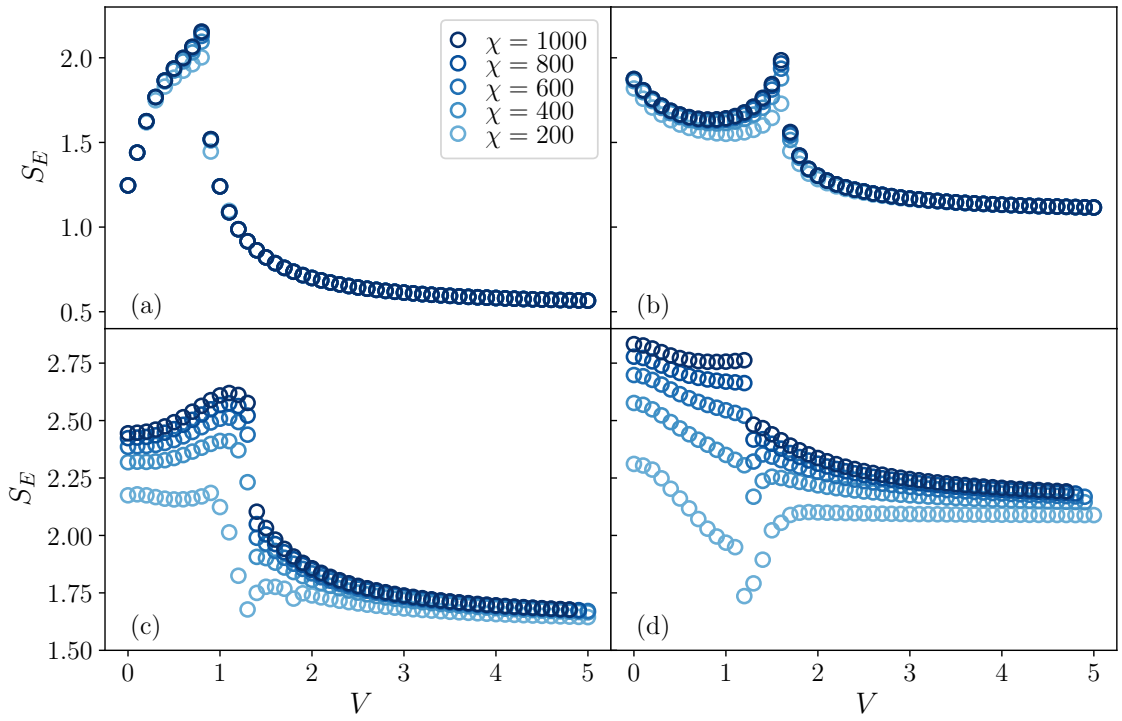

FIGURE 6.9: Entanglement entropy as function of V and χ. (a) $L_y = 4$, (b) $L_y = 6$, (c) $L_y = 8$, (d) $L_y = 10$. Results for (b) and (c) with $\chi \leq 2000$ are shown in figure 6.10.

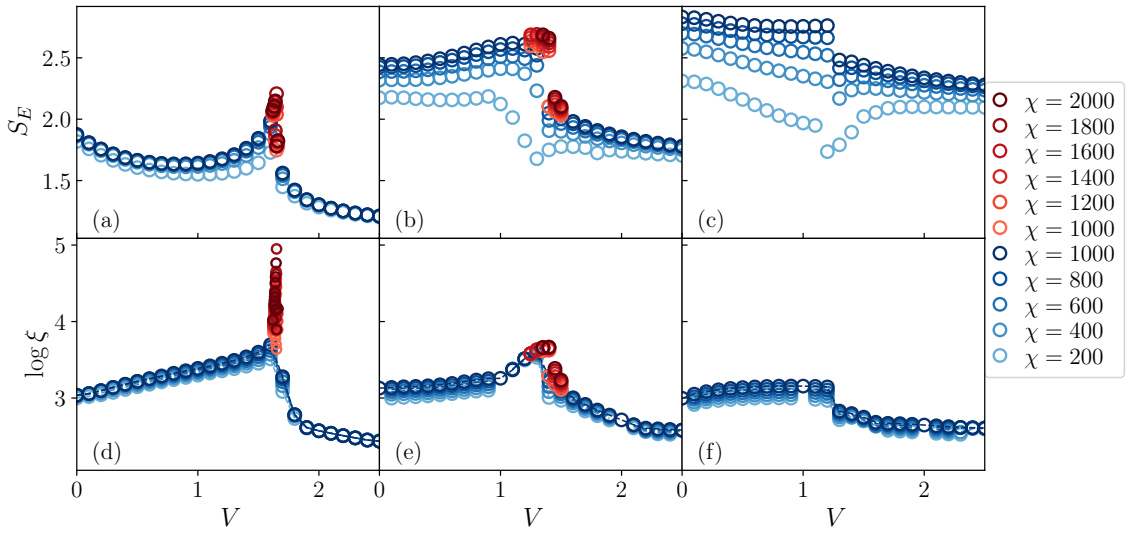

FIGURE 6.10: Entanglement entropy [(a) through (c)] and correlation length [(d) through (f), in lattice sites] as function of V and χ, with $\chi \leq 2000$ near the transition for $L_y = 6$ and $L_y = 8$. (a), (d) $L_y = 6$; (b), (e) $L_y = 8$; (c), (f) $L_y = 10$. Due to constraints on computational resources, there are no results for $\chi > 1000$ at $L_y = 10$; the data for $L_y = 10$ at $\chi \leq 1000$ are shown here for comparison. Compared to figure 6.9, we note that at higher χ, features like peaks and discontinuities become more pronounced.

by a change in bond dimension in general, and we have observed that an increase in bond dimension can shift the critical point, it is possible that we would observe sharper features if sub-figures 6.5(c) through (f) were produced at higher χ. This would, however, incur significant computational costs, because as this data is obtained through a semi-adiabatic 'sweep' through V, none of the data points can be obtained in parallel.

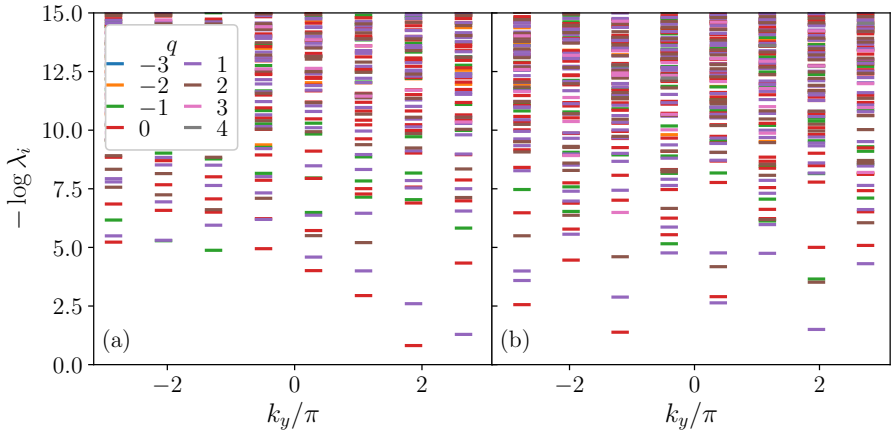

FIGURE 6.11: Momentum-resolved entanglement spectrum for $L_y = 8$, $n_\phi = 3/11$, at (a) $\chi = 1000$ and (b) $\chi = 1200$. Comparing this to figure 6.2, we clearly see that at $\chi = 1000$, the system realises the FQH state, while at $\chi = 1200$, the spectrum resembles that of the ICI state.

In contrast to the importance for S_E and ξ, increasing χ has little effect on the parts of the entanglement spectrum relevant to our analysis. This is because we are mostly concerned with the lower part of the entanglement spectrum, which represents the largest singular values in the decomposition (3.15). Because the singular values are calculated in descending order, the largest singular values–and thus the lower parts of the entanglement spectrum–are obtained at small to moderate bond dimension. Re-running calculations at a higher bond dimension only serves to improve the resolution in the higher part of the entanglement spectrum.

6.5 Central charge

To further study the plateau transition at the critical point, we extract the *central charge* c corresponding to some hypothetical conformal field theory that would describe the system at its critical point. This method is introduced in section 3.7.3.

Figure 6.12 shows the scaling of $S_E(\chi)$ with $\log \xi(\chi)$ for $L_y = 6$, at $V \approx V_c$. A line corresponding to a $c = 1$ slope is also included. We clearly see that most results, on both the integer as well as the fractional side of the transition, appear to follow the $c = 1$ scaling.

Figure 6.14 shows the scaling of $S_E(\chi)$ with $\log \xi(\chi)$ for $L_y = 8$, at $V \approx V_c$. A line corresponding to $c = 3$ scaling behaviour is also shown. Here, we see a somewhat different picture than in figure 6.12. States in the integer phase appear not to follow the scaling $S_E \sim c/6 \log \xi$. In fact, for those states, the correlation length starts to decrease with χ at some point, while S_E is still growing (which we can also observe in figure 6.8). However, results in the fractional phase appear to be consistent with a $c = 3$ conformal field theory.

We should note that we observed a similar back-bending behaviour of $\xi(\chi)$ at some points away from the transition in the $L_y = 6$ case as well. This disappeared, however, when we forced the iDMRG to extend the left- and right environments (see figure 3.15;

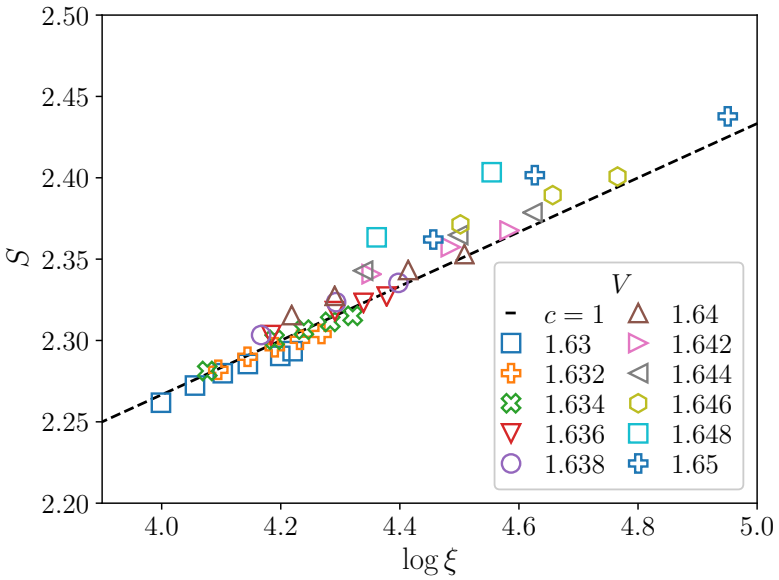

FIGURE 6.12: Entanglement entropy S_E versus correlation length $\log \xi$ for various V, on an $L_y = 6$ cylinder at $1000 \leq \chi \leq 2000$. Both S_E and ξ scale monotonically with bond dimension. The dashed black line denotes a scaling $S_E(\chi) \sim 1/6 \log \xi(\chi)$, i.e., $c = 1$. We can see that states near the plateau transition seem to follow a $c = 1$ scaling. This is most clear in the lower values of V shown here.

it is only when the true edges of the system have been 'pushed away' far enough that the active MPS unit cell represents the infinite system) using a fixed MPS unit cell. This scaling of $\xi(\chi)$ can be understood by realising that when the DMRG algorithm converges (which is a condition based on energy and entanglement entropy), the 'true' edges of the system can still be so close to the 'active' MPS unit cell as to invalidate the assumption that the MPS represents an infinite system. This results in an effective truncation of the correlation length. This effect is especially strong at criticality, where ξ is (normally) largest. By repeatedly pushing out the boundaries, the active MPS unit cell becomes a better representation of the infinite system. We attempted a similar solution at $L_y = 8$, but were unable to fully eliminate the effect within the available computational resources.

Due to the results for $L_y = 7$ not indicating a sharp transition, it is difficult to pinpoint where, if anywhere, finite entanglement should yield a clear picture of a central charge. We therefore show the scaling of S_E with $\log \xi$ for a range of V in figure 6.13. We observe that for $V \geq 1.5$, scaling is consistent with a central charge $c = 2$. For smaller V, however, slopes of $S_E(\chi) \sim (c/6) \log \xi(\chi)$ are either much steeper, or variable. Under insertion of $\phi_{\text{ext}} = \pi$ external flux through the cylinder, the results for low V changed considerably, but all states at $V \geq 1.5$ still demonstrated scaling consistent with $c = 2$. We therefore tentatively put the central charge of a critical theory at $L_y = 7$ at $c = 2$, but emphasise that our data is not sufficiently clear to be able to form strong conclusions. An overview of the three central charges we extract can be found in figure 6.16.

To further solidify our understanding of these central charges, we show the simultaneous scaling of ξ and S_E as function of V in figure 6.15. We observe markedly different behaviour for each circumference. At $L_y = 6$, we find the same 'jumping' behaviour we noted in figure 6.6. Nonetheless, we see that, at least for a subset of values, the scaling $S_E(V) \sim (c/6) \log \xi(V)$ is consistent with a central charge $c = 1$, just like we found in the finite entanglement scaling above. At $L_y = 7$, we note that the simultaneous scaling with χ yields results consistent with $c = 2$, but that no such scaling is found as function

of V. Finally, at $L_y = 8$, we observe results consistent with a $c = 3$ central charge, when scaling with both χ and V.

Unfortunately, obtaining results for larger circumferences becomes exponentially more difficult, and problems with DMRG convergence limit us from including results for higher L_y. Although we therefore emphasize that we cannot make very firm statements about the critical point, we point out that our results suggest variability of c as a function of L_y. This would be compatible with a description of the critical point in terms of a highly entangled Fermi surface (Geraedts et al., 2016), as will be discussed further in section 6.6.

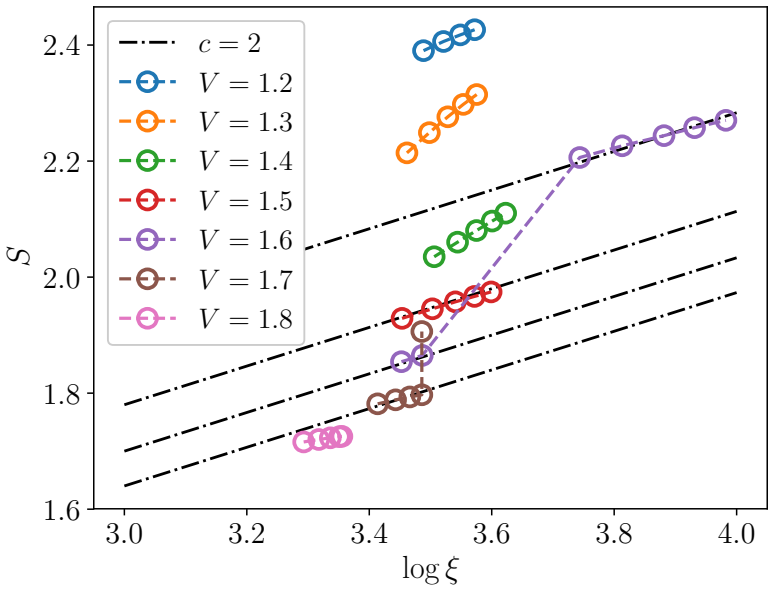

FIGURE 6.13: Entanglement entropy S_E versus correlation length $\log \xi$ for various V, on an $L_y = 7$ cylinder at $1200 \leq \chi \leq 2000$. The dot-dashed black line denotes a scaling $S_E(\chi) \sim 2/6 \log \xi(\chi)$, i.e., $c = 2$. States with $V \geq 1.5$ appear to follow this scaling. States at other values of V show either steeper slopes, or non-linear behaviour. At $V = 1.6$ and $V = 1.7$, we observe a jump between two regimes (also visible in figure 6.4). It is unclear what causes this jump, as it is unlikely that this is caused by a shift in V_c, as we see in the $L_y = 8$ results in figure 6.14. Recalculation of these results with $\phi_{\text{ext}} = \pi$ external flux inserted into the cylinder (not shown) yielded $c = 2$ scaling for $V \geq 1.5$ (consistent with the results here), and very different results for smaller V. For $V = 1.6$, results up to $\chi = 2400$ have been included, in order to confirm that the jump in the data does not change the $c = 2$ scaling.

6.6 Towards a theory for the plateau transition

Given our data supporting a direct QH plateau transition between an ICI state and an FCI state in the Harper-Hofstadter model, at least at $L_y = 6$, we will examine several theoretical scenarios for a possible continuous transition and discuss relevant effective field theory descriptions for our critical point. We initially focus on the observed transition between a $C = +4$ ICI and a $\nu = 1/3$ Laughlin-like state at $n_\phi = 3/11$, as our data is most convincing for this case.

Several works have considered flux-attachment transitions between different QH states in CF models (Wen and Wu, 1993; Chen, Fisher, and Wu, 1993; Ye and Sachdev, 1998;

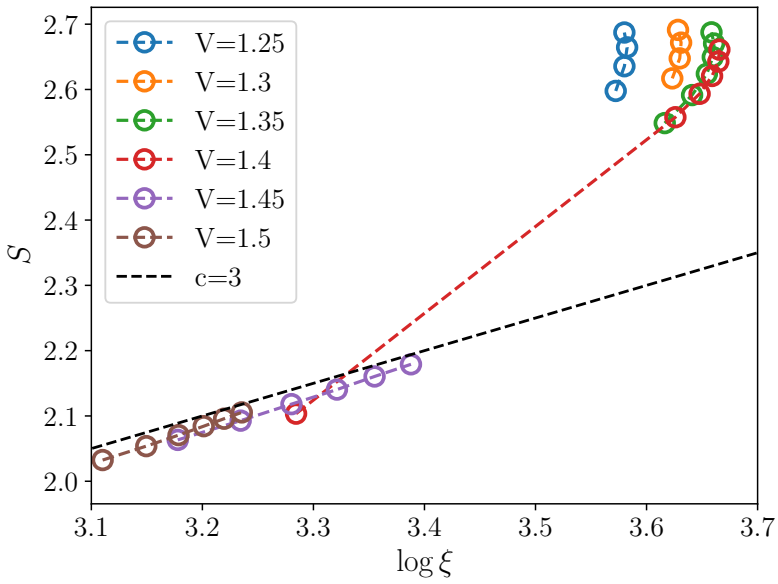

FIGURE 6.14: Entanglement entropy S_E versus correlation length $\log \xi$ for various V, on an $L_y = 8$ cylinder at $1000 \leq \chi \leq 2000$. The dashed black line denotes a scaling $S_E(\chi) \sim 3/6 \log \xi(\chi)$, i.e., $c = 3$. These results paint a somewhat different picture than those in figure 6.12). States in the integer phase appear not to follow the scaling $S_E \sim c/6 \log \xi$. In fact, for those states, the correlation length starts to decrease with χ at some point, while S_E is still growing (see also figure 6.8. Results in the fractional phase are strongly consistent with a $c = 3$ conformal field theory. The jump in the data for $V = 1.4$ can again be ascribed to the shift in V_c with χ described in section 6.4.

Grover and Vishwanath, 2013; Barkeshli and McGreevy, 2014; Barkeshli, Yao, and Laumann, 2015; Lee et al., 2018; Ma and He, 2020). Transitions between a superconductor and a $\nu = 1/2$ Laughlin state (Barkeshli and McGreevy, 2014) and between different states in the same Jain series (Lee et al., 2018)[7] seem most similar to our current setting.

Barkeshli and McGreevy (2014) model the Laughlin state with two fermionic partons filling bands of Chern number $C = +1$. The topologically trivial superconducting phase arises if one of these bands experiences a topological transition to Chern number $C = -1$, with the other band remaining at $C = +1$. This requires a simultaneous gap-closing at two Dirac points, ensured by a translational symmetry. In the absence of this symmetry, the transition splits into two transitions, separated by a Mott insulator phase. Crucially, only a single parton field is affected by the transition.

Similarly, the critical points discussed in Lee et al. (2018) can be understood as a Chern number changing transition. Here, a fermionic CF theory is used, and the relevant parton field describes the effective band structure experienced by the CFs. Again, transitions are explained by the closing of a gap at multiple Dirac points with corresponding change in the CF band's Chern number C^*. The simultaneous closing closing of the gap at several Dirac points is enforced by magnetic translation symmetry, supporting changes of C^* by $\Delta C^* > 1$. However, the parton fields describing flux attachment remain unaffected at the transition. Thus, in both these scenarios (Barkeshli and McGreevy, 2014; Lee et al., 2018),

[7] The theory by Lee et al. (2018) was extended to Abelian states in *different* Jain series and non-Abelian states by Ma and He (2020). The latter work acknowledges that the theory it sets out is unable to capture the phase transition described in this chapter. We will nonetheless briefly cover its applicability to our results.

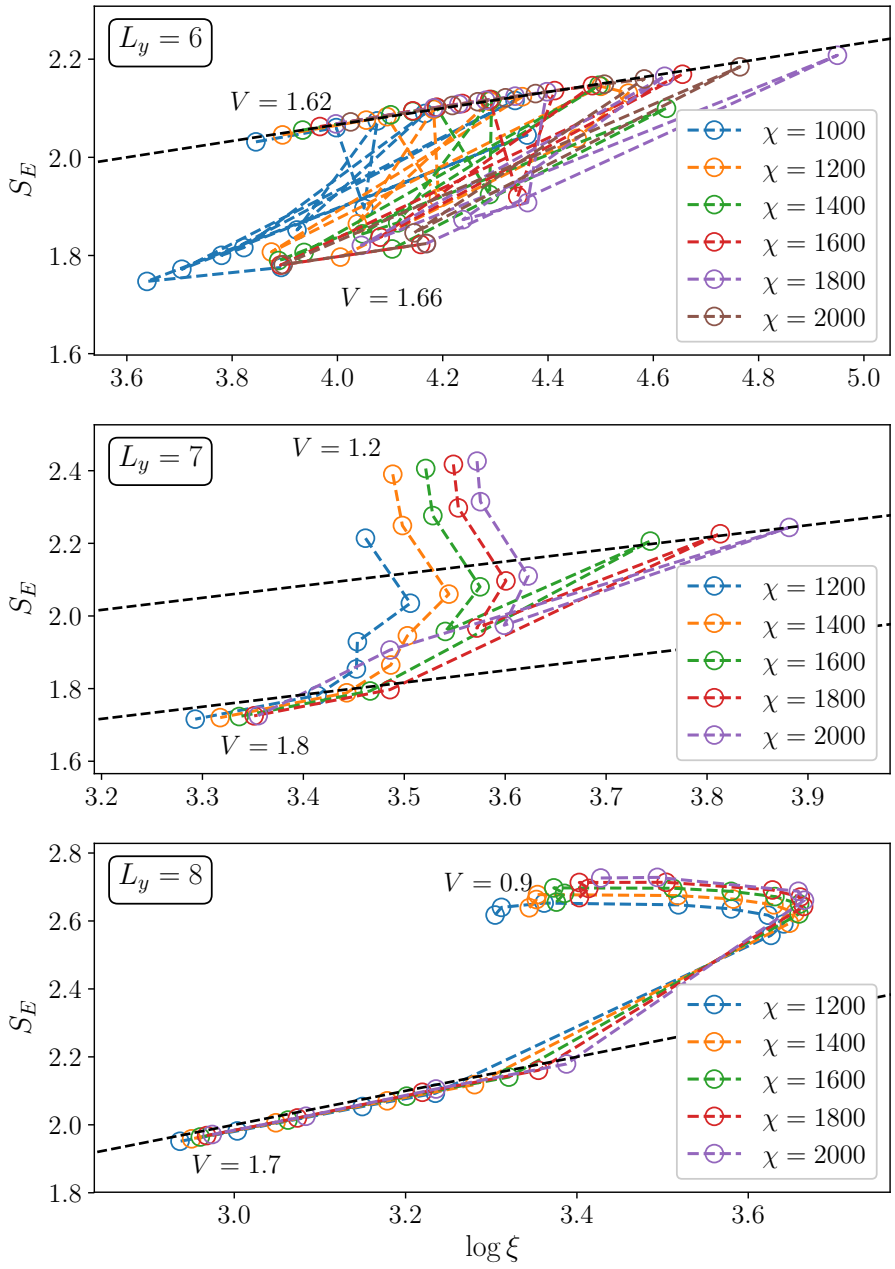

FIGURE 6.15: Simultaneous scaling of $\log \xi$ and S_E with interaction strength V, for various bond dimensions χ, at $L_y = 6, 7$ and 8 (top to bottom). The lowest and highest value of V have been marked to indicate the 'direction' of the graphs. We note that the picture for $L_y = 6$ is muddled by the same 'jumping' observed in figure 6.6, and that no clear scaling behaviour is evident in the results for $L_y = 7$. Dashed black lines indicate a scaling of $S_E(V) \sim (c/6) \log \xi(V)$, with $c = 1, 2, 3$ at $L_y = 6, 7, 8$ respectively. We thus see that the scaling observed in figures 6.12 and 6.14 reappears.

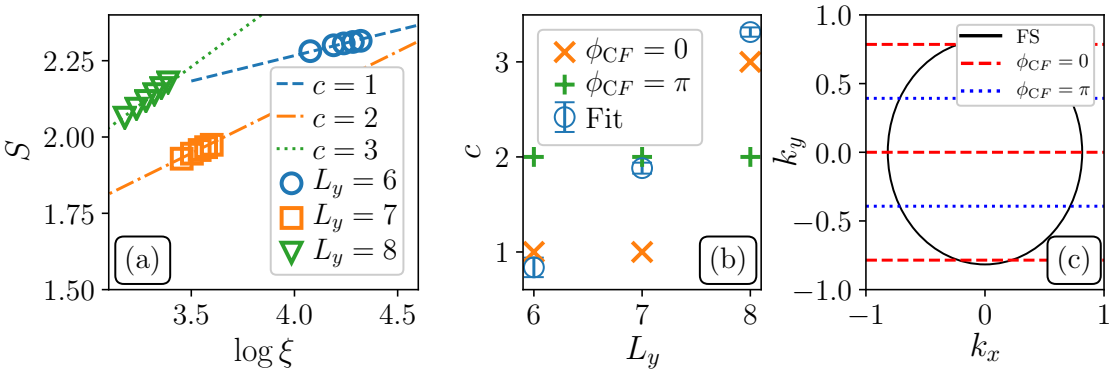

FIGURE 6.16: Combining the central charge scaling for $L_y = 6, 7$ and 8. (a) Scaling of S_E and ξ with $1000 \leq \chi \leq 2000$ for $L_y = 6$ (blue circles), $L_y = 7$ (orange squares) and $L_y = 8$ (green triangles), at $V = 1.634, 1.5, 1.45$ respectively, and expected linear scaling for $c = 1$, 2 and 3, respectively. Dashed black lines denote linear fits. (b) $c(L_y)$, as inferred from linear fits to the data (blue circles) and predicted for CF Fermi surface with $\phi_{\text{CF}} = 0$ (orange crosses) and $\phi_{\text{CF}} = \pi$ (green pluses). Error bars denote one standard deviation σ. (c) View of a putative Fermi surface for $L_y = 8$, showing intersections with three (two) lines of allowed k_y momentum for $\phi_{\text{CF}} = 0\,(\pi)$.

the critical theory is given by Dirac points carrying a fixed central charge, and at most one parton field is affected by the transition.

In our work, the description of the ICI phase does not require a parton construction. Rather, states in this phase can be described by (regular) fermions in the lowest Harper-Hofstadter sub-band with Chern number $C_1 = 4$. In contrast to this, the description of the FCI phase requires three parton fields. Two of these parton fields experience $C = 1$ Chern bands to effectuate flux attachment, while the third parton field describes the effective physics of the CFs, which is also a $C = 1$ Chern band for the $\nu = 1/3$ Laughlin state. Thus, at the transition from ICI to Laughlin state, two changes occur, which at least in our data at $L_y = 6$ appear to occur simultaneously. Firstly, the change of the CF band Chern number, and secondly the fractionalisation of particles into three partons to give rise to the two additional fields. Hence, to describe the transition, one would have to explain why these changes occur simultaneously rather than independently. While there may exist effective theories in which this type of fractionalisation must occur at once, a more generic case might display a sequence of several transitions affecting individual parton fields.

Furthermore, our numerics indicate that the central charge at the critical point varies with cylinder circumference (section 6.5). While a transition described by multiple Dirac points could explain the magnitude of the central charges we observe, this scaling with L_y does not fit with that picture. A single transition would thus require a more exotic explanation, such as the emergence of a 2D Fermi surface at the critical point (Geraedts et al., 2016; Gong et al., 2019).

Following the calculations in Geraedts et al. (2016), at $\nu = 1/3$ we find $k_F \ell_B = \sqrt{2/3}$. Given the infinite cylinder geometry, k_x is essentially unconstrained, but k_y can only take on a few discrete values:

$$k_y = \frac{2\pi}{L_y}(n + a), \quad n \in \mathbb{Z}, \tag{6.6}$$

where the CF boundary conditions determine whether $a = 0$ (for periodic boundary conditions) or $a = 1/2$ (for anti-periodic boundary conditions). The discrete k_y-values

create 'wires' running through the Fermi surface, with the number of wires N_w equal to the central charge c if the model is described by a Fermi liquid. At $L_y = 6$, we find $N_w = 1$ with $a = 0$, or $N_w = 3$ with $a = 1/2$. At $L_y = 7$, we find $N_w = 1$ with $a = 0$, or $N_w = 2$ with $a = 1/2$. At $L_y = 8$, we find $N_w = 3$ with $a = 0$, or $N_w = 2$ with $a = 1/2$. Comparing this to our central charges, which are $c = 1, 2, 3$ for $L_y = 6, 7, 8$, respectively, we see that our results would be consistent with an Fermi surface description if $a = 0$ for $L_y = 6, 8$, and $a = 1/2$ for $L_y = 7$. An illustration of the central charges we extract from the data, compared to the values predicted by (6.6), as well as an illustration of the 'wires' crossing a circular Fermi surface, is shown in figure 6.16. However, it is unclear whether the CFs actually experience the required boundary conditions for this analysis to work out, nor what type of particle would experience the suggested Fermi surface. Furthermore, our results for $L_y = 7$ have suggested that the bond dimensions used to obtain these results were insufficient. Thus, we are careful to not interpret these results as definitive.

The construction of theories for the interaction-driven integer-to-fractional CI plateau transition forms an exciting field of future study. A general theory would potentially predict not only the transition we have studied so far, but also transitions into different FQH states. For example, the next section describes a similar transition into a $\nu = 2/5$ state.

6.7 Plateau transition into a $\nu = 2/5$ state

A natural extension to the plateau transition described in section 6.2 is the question whether similar transitions can be found into higher hierarchy states (see section 2.3.2). In this section, we will be describing precisely such a transition into the $\nu = 2/5$ state, the state following $\nu = 1/3$ in the FQH hierarchy (2.26). Following the calculations in section 6.1, we require $r = 2$, $k = 2$ in (6.1) for the fractional state to occur in the LLL tail. This implies that a flux density $n_\phi = p/q$ with $p = 5$ and q, again, an essentially free parameter, combined with a particle density $n = 2/q$ should give the correct filling fraction:

$$\nu = \frac{n}{n_\phi} = \frac{2/q}{5/q} = \frac{2}{5}. \tag{6.7}$$

We again choose q such that it is small enough to make MPS simulations feasible, while not so small that the fractional state is destabilised. In the following, we will consider $q = 16$ as our example. Figure 6.17 shows our results for the transition in this case.

The fractional state in the LLL tail is now in competition with an ICI state supported by the lowest 2 sub-bands (in contrast to the state only existing in a single sub-band, as in the discussion on $\nu = 1/3$). Following section 4.3 (in particular section 4.3.1), we can derive Chern numbers for the ICI state at $q = 16$ by adding the sum of the Chern numbers for the lowest sub-bands:

$$q = 16: \quad C_1 = -3, C_2 = -3 \quad \Rightarrow C_{\text{ICI}} = -6 \tag{6.8}$$

This would imply that we will find a Hall conductivity of $\sigma_H = -6$ in the ICI phase. Indeed, at low interactions, we obtain a transport of -18 charge quanta upon insertion of $3 \times 2\pi$ external flux, yielding $\sigma_H = -6$, as can be seen in figure 6.17(g). Conversely, at high V, we find a charge transport of $6/5$ under the same flux insertion, which is consistent with $\sigma_H = 2/5$, and thus consistent with a $\nu = 2/5$ state. However, unlike the $\nu = 1/3$ results described in section 6.2, we here observe a fairly stable intermediate plateau, with 6 charge quanta being transported indicating $\sigma_H = 2$.

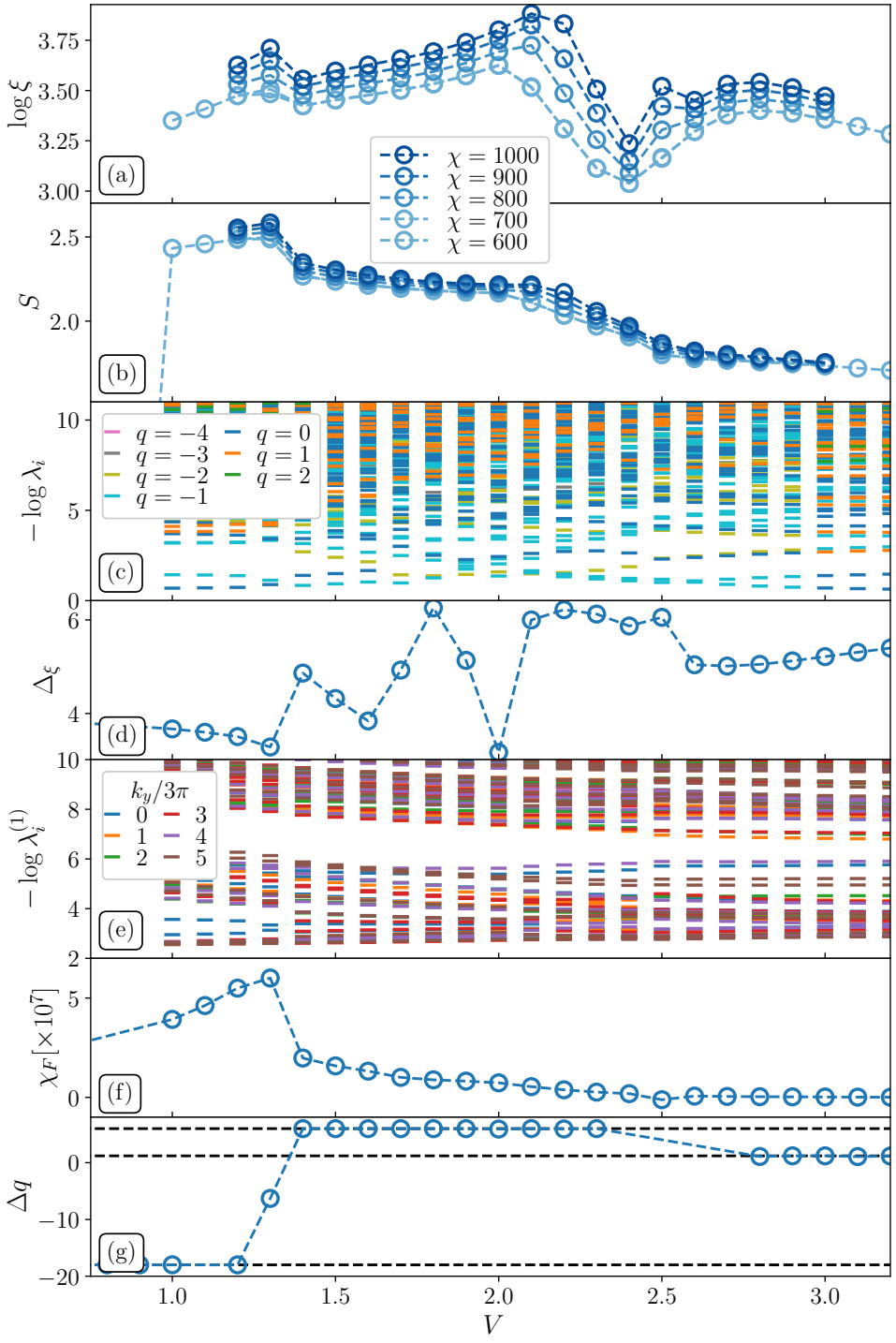

FIGURE 6.17: Transition from an ICI state into the $\nu = 2/5$ state at $L_y = 6$. Shown are: (a) Correlation length (the circumference $\log L_y \approx 1.79$ falls below the range shown) and (b) entanglement entropy for several values of the bond dimension $600 \leq \chi \leq 1000$ (c) entanglement spectrum (colours denote different quantum number sectors). (d) Entanglement gap. (e) Spectrum of the single-particle density matrix. (f) Fidelity susceptibility χ_F. (g) Transported charge under the insertion of $3 \times 2\pi$ external flux. Horizontal lines denote $\Delta q = -18$, $\Delta q = 6/5$ and $\Delta q = 6$ (corresponding to $\sigma_H = -6$, $\sigma_H = 2$ and $\sigma_H = 2/5$, respectively). For $2.4 \leq V \leq 2.7$, data is missing due to bad DMRG convergence. Subfigures (c) through (f) have $\chi = 600$, (g) has $\chi = 500$.

The other results in figure 6.17 also paint a more complicated picture that we obtained for the $\nu = 1/3$ transition. In particular, the entanglement entropy [figure 6.17(b)], entanglement spectrum [figure 6.17(c)] and spectrum of the single-particle density matrix [figure 6.17(e)] show much less obvious discontinuities.

Nonetheless, there does seem to be a phase transition indicated by these results. The correlation length [figure 6.17(a)] exhibits several (minor) discontinuities or features as function of V, as well as regions of significant scaling with χ. The entanglement entropy [figure 6.17(b)] appears to show three distinct regimes with different slopes of $S_E(V)$ (at $V \leq 1.3$, $1.4 \leq V \leq 2$ and $V \geq 2.5$), separated by either (weak) discontinuities, or intervals of stronger scaling of S_E with χ (mainly at $2.1 \leq V \leq 1.9$). Transitions between these regimes line up with the features in ξ.

The entanglement spectrum [figure 6.17(c)] exhibits some level crossings in the lower states at $1.3 \leq V \leq 2.5$. While it is difficult to line up any features within this interval, the onset and end point of the interval do match with the features discussed above. Due to the several level crossings involving the lowest entanglement level, which cause the entanglement gap [figure 6.17(d)] to be calculated within different momentum and charge sectors, the entanglement gap varies rather wildly. We can however still distinguish the regimes at $V \leq 1.3$ and $V \geq 2.6$ from the intermediate regime. The spectrum of the single-particle density matrix [figure 6.17(e)], while hard to interpret and not displaying major features, does appear to show a discontinuous change between $V = 1.3$ and $V = 1.4$, and a stable state for all $V \geq 2.5$. The same points can be seen in the fidelity susceptibility χ_F [figure 6.17(f)], with a sharp feature at $V = 1.3$ and a minor change of slope at $V = 2.5$, followed by $\chi_F \approx 1$ for all $V \geq 2.5$ (indicating that these states are essentially identical).

All these results are consistent with the aforementioned intermediate phase, identified in the flux insertion results and the fidelity susceptibility χ_F [figure 6.17(g)]. We tentatively put the location of this intermediate phase at $1.3 \lessapprox V \lessapprox 2.5$, although further research is needed to locate it more precisely, and to study the persistence of this phase at different L_y. Additionally, further research is needed to identify the nature of the intermediate phase, for which we do not yet have a (heuristic or formal) description.

6.8 Discussion

We have shown strong numerical evidence for the existence of a direct phase transition between an ICI state in a $|C| > 1$ band, and an FCI (or FQH) state, showing characteristics of the $\nu = 1/3$ Laughlin state in the $C = 1$ LLL tail of the fermionic Harper-Hofstadter model. At $L_y = 6$, the transition appears sharply direct, strongly suggesting the absence of an intermediate phase. While at $L_y = 7$ and $L_y = 8$ our data is less clear and exhibits fewer indications of a sharp transition, it is still consistent with a phase transition. This phase transition is not captured by any presently known theory. Our evidence for the phase transition includes the correlation length, entanglement entropy, entanglement spectrum, entanglement gap, the spectrum of the single-particle density matrix, fidelity susceptibility and Hall conductivity, all of which show distinct discontinuities at the critical point. We have shown that the critical point, identified numerically using DMRG, can shift with bond dimension, due to the integer phase having higher entanglement than the fractional phase. We have also studied the central charge associated with the critical point. Additionally, we have shown that a similar transition exists into the $\nu = 2/5$ hierarchy state, with some as yet unidentified intermediate phase occurring between the ICI state and the $\nu = 2/5$ state.

As stated, the construction of a theory that would be able to capture the phase transitions described in this chapter forms an exciting field of future study. The methods used here can also be used to look for phase transitions in additional cases. These cases include further states in the hierarchy (2.26), which form an immediate generalisation of the work in this chapter, as well as more exotic FQH or FCI states.

A perhaps more exciting and definitely more challenging avenue is to look for transitions between two distinct fractional phases. Andrews and Möller (2018) have described FCI states in single $|C| > 1$ Harper-Hofstadter bands (focusing on the lowest sub-band below the relevant single-particle gap in cases with $n_\phi = p/q$, with $p > 1$ sub-bands in the LLL) at

$$n_\phi = \frac{p}{q} = \frac{p}{|C|\, p - \mathrm{sgn}(C)}. \tag{6.9}$$

One could realise such an FCI state at flux densities with $p \geq 2$, such that this state (supported by the lowest sub-band) competes with an FQH state in the LLL (which consists of p sub-bands). At the corresponding flux density $n_\phi = p/q$, each Harper-Hofstadter sub-band has a density of states $n_s = 1/q$.

Thus, for example, one could realise an FCI state in a single $C = -2$ band, with filling fraction $\nu_1 = 2/3$ or $\nu_1 = 4/5$. These are particle-hole conjugate filling fractions to the $\nu = 1/3$ and $\nu = 1/5$ described in Andrews and Möller (2018). The existence of these conjugate states is, at present, an assumption. These states would be supported by a single Harper-Hofstadter band with $n_s^{(1)} = 1/q$, where the superscript (1) denotes that this holds for a single band. Then, the particle density required to realise the $\nu_1 = 2/3$ ($\nu_1 = 4/5$) state would be $n = \nu_1 n_s = 2/3q$ ($n = 4/5q$).

Since the value of p is not determined by ν or C, we can now choose to create this state at $p = 2$, where the flux density is $n_\phi = 2/q$. Here, the LLL is a $C = +1$ structure consisting of two sub-bands, and thus has a combined density of states $n_s^{(2)} = 2/q$, where the superscript (2) denotes that this is the density of states on two sub-bands. Thus, as $\nu_{\mathrm{LLL}} = n/n_s^{(2)}$, the particle and flux density at that point are also commensurate with a $\nu_{\mathrm{LLL}} = (2/3q)/(2/q) = 1/3$ state (if we started at $\nu_1 = 2/3$ in the lowest sub-band) or a $\nu_{\mathrm{LLL}} = (4/5q)/(2/q) = 2/5$ state (if we started at $\nu_1 = 4/5$) on the LLL. Thus, one could investigate whether a phase transition such as those studied in this chapter, occurs between the sub-band $\nu_1 = 2/3$ ($\nu_1 = 4/5$) FCI state at small V, and the $\nu_{\mathrm{LLL}} = 1/3$ ($\nu_{\mathrm{LLL}} = 2/5$) LLL FQH state at larger V. Such a phase transition would necessarily change the Chern number of the band supporting the state, as the lowest sub-band always has $|C| > 1$, while the LLL always has $C = +1$.

Unfortunately, for a flux density (6.9) small enough to stabilise the FQH state (in the fermionic case) on the LLL tail would most likely require $|C| \geq 3$ at least. Andrews and Möller (2018) were unable to get fermionic results for $|C| \geq 3$ using exact diagonalisation due to finite-size effects. Thus, some improvement of the method (or more computing power) is needed to simulate systems large enough to potentially observe these transitions.

Finally, one could study transitions in the bosonic Harper-Hofstadter model similar to those described here. Due to the existence of Bose-Einstein condensates in the bosonic model, such transitions would most likely be from a condensate into various QH states.

Chapter 7

Conclusions and outlook

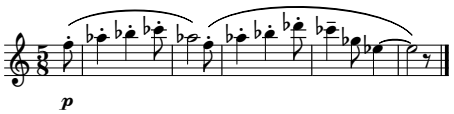

Leonard Bernstein, *Sonata for Clarinet and Piano*

In this thesis, we have studied quantum Hall (QH) states in the Harper-Hofstadter model from several angles, using methods based on Matrix Product States (MPSs) and the the Density Matrix Renormalization Group (DMRG). The quantum Hall effect (QHE) arises when charged particles are confined to move in two dimensions, subject to a magnetic field. The fractional quantum Hall effect (FQHE) in particular forms a prime example of the appearance of topological order in physics, and the study of transitions between QH states has proved a fertile field of research. The Harper-Hofstadter model describes particles on a two-dimensional lattice, subject to uniform magnetic flux piercing the lattice. This model has been shown to support both integer and fractional QH and Chern insulator (CI) states. The band structure of the Harper-Hofstadter model, or *Hofstadter butterfly*, is self-similar and exhibits a 'tail' which can be adiabatically connected to the lowest Landau level (LLL). This tail consists of a number of *magnetic sub-bands* p, which depends on the flux density $n_\phi = p/q$, leading to the splitting of the LLL into several sub-bands when $p > 1$.

We use MPSs and DMRG to study QH states in the Harper-Hofstadter model, as these methods have proven successful for similar problems in the past, and provide us with significant access to the microscopic properties of the states. We have studied QH states in the Harper-Hofstadter model using observables extracted from the MPSs, including the entanglement entropy S_E (including the *topological entanglement entropy* S_{topo}), correlation length ξ, density and density-density correlation functions, momentum-resolved entanglement spectra, entanglement gaps, spectra of the single-particle density matrix ρ_{ij} and fidelity susceptibility χ_F. Additionally, we have made heavy use of flux insertion procedures (Laughlin, 1981) to directly observe the Hall response σ_H to a semi-adiabatic change in external flux.

The existence and stability of fractional quantum Hall (FQH) states in the LLL tail of the Harper-Hofstadter model, at $n_\phi = p/q$ with $p > 1$, i.e., where the tail consists of multiple magnetic sub-bands, has often been implicitly or explicitly assumed in the literature. However, little systematic study has been undertaken to confirm the validity of this assumption. In chapter 5, therefore, we extensively studied whether FQH states exist on the LLL tail of the Harper-Hofstadter model at $p > 1$. This work also provides the basis for our investigation into novel phase transitions in chapter 6. While we put most emphasis on the fermionic model, we demonstrate the stability of a $\nu = 1/2$ bosonic Laughlin-like

state on a range of n_ϕ with $1 \leq p \leq 4$, thereby essentially providing benchmark results for our work with fermions.

For the fermionic model, we have studied both the $\nu = 1/3$ Laughlin state, as well as the next state in the FQH hierarchy at $\nu = 2/5$. We found strong evidence for the existence of the $\nu = 1/3$ state on the Harper-Hofstadter model's LLL tail consisting of multiple sub-bands, where our numerical results agreed with theoretical predictions for the Hall conductivity σ_H (obtained through flux insertion), entanglement spectra (through the existence of a chiral tail, and the partition counting of semi-degenerate levels within a quantum number sector in this tail), density profiles, correlation functions and extrapolated values for S_{topo}.

For the $\nu = 2/5$ case, we again found good agreement between most of our results and theoretical predictions for σ_H and S_{topo}, albeit with the occasional outlier. In particular, states with small circumferences L_y in terms of ℓ_B tended to line up less well with theoretical predictions. Matching momentum-resolved entanglement spectra, while consistent with each other, to results from the literature is more difficult due to an absence of clear predictions therein. We note here that Andrews, Mohan, and Neupert (2020) extended the search for FQH states on multiple sub-band LLLs to both $\nu = 2/5$ as well as $\nu = 3/7$, using methods building on our work in Schoonderwoerd, Pollmann, and Möller (2019). For the $\nu = 2/5$ state, there is good agreement between our work and the results in Andrews, Mohan, and Neupert (2020). However, as this work uses a DMRG implementation closely related to ours (Hauschild and Pollmann, 2018), the agreement between these results and ours should not be taken as conclusive evidence. A replication of these results using different methods, such as exact diagonalisation, or at least an independent implementation of DMRG, could thus offer valuable confirmation of our results.

A second important result from chapter 5 is the improved numerical method for extrapolating the topological entanglement entropy S_{topo}. Because, as we have shown, the same FQH states can be found for several values of n_ϕ, one can combine calculations for these states. When graphed as function of L_y in units of the magnetic length ℓ_B, the entanglement entropy S_E of these states tends to collapse onto a uniform relation between S_E and L_y, which can then be used to extrapolate to S_{topo} at $L_y = 0$. Because this allows us to combine results for many $L_y[\ell_B]$ while keeping L_y manageably small in terms of lattice sites, we obtain a large improvement in the accuracy of this extrapolation, which is now based on many more data points than if results for a single n_ϕ had been used, at a relatively small increase in computational cost. While this development does not provide new physical insight, we believe it is an important technical improvement. This is partially evidenced by the fact that our method has, since its appearance in Schoonderwoerd, Pollmann, and Möller (2019), already found application in other works (Andrews and Soluyanov, 2020; Andrews, Mohan, and Neupert, 2020).

Chapter 6 contains our most important results. In this chapter, we continue a long tradition of the study of QH phase transitions, to study phase transitions between integer Chern insulator (ICI) and FQH states. The transitions we find appear to be novel, i.e., we have not found an existing theory able to predict these phase transitions. Our investigation was centred on FQH states supported on the LLL Harper-Hofstadter tail with $p > 1$. Specifically, we studied competition between an ICI state supported on a subset of the magnetic sub-bands forming the LLL and an FQH state supported by the entire LLL. We found that both states can be realised at fixed n_ϕ, depending on the value of the interaction strength V, with the ICI state being favoured at low V, and the FQH state being favoured at high V. We studied the transition between these states using the entanglement entropy, correlation length, momentum-resolved entanglement spectra, entanglement gaps, spectra of the single-particle density matrix ρ_{ij}, fidelity susceptibility

χ_F and Hall response σ_H.

At $n_\phi = 3/11$, we found a transition between a $C = +4$ ICI and the $\nu = 1/3$ Laughlin state. This transition appears most clearly at a circumference $L_y = 6$, where our numerics indicate that the transition is direct. At $L_y = 7$, sharp indications of a transition are much harder to discern, and there seems to be some indication of an intermediate phase between the ICI and Laughlin states. At $L_y = 8$, we again observe sharp features indicating a transition in some observables, but not in all. However, as the systems with larger circumference carry more entanglement, they are less well captured by DMRG at a given bond dimension. It could be that this, rather than a physical reason, is why we observe smooth features. Therefore, it is difficult to draw final conclusions from our numerical results at this stage. Nonetheless, our data is obtained at state-of-the-art bond dimensions, which strengthens our confidence; it seems highly unlikely for this data to be wholly negated by yet-unattainable results at even larger χ. While the nature of numerical studies means that physical conclusions are inextricably linked to data quality and numerical limitations, we believe that our data is sufficiently clear for our results to be valuable, and that they provide a solid basis for future theoretical developments.

We have extracted the central charge corresponding to a putative field theory describing the system at criticality from $S_E(\chi)$ and $\xi(\chi)$ under finite entanglement scaling. We found that the central charge obtained in this manner scales with circumference L_y. This scaling appears consistent with the existence or emergence of a (two-dimensional) Fermi surface at the critical point, as in Geraedts et al. (2016) and Gong et al. (2019). While we are unable to provide a complete theory describing where such a Fermi surface stems from, we believe that the consistency between our results and such a theory should be taken seriously.

Apart from the Fermi surface theory, we have identified two recent theories that could be candidates for providing an explanation for our phase transition. Both of the theories we considered describe the critical system as Dirac points carrying fixed central charge. This already contradicts our finding of a central charge which varies with circumference. Additionally, a theory capturing our phase transition would require the simultaneous change of the composite fermion (CF) band Chern number, and the fractionalisation of electrons into three partons. Neither of the theories we considered fulfil this requirement. Herein lies the importance of our findings: we have strong numerical evidence for the existence of topological phase transitions that are not captured by current theories.

While the $\nu = 1/3$ Laughlin state formed the main focus of chapter 6, we have extended our work there to the next state in the FQH hierarchy at $\nu = 2/5$. This work suffers from the same difficulties in capturing the $\nu = 2/5$ state using finite-χ numerics as those we described for the $\nu = 1/3$ state, as well as the somewhat limited predictions for finite size $\nu = 2/5$ states in the literature. Nonetheless, we have, at $L_y = 6$ and $n_\phi = 5/16$, observed a clear transition from a $C = -6$ ICI (supported on two out of the five magnetic sub-bands) to a $\nu = 2/5$ FQH state. This transition appears to take place via an as yet unidentified intermediate phase, characterised by a plateau in the entanglement entropy S_E, a series of level crossings in the momentum-resolved entanglement spectrum and the spectrum of the single-particle density matrix, as well as a Hall response $\sigma_H = +2$. It is unclear whether this transition can and should be captured by the same theory describing the transition into the $\nu = 1/3$ state. We therefore recommend this as a field for future research.

To finish this chapter, we now provide an overview of some avenues of further study opened up by the work in this thesis. We here make suggestions that remain fairly closely related to the work presented in this thesis. However, we do point out that any (further) study in this field can have potential implications for our understanding of the interplay between topology and physics in general, and could therefore affect a range of potential

applications as mentioned in the introduction. Firstly, as already mentioned, the work in chapter 5 could benefit from an independent replication, particularly of the results for the $\nu = 2/5$ state, as well as an extension to further hierarchy states. Additionally, the methods used in that chapter can be extended to more exotic QH states, such as non-Abelian states. Finally, extending the work of chapter 5 to FQH states supported not by the entire LLL tail, but by a subset of sub-bands forms another interesting opportunity.

Chapter 6 yields several additional opportunities for future study. Firstly, as stated above, there is a gap in the theoretical understanding of the phase transitions described in that chapter. The development of such a theory (or theories, if the $\nu = 1/3$ and $\nu = 2/5$ cases require independent descriptions) could yield exciting new understanding of QH physics. Additionally, the methods from chapter 6 can be applied to study phase transitions into other FQH hierarchy states, as well as more exotic states. Extending the methods to the bosonic Harper-Hofstadter model, for example by studying transitions from a Bose-Einstein condensate into various QH states, could also be interesting, particularly given recent experimental realisations of the bosonic model which would allow for numerics to be checked against experiments. A last extension, finally, is given by the potential existence of transitions between *distinct* fractional Chern insulator (FCI) states, with one state supported on the full LLL tail, and another supported on a subset of the sub-bands forming the tail. While this would require the improvement of some current numerical techniques, if such transitions can be found, they would provide access to a rich landscape of QH plateau transitions.

Bibliography

Affleck, Ian, Tom Kennedy, Elliott H. Lieb, and Hal Tasaki (1987). "Rigorous Results on Valence-Bond Ground States in Antiferromagnets". In: *Physical Review Letters* 59, pp. 799–802. DOI: 10.1103/PhysRevLett.59.799.

Affleck, Ian, Tom Kennedy, Elliott H. Lieb, and Hal Tasaki (1988). "Valence Bond Ground States in Isotropic Quantum Antiferromagnets". In: *Communications in Mathematical Physics* 115, pp. 477–528. DOI: 10.1007/BF01218021.

Aidelsburger, M, M Atala, M Lohse, J T Barreiro, B Paredes, and I Bloch (2013). "Realization of the Hofstadter Hamiltonian with Ultracold Atoms in Optical Lattices". In: *Physical Review Letters* 111, p. 185301. DOI: 10.1103/PhysRevLett.111.185301.

Aidelsburger, M, M Lohse, C Schweizer, M Atala, J T Barreiro, S Nascimbène, N R Cooper, I Bloch, and N Goldman (2014). "Measuring the Chern Number of Hofstadter Bands with Ultracold Bosonic Atoms". In: *Nature Physics* 11, pp. 162–166. DOI: 10.1038/nphys3171.

Ando, Tsuneya (1983). "Electron Localization in a Two-Dimensional System in Strong Magnetic Fields. I. Case of Short-Range Scatterers". In: *Journal of the Physical Society of Japan* 52, pp. 1740–1749. DOI: 10.1143/JPSJ.52.1740.

Andrews, Bartholomew, Madhav Mohan, and Titus Neupert (2020). "Abelian Topological Order of $\nu = 2/5$ and $3/7$ Fractional Quantum Hall States in Lattice Models". In: arXiv: 2007.08870.

Andrews, Bartholomew and Gunnar Möller (2018). "Stability of Fractional Chern Insulators in the Effective Continuum Limit of Harper-Hofstadter Bands with Chern Number $|C| > 1$". In: *Physical Review B* 97, p. 035159. DOI: 10.1103/PhysRevB.97.035159.

Andrews, Bartholomew and Alexey Soluyanov (2020). "Fractional Quantum Hall States for Moiré Superstructures in the Hofstadter Regime". In: *Physical Review B* 101, p. 235312. DOI: 10.1103/PhysRevB.101.235312.

Aoki, H. and T. Ando (1981). "Effect of Localization on the Hall Conductivity in the Two-Dimensional System in Strong Magnetic Fields". In: *Solid State Communications* 38.11, pp. 1079–1082. DOI: 10.1016/0038-1098(81)90021-1.

Ardonne, E. and N. Regnault (2011). "Structure of Spinful Quantum Hall States: A Squeezing Perspective". In: *Physical Review B* 84, p. 205134. DOI: 10.1103/PhysRevB.84.205134.

Arovas, Daniel P., Robert Schrieffer, Frank Wilczek, and A. Zee (1985). "Statistical Mechanics of Anyons". In: *Nuclear Physics B* 251, pp. 117–126. DOI: 10.1016/0550-3213(85)90252-4.

Asoudeh, M., V. Karimipour, and A. Sadrolashrafi (June 2007). "Quantum Phase Transitions and Matrix Product States in Spin Ladders". In: *Physical Review B* 75.22, p. 224427. DOI: 10.1103/PhysRevB.75.224427.

Azbel, M. Ya. (1964). "Energy Spectrum of a Conduction Electron in a Magnetic Field". In: *Soviet Physics JETP* 19, pp. 634–645.

Barkeshli, M., N. Y. Yao, and C. R. Laumann (2015). "Continuous Preparation of a Fractional Chern Insulator". In: *Physical Review Letters* 115, p. 026802. DOI: 10.1103/PhysRevLett.115.026802.

Barkeshli, Maissam and John McGreevy (2014). "Continuous Transition between Fractional Quantum Hall and Superfluid States". In: *Physical Review B* 89, p. 235116. DOI: 10.1103/PhysRevB.89.235116.

Bauer, B., P. Corboz, R. Orús, and M. Troyer (2011). "Implementing Global Abelian Symmetries in Projected Entangled-Pair State Algorithms". In: *Physical Review B* 83, p. 125106. DOI: 10.1103/PhysRevB.83.125106.

Bauer, David, T. S. Jackson, and Rahul Roy (2016). "Quantum Geometry and Stability of the Fractional Quantum Hall Effect in the Hofstadter Model". In: *Physical Review B* 93, p. 235133. DOI: 10.1103/PhysRevB.93.235133.

Baxter, R. J. (1968). "Dimers on a Rectangular Lattice". In: *Journal of Mathematical Physics* 9, pp. 650–654. DOI: 10.1063/1.1664623.

Baxter, R. J. (1978). "Variational Approximations for Square Lattice Models in Statistical Mechanics". In: *Journal of Statistical Physics* 19, pp. 461–478. DOI: 10.1007/BF01011693.

Bergholtz, Emil J. and Zhao Liu (2013). "Topological Flat Band Models and Fractional Chern Insulators". In: *International Journal of Modern Physics B* 27, p. 1330017. DOI: 10.1142/S021797921330017X.

Bernevig, B. Andrei and F. D. M. Haldane (2008). "Model Fractional Quantum Hall States and Jack Polynomials". In: *Physical Review Letters* 100, p. 246802. DOI: 10.1103/PhysRevLett.100.246802.

Berry, M.V. (1984). "Quantal Phase Factors Accompanying Adiabatic Changes". In: *Proceedings of the Royal Society of London. A* 392, pp. 45–57. DOI: 10.1098/rspa.1984.0023.

Burnell, F.J. (Mar. 2018). "Anyon Condensation and Its Applications". In: *Annual Review of Condensed Matter Physics* 9.1, pp. 307–327. DOI: 10.1146/annurev-conmatphys-033117-054154.

Calabrese, Pasquale and John Cardy (2009). "Entanglement Entropy and Conformal Field Theory". In: *Journal of Physics A: Mathematical and Theoretical* 42.50, p. 504005. DOI: 10.1088/1751-8113/42/50/504005.

Chalker, J. T. and P. D. Coddington (1988). "Percolation, Quantum Tunnelling and the Integer Hall Effect". In: *Journal of Physics C: Solid State Physics* 21, pp. 2665–2679. DOI: 10.1088/0022-3719/21/14/008.

Chang, A. M. (2003). "Chiral Luttinger Liquids at the Fractional Quantum Hall Edge". In: *Reviews of Modern Physics* 75, pp. 1449–1505. DOI: 10.1103/RevModPhys.75.1449.

Chang, A. M., L. N. Pfeiffer, and K. W. West (1996). "Observation of Chiral Luttinger Behavior in Electron Tunneling into Fractional Quantum Hall Edges". In: *Physical Review Letters* 77, pp. 2538–2541. DOI: 10.1103/PhysRevLett.77.2538.

Chen, Wei, Matthew P. A. Fisher, and Yong-Shi Wu (1993). "Mott Transition in an Anyon Gas". In: *Physical Review B* 48, pp. 13749–13761. DOI: 10.1103/PhysRevB.48.13749.

Chen, Xiao, William Witczak-Krempa, Thomas Faulkner, and Eduardo Fradkin (2017). "Two-Cylinder Entanglement Entropy under a Twist". In: *Journal of Statistical Mechanics: Theory and Experiment* 043104. DOI: 10.1088/1742-5468/aa668a.

Chern, Shiing-shen (1945). "On the Curvatura Integra in a Riemannian Manifold". In: *Annals of Mathematics* 46, pp. 674–684. DOI: 10.2307/1969203.

Cirac, J. Ignacio, Didier Poilblanc, Norbert Schuch, and Frank Verstraete (2011). "Entanglement Spectrum and Boundary Theories with Projected Entangled-Pair States". In: *Physical Review B* 83, p. 245134. DOI: 10.1103/PhysRevB.83.245134.

Corboz, Philippe, Román Orús, Bela Bauer, and Guifré Vidal (2010). "Simulation of Strongly Correlated Fermions in Two Spatial Dimensions with Fermionic Projected Entangled-Pair States". In: *Physical Review B - Condensed Matter and Materials Physics* 81, p. 165104. DOI: 10.1103/PhysRevB.81.165104.

Corboz, Philippe and Guifre Vidal (2009). "Fermionic Multiscale Entanglement Renormalization Ansatz". In: *Physical Review B* 80, p. 165129. DOI: 10.1103/PhysRevB.80.165129.

Cozzini, Marco, Radu Ionicioiu, and Paolo Zanardi (Sept. 2007). "Quantum Fidelity and Quantum Phase Transitions in Matrix Product States". In: *Physical Review B* 76.10, p. 104420. DOI: 10.1103/PhysRevB.76.104420.

Crosswhite, Gregory M. and Dave Bacon (2008). "Finite Automata for Caching in Matrix Product Algorithms". In: *Physical Review A - Atomic, Molecular, and Optical Physics* 78, p. 012356. DOI: 10.1103/PhysRevA.78.012356.

Crosswhite, Gregory M., A. C. Doherty, and Guifré Vidal (2008). "Applying Matrix Product Operators to Model Systems with Long-Range Interactions". In: *Physical Review B* 78, p. 035116. DOI: 10.1103/PhysRevB.78.035116.

de-Picciotto, R., M. Reznikov, M. Heiblum, V. Umansky, G. Bunin, and D. Mahalu (1997). "Direct Observation of a Fractional Charge". In: *Nature* 389, p. 162. DOI: 10.1038/38241.

Eisert, J., M. Cramer, and M. B. Plenio (2010). "Colloquium: Area Laws for the Entanglement Entropy". In: *Reviews of Modern Physics* 82, pp. 277–306. DOI: 10.1103/RevModPhys.82.277.

Engel, L., H. P. Wei, D. C. Tsui, and M. Shayegan (1990). "Critical Exponent in the Fractional Quantum Hall Effect". In: *Surface Science* 229, pp. 13–15. DOI: 10.1016/0039-6028(90)90820-X.

Evenbly, G and G Vidal (2009). "Entanglement Renormalization in Two Spatial Dimensions". In: *Physical Review Letters* 102, p. 180406. DOI: 10.1103/PhysRevLett.102.180406.

Evenbly, Glen (2010). "Foundations and Applications of Entanglement Renormalization". PhD thesis. University of Queensland. arXiv: 1109.5424.

Fannes, M., B. Nachtergaele, and R. F. Werner (1992). "Finitely Correlated States on Quantum Spin Chains". In: *Communications in Mathematical Physics* 144, pp. 443–490. DOI: 10.1007/BF02099178.

Feigin, B., M. Jimbo, T. Miwa, and E. Mukhin (2002). "A Differential Ideal of Symmetric Polynomials Spanned by Jack Polynomials at $\beta = -(r-1)/(k+1)$". In: *International Mathematics Research Notices* 2002, pp. 1223–1237. DOI: 10.1155/S1073792802112050.

Fradkin, E. (2013). *Field Theories of Condensed Matter Physics*. Cambridge University Press.

Francesco, Philippe, Pierre Mathieu, and David Sénéchal (1997). *Conformal Field Theory*. Graduate Texts in Contemporary Physics. New York: Springer-Verlag. DOI: 10.1007/978-1-4612-2256-9.

Fröwis, F., V. Nebendahl, and W. Dür (2010). "Tensor Operators: Constructions and Applications for Long-Range Interaction Systems". In: *Physical Review A* 81, p. 062337. DOI: 10.1103/PhysRevA.81.062337.

Gavrilenko, V.I. and A.V. Ikonnikov (1986). *Quantum Hall Effect*. Moscow: Znanie.

Geraedts, S. D., M. P. Zaletel, R. S. K. Mong, M. A. Metlitski, A. Vishwanath, and O. I. Motrunich (2016). "The Half-Filled Landau Level: The Case for Dirac Composite Fermions". In: *Science* 352, pp. 197–201. DOI: 10.1126/science.aad4302.

Gerster, Matthias, Matteo Rizzi, Pietro Silvi, Marcello Dalmonte, and Simone Montangero (2017). "Fractional Quantum Hall Effect in the Interacting Hofstadter Model via Tensor Networks". In: *Physical Review B* 96, p. 195123. DOI: 10.1103/PhysRevB.96.195123.

Girvin, Steven M. (1999). "The Quantum Hall Effect: Novel Excitations and Broken Symmetries". In: *Topological Aspects of Low Dimensional Systems*. Les Houches - Ecole d'Ete de Physique Theorique 69. Berlin, Heidelberg: Springer. DOI: 10.1007/3-540-46637-1_2.

Gohlke, Matthias, Ruben Verresen, Roderich Moessner, and Frank Pollmann (2017). "Dynamics of the Kitaev-Heisenberg Model". In: *Physical Review Letters* 119, p. 157203. DOI: 10.1103/PhysRevLett.119.157203.

Gong, Shou-Shu, Wayne Zheng, Mac Lee, Yuan-Ming Lu, and D. N. Sheng (2019). "Chiral Spin Liquid with Spinon Fermi Surfaces in the Spin-$\frac{1}{2}$ Triangular Heisenberg Model". In: *Physical Review B* 100, p. 241111. DOI: 10.1103/PhysRevB.100.241111.

Grover, Tarun and Ashvin Vishwanath (2013). "Quantum Phase Transition between Integer Quantum Hall States of Bosons". In: *Physical Review B* 87, p. 045129. DOI: 10.1103/PhysRevB.87.045129.

Grushin, Adolfo G., Johannes Motruk, Michael P. Zaletel, and Frank Pollmann (2015). "Characterization and Stability of a Fermionic $\nu = 1/3$ Fractional Chern Insulator". In: *Physical Review B - Condensed Matter and Materials Physics* 91, p. 035136. DOI: 10.1103/PhysRevB.91.035136.

Hafezi, M., A. S. Sørensen, E. Demler, and M. D. Lukin (2007). "Fractional Quantum Hall Effect in Optical Lattices". In: *Physical Review A* 76, p. 023613. DOI: 10.1103/PhysRevA.76.023613.

Haldane, F. D. M. (1983). "Fractional Quantization of the Hall Effect: A Hierarchy of Incompressible Quantum Fluid States". In: *Physical Review Letters* 51, pp. 605–608. DOI: 10.1103/PhysRevLett.51.605.

Haldane, F. D. M. (1988). "Model for a Quantum Hall Effect without Landau Levels: Condensed-Matter Realization of the "Parity Anomaly"". In: *Physical Review Letters* 61, p. 2015. DOI: 10.1103/PhysRevLett.61.2015.

Haldane, F. D. M. (1991). "Fractional Statistics in Arbitrary Dimensions: A Generalization of the Pauli Principle". In: *Physical Review Letters* 67, pp. 937–940. DOI: 10.1103/PhysRevLett.67.937.

Haldane, F. D. M. (2006). "Pauli-like Principle for Abelian and Non-Abelian FQHE Quasiparticles". In: *Bulletin of the American Physical Society* 51, p. 16.

Halperin, B. I. (1982). "Quantized Hall Conductance, Current-Carrying Edge States, and the Existence of Extended States in a Two-Dimensional Disordered Potential". In: *Physical Review B* 25, pp. 2185–2190. DOI: 10.1103/PhysRevB.25.2185.

Halperin, B. I. (1984). "Statistics of Quasiparticles and the Hierarchy of Fractional Quantized Hall States". In: *Physical Review Letters* 52, pp. 1583–1586. DOI: 10.1103/PhysRevLett.52.1583.

Haque, Masudul, Oleksandr Zozulya, and Kareljan Schoutens (2007). "Entanglement Entropy in Fermionic Laughlin States". In: *Physical Review Letters* 98, p. 060401. DOI: 10.1103/PhysRevLett.98.060401.

Harper, P. G. (1955). "Single Band Motion of Conduction Electrons in a Uniform Magnetic Field". In: *Proceedings of the Physical Society. Section A* 68, pp. 874–878. DOI: 10.1088/0370-1298/68/10/304.

Hasan, M. Z. and C. L. Kane (2010). "Colloquium : Topological Insulators". In: *Reviews of Modern Physics* 82, pp. 3045–3067. DOI: 10.1103/RevModPhys.82.3045.

Hastings, M. B. (2007). "An Area Law for One-Dimensional Quantum Systems". In: *Journal of Statistical Mechanics* 2007, P08024–P08024. DOI: 10.1088/1742-5468/2007/08/P08024.

Hauschild, Johannes and Frank Pollmann (2018). "Efficient Numerical Simulations with Tensor Networks: Tensor Network Python (TeNPy)". In: *SciPost Physics Lecture Notes* 5. DOI: 10.21468/SciPostPhysLectNotes.5.

Hermanns, M., A. Chandran, N. Regnault, and B. Andrei Bernevig (2011). "Haldane statistics in the finite-size entanglement spectra of $1/m$ fractional quantum Hall states". In: *Physical Review B* 84, p. 121309. DOI: 10.1103/PhysRevB.84.121309.

Hofstadter, Douglas R. (1976). "Energy Levels and Wave Functions of Bloch Electrons in Rational and Irrational Magnetic Fields". In: *Physical Review B* 14, pp. 2239–2249. DOI: 10.1103/PhysRevB.14.2239.

Hu, Zi-Xiang, Z. Papić, S. Johri, R.N. Bhatt, and Peter Schmitteckert (June 2012). "Comparison of the Density-Matrix Renormalization Group Method Applied to Fractional Quantum Hall Systems in Different Geometries". In: *Physics Letters A* 376.30-31, pp. 2157–2161. DOI: 10.1016/j.physleta.2012.05.031.

Hubig, C., I. P. McCulloch, U. Schollwöck, and F. A. Wolf (2015). "Strictly Single-Site DMRG Algorithm with Subspace Expansion". In: *Physical Review B* 91, p. 155115. DOI: 10.1103/physrevb.91.155115.

Huckestein, Bodo (1995). "Scaling Theory of the Integer Quantum Hall Effect". In: *Reviews of Modern Physics* 67, pp. 357–396. DOI: 10.1103/RevModPhys.67.357.

Ising, Ernst (1925). "Beitrag Zur Theorie Des Ferromagnetismus". In: *Zeitschrift für Physik* 31.1, pp. 253–258. DOI: 10.1007/BF02980577.

Jain, Jainendra K (1989). "Composite-Fermion Approach for the Fractional Quantum Hall Effect". In: *Physical Review Letters* 63, pp. 199–202. DOI: 10.1103/PhysRevLett.63.199.

Jain, Jainendra K. (2007). *Composite Fermions*. Cambridge University Press.

Kane, C. L. and Matthew P. A. Fisher (1995). "Impurity Scattering and Transport of Fractional Quantum Hall Edge States". In: *Physical Review B* 51, pp. 13449–13466. DOI: 10.1103/PhysRevB.51.13449.

Kardar, Mehran (2007). *Statistical Physics of Particles*. Cambridge : New York: Cambridge University Press.

Khmelnitskii, D.E. (1983). "Quantization of Hall Conductivity". In: *JETP Letters* 38, pp. 552–556.

Kitaev, Alexei and John Preskill (2006). "Topological Entanglement Entropy". In: *Physical Review Letters* 96, p. 110404. DOI: 10.1103/PhysRevLett.96.110404.

Kivelson, Steven, Dung-Hai Lee, and Shou-Cheng Zhang (1992). "Global Phase Diagram in the Quantum Hall Effect". In: *Physical Review B* 46, pp. 2223–2238. DOI: 10.1103/PhysRevB.46.2223.

Kjall, Jonas A, Michael P Zaletel, Roger S K Mong, Jens H Bardarson, and Frank Pollmann (2013). "Phase Diagram of the Anisotropic Spin-2 XXZ Model: Infinite-System Density Matrix Renormalization Group Study". In: *Physical Review B* 87, p. 235106. DOI: 10.1103/PhysRevB.87.235106.

Klitzing, K. V., G. Dorda, and M. Pepper (1980). "New Method for High-Accuracy Determination of the Fine-Structure Constant Based on Quantized Hall Resistance". In: *Physical Review Letters* 45, pp. 494–497. DOI: 10.1103/PhysRevLett.45.494.

Kol, A. and N. Read (1993). "Fractional Quantum Hall Effect in a Periodic Potential". In: *Physical Review B* 48, pp. 8890–8898. DOI: 10.1103/PhysRevB.48.8890.

Lanczos, C. (1950). "An Iteration Method for the Solution of the Eigenvalue Problem of Linear Differential and Integral Operators". In: *Journal of Research of the National Bureau of Standards* 45, p. 255. DOI: 10.6028/jres.045.026.

Landau, L. (1937). "On the Theory of Phase Transitions". In: *JETP* 7, pp. 19–32.

Läuchli, Andreas M., Emil J. Bergholtz, and Masudul Haque (2010). "Entanglement Scaling of Fractional Quantum Hall States through Geometric Deformations". In: *New Journal of Physics* 12, p. 075004. DOI: 10.1088/1367-2630/12/7/075004.

Laughlin, R. B. (1981). "Quantized Hall Conductivity in Two Dimensions". In: *Physical Review B* 23, pp. 5632–5633. DOI: 10.1103/PhysRevB.23.5632.

Laughlin, R. B. (1983). "Anomalous Quantum Hall Effect: An Incompressible Quantum Fluid with Fractionally Charged Excitations". In: *Physical Review Letters* 50, pp. 1395–1398. DOI: 10.1103/PhysRevLett.50.1395.

Laughlin, R. B. (1988). "Superconducting Ground State of Noninteracting Particles Obeying Fractional Statistics". In: *Physical Review Letters* 60, pp. 2677–2680. DOI: 10.1103/PhysRevLett.60.2677.

Lee, Jong Yeon, Chong Wang, Michael P. Zaletel, Ashvin Vishwanath, and Yin-Chen He (2018). "Emergent Multi-Flavor QED_3 at the Plateau Transition between Fractional Chern Insulators: Applications to Graphene Heterostructures". In: *Physical Review X* 8, p. 031015. DOI: 10.1103/PhysRevX.8.031015.

Levin, Michael and Xiao-Gang Wen (2006). "Detecting Topological Order in a Ground State Wave Function". In: *Physical Review Letters* 96, p. 110405. DOI: 10.1103/PhysRevLett.96.110405.

Li, Hui and F. D. M. Haldane (2008). "Entanglement Spectrum as a Generalization of Entanglement Entropy: Identification of Topological Order in Non-Abelian Fractional Quantum Hall Effect States". In: *Physical Review Letters* 101, p. 010504. DOI: 10.1103/PhysRevLett.101.010504.

Lu, Yuan-Ming and Dung-Hai Lee (2014). "Quantum Phase Transitions between Bosonic Symmetry-Protected Topological Phases in Two Dimensions: Emergent QED 3 and Anyon Superfluid". In: *Physical Review B* 89, p. 195143. DOI: 10.1103/PhysRevB.89.195143.

Ma, Ruochen and Yin-Chen He (2020). "Emergent QCD_3 Quantum Phase Transitions of Fractional Chern Insulators". In: *Physical Review Research* 2, p. 033348. DOI: 10.1103/PhysRevResearch.2.033348.

McCulloch, Ian P. (2007). "From Density-Matrix Renormalization Group to Matrix Product States". In: *Journal of Statistical Mechanics: Theory and Experiment* 2007, P10014. DOI: 10.1088/1742-5468/2007/10/P10014.

McCulloch, Ian P. (2008). "Infinite Size Density Matrix Renormalization Group, Revisited". In: arXiv: 0804.2509.

Miyake, Hirokazu, Georgios A. Siviloglou, Colin J. Kennedy, William Cody Burton, and Wolfgang Ketterle (2013). "Realizing the Harper Hamiltonian with Laser-Assisted Tunneling in Optical Lattices". In: *Physical Review Letters* 111, p. 185302. DOI: 10.1103/PhysRevLett.111.185302.

Möller, G. and N. R. Cooper (2010). "Condensed Ground States of Frustrated Bose-Hubbard Models". In: *Physical Review A* 82, p. 063625. DOI: 10.1103/PhysRevA.82.063625.

Möller, Gunnar and N. R. Cooper (2009). "Composite Fermion Theory for Bosonic Quantum Hall States on Lattices". In: *Physical Review Letters* 103, p. 105303. DOI: 10.1103/PhysRevLett.103.105303.

Möller, Gunnar and N. R. Cooper (2015). "Fractional Chern Insulators in Harper-Hofstadter Bands with Higher Chern Number". In: *Physical Review Letters* 115, p. 126401. DOI: 10.1103/PhysRevLett.115.126401.

Moore, Gregory and Nicholas Read (1991). "Nonabelions in the Fractional Quantum Hall Effect". In: *Nuclear Physics B* 360, pp. 362–396. DOI: 10.1016/0550-3213(91)90407-O.

Motruk, Johannes and Frank Pollmann (2017). "Phase Transitions and Adiabatic Preparation of a Fractional Chern Insulator in a Boson Cold-Atom Model". In: *Physical Review B* 96, p. 165107. DOI: 10.1103/PhysRevB.96.165107.

Motruk, Johannes, Michael P Zaletel, Roger S K Mong, and Frank Pollmann (2016). "Density Matrix Renormalization Group on a Cylinder in Mixed Real and

Momentum Space". In: *Physical Review B* 93, p. 155139. DOI: 10.1103/PhysRevB.93.155139.

Murg, V., F. Verstraete, Ö. Legeza, and R. M. Noack (2010). "Simulating Strongly Correlated Quantum Systems with Tree Tensor Networks". In: *Physical Review B* 82, p. 205105. DOI: 10.1103/PhysRevB.82.205105.

Neupert, Titus, Luiz Santos, Claudio Chamon, and Christopher Mudry (2011). "Fractional Quantum Hall States at Zero Magnetic Field". In: *Physical Review Letters* 106, p. 236804. DOI: 10.1103/PhysRevLett.106.236804.

Nishino, T (1995). "Density Matrix Renormalization Group Method for 2D Classical Models". In: *Journal of the Physical Society of Japan* 64, pp. 3598–3601. DOI: 10.1143/JPSJ.64.3598.

Nishino, Tomotoshi and Kouichi Okunishi (1996). "Corner Transfer Matrix Renormalization Group Method". In: *Journal of the Physical Society of Japan* 65, pp. 891–894. DOI: 10.1143/JPSJ.65.891.

Nishino, Tomotoshi and Kouichi Okunishi (1997). "Corner Transfer Matrix Algorithm for Classical Renormalization Group". In: *Journal of the Physical Society of Japan* 66, pp. 3040–3047. DOI: 10.1143/JPSJ.66.3040.

Onsager, Lars (Feb. 1944). "Crystal Statistics. I. A Two-Dimensional Model with an Order-Disorder Transition". In: *Physical Review* 65.3-4, pp. 117–149. DOI: 10.1103/PhysRev.65.117.

Orús, Román (2014). "A Practical Introduction to Tensor Networks: Matrix Product States and Projected Entangled Pair States". In: *Annals of Physics* 349, pp. 117–158. DOI: 10.1016/j.aop.2014.06.013.

Osadchy, D. and J. E. Avron (2001). "Hofstadter Butterfly as Quantum Phase Diagram". In: *Journal of Mathematical Physics* 42, pp. 5665–5671. DOI: 10.1063/1.1412464.

Oseledets, I. V. (2011). "Tensor-Train Decomposition". In: *SIAM Journal on Scientific Computing* 33, pp. 2295–2317. DOI: 10.1137/090752286.

Ostlund, Stellan and Stefan Rommer (1995). "Thermodynamic Limit of Density Matrix Renormalization". In: *Physical Review Letters* 75, pp. 3537–3540. DOI: 10.1103/PhysRevLett.75.3537.

Palmer, R. N. and D. Jaksch (2006). "High-Field Fractional Quantum Hall Effect in Optical Lattices". In: *Physical Review Letters* 96, p. 180407. DOI: 10.1103/PhysRevLett.96.180407.

Papić, Z. (2014). "Solvable Models for Unitary and Nonunitary Topological Phases". In: *Physical Review B* 90, p. 075304. DOI: 10.1103/PhysRevB.90.075304.

Parameswaran, Siddharth A, Rahul Roy, and Shivaji L Sondhi (2013). "Fractional Quantum Hall Physics in Topological Flat Bands". In: *Comptes Rendus Physique* 14, pp. 816–839. DOI: 10.1016/j.crhy.2013.04.003.

Pauli, W. (1925). "Über den Zusammenhang des Abschlusses der Elektronengruppen im Atom mit der Komplexstruktur der Spektren". In: *Zeitschrift für Physik* 31, pp. 765–783. DOI: 10.1007/BF02980631.

Penrose, Roger (1971). "Applications of Negative Dimensional Tensors". In: *Combinatorial Mathematics and Its Applications*. Vol. 1. Oxford: Academic Press, pp. 221–244.

Perez-Garcia, David, Frank Verstraete, Michael M Wolf, and J I Cirac (2007). "Matrix Product State Representations". In: *Quantum Information and Computation* 7, p. 401. arXiv: quant-ph/0608197.

Pillay, Jason Cornelius (Mar. 2020). "Matrix Product State Study of Strongly-Interacting Systems and Quantum Phase Transitions". PhD Thesis. The University of Queensland. DOI: 10.14264/uql.2020.489.

Pirvu, B, V Murg, J I Cirac, and F Verstraete (2010). "Matrix Product Operator Representations". In: *New Journal of Physics* 12, p. 025012. DOI: 10.1088/1367-2630/12/2/025012.

Pollmann, Frank, Subroto Mukerjee, Ari M. Turner, and Joel E. Moore (2009). "Theory of Finite-Entanglement Scaling at One-Dimensional Quantum Critical Points". In: *Physical Review Letters* 102, p. 255701. DOI: 10.1103/PhysRevLett.102.255701.

Pollmann, Frank and Ari M Turner (2012). "Detection of Symmetry-Protected Topological Phases in One Dimension". In: *Physical Review B - Condensed Matter and Materials Physics* 86, p. 125441. DOI: 10.1103/PhysRevB.86.125441.

Prange, R. E. and Robert Joynt (1982). "Conduction in a Strong Field in Two Dimensions: The Quantum Hall Effect". In: *Physical Review B* 25, p. 2943. DOI: 10.1103/PhysRevB.25.2943.

Qi, Xiao-Liang (2011). "Generic Wave-Function Description of Fractional Quantum Anomalous Hall States and Fractional Topological Insulators". In: *Physical Review Letters* 107, p. 126803. DOI: 10.1103/PhysRevLett.107.126803.

Regnault, N. (2017). "Entanglement Spectroscopy and Its Application to the Quantum Hall Effects". In: *Topological Aspects of Condensed Matter Physics: Lecture Notes of the Les Houches Summer School, August 2014* 103, pp. 165–215. DOI: 10.1093/acprof:oso/9780198785781.003.0004.

Regnault, N., B. A. Bernevig, and F. D. M. Haldane (2009). "Topological Entanglement and Clustering of Jain Hierarchy States". In: *Physical Review Letters* 103, p. 016801. DOI: 10.1103/PhysRevLett.103.016801.

Regnault, N and B. Andrei Bernevig (2011). "Fractional Chern Insulator". In: *Physical Review X* 1.2, p. 021014. DOI: 10.1103/PhysRevX.1.021014.

Rosson, Paolo, Michael Lubasch, Martin Kiffner, and Dieter Jaksch (2019). "Bosonic Fractional Quantum Hall States on a Finite Cylinder". In: *Physical Review A* 99, p. 033603. DOI: 10.1103/PhysRevA.99.033603.

Roy, Rahul (2014). "Band Geometry of Fractional Topological Insulators". In: *Physical Review B* 90, p. 165139. DOI: 10.1103/PhysRevB.90.165139.

Saminadayar, L., D. C. Glattli, Y. Jin, and B. Etienne (1997). "Observation of the $e/3$ Fractionally Charged Laughlin Quasiparticle". In: *Physical Review Letters* 79, pp. 2526–2529. DOI: 10.1103/PhysRevLett.79.2526.

Scaffidi, Thomas and Gunnar Möller (2012). "Adiabatic Continuation of Fractional Chern Insulators to Fractional Quantum Hall States". In: *Physical Review Letters* 109, p. 246805. DOI: 10.1103/PhysRevLett.109.246805.

Schmoll, Philipp, Sukhbinder Singh, Matteo Rizzi, and Román Orús (2020). "A Programming Guide for Tensor Networks with Global S U (2) Symmetry". In: *Annals of Physics* 419, p. 168232. DOI: 10.1016/j.aop.2020.168232.

Schollwöck, Ulrich (2011). "The Density-Matrix Renormalization Group in the Age of Matrix Product States". In: *Annals of Physics* 326, pp. 96–192. DOI: 10.1016/j.aop.2010.09.012.

Schoonderwoerd, Leon (2020). *Additional Entanglement Spectra for "Quantum Hall States in the Harper-Hofstadter Model: Existence, Stability and Novel Phase Transitions"*. DOI: 10.5281/zenodo.4040500.

Schoonderwoerd, Leon, Frank Pollmann, and Gunnar Möller (2019). "Interaction-Driven Plateau Transition between Integer and Fractional Chern Insulators". In: arXiv: 1908.00988 [cond-mat].

Shi, Y. Y., L. M. Duan, and G. Vidal (2006). "Classical Simulation of Quantum Many-Body Systems with a Tree Tensor Network". In: *Physical Review A* 74, p. 022320. DOI: 10.1103/PhysRevA.74.022320.

Singh, Sukhwinder, Robert N. C. Pfeifer, and Guifré Vidal (2010). "Tensor Network Decompositions in the Presence of a Global Symmetry". In: *Physical Review A* 82, p. 050301. DOI: 10.1103/PhysRevA.82.050301.

Singh, Sukhwinder, Robert N. C. Pfeifer, and Guifre Vidal (2011). "Tensor Network States and Algorithms in the Presence of a Global U(1) Symmetry". In: *Physical Review B* 83, p. 115125. DOI: 10.1103/PhysRevB.83.115125.

Sondhi, S. L., S. M. Girvin, J. P. Carini, and D. Shahar (1997). "Continuous Quantum Phase Transitions". In: *Reviews of Modern Physics* 69, pp. 315–333. DOI: 10.1103/RevModPhys.69.315.

Sørensen, Anders S., Eugene Demler, and Mikhail D. Lukin (2005). "Fractional Quantum Hall States of Atoms in Optical Lattices". In: *Physical Review Letters* 94, p. 086803. DOI: 10.1103/PhysRevLett.94.086803.

Sterdyniak, Antoine, Nicolas Regnault, and Gunnar Möller (2012). "Particle Entanglement Spectra for Quantum Hall States on Lattices". In: *Physical Review B* 86, p. 165314. DOI: 10.1103/PhysRevB.86.165314.

Tagliacozzo, L., Thiago R. De Oliveira, S. Iblisdir, and J. I. Latorre (2008). "Scaling of Entanglement Support for Matrix Product States". In: *Physical Review B - Condensed Matter and Materials Physics* 78, p. 024410. DOI: 10.1103/PhysRevB.78.024410.

Tagliacozzo, L., G. Evenbly, and G. Vidal (2009). "Simulation of Two-Dimensional Quantum Systems Using a Tree Tensor Network That Exploits the Entropic Area Law". In: *Physical Review B* 80, p. 235127. DOI: 10.1103/PhysRevB.80.235127.

Takasaki, Hiroshi, Toshiya Hikihara, and Tomotoshi Nishino (1999). "Fixed Point of the Finite System DMRG". In: *Journal of the Physical Society of Japan* 68, pp. 1537–1540. DOI: 10.1143/JPSJ.68.1537.

Thouless, D. J., Mahito Kohmoto, M. P. Nightingale, and M. den Nijs (1982). "Quantized Hall Conductance in a Two-Dimensional Periodic Potential". In: *Physical Review Letters* 49, pp. 405–408. DOI: 10.1103/PhysRevLett.49.405.

Tong, David (2016). "Lectures on the Quantum Hall Effect". In: arXiv: 1606.06687.

Trugman, S. A. and S. Kivelson (1985). "Exact Results for the Fractional Quantum Hall Effect with General Interactions". In: *Physical Review B* 31, pp. 5280–5284. DOI: 10.1103/PhysRevB.31.5280.

Tsui, D. C., H. L. Stormer, and A. C. Gossard (1982). "Two-Dimensional Magnetotransport in the Extreme Quantum Limit". In: *Physical Review Letters* 48, pp. 1559–1562. DOI: 10.1103/PhysRevLett.48.1559.

Tsukada, Masaru (1976). "On the Tail States of the Landau Subbands in MOS Structures under Strong Magnetic Field". In: *Journal of the Physical Society of Japan* 41, pp. 1466–1472. DOI: 10.1143/JPSJ.41.1466.

Ueda, Hiroshi, Andrej Gendiar, and Tomotoshi Nishino (2010). "A Classical Background for the Wave Function Prediction in the Infinite System Density Matrix Renormalization Group Method". In: *Journal of the Physical Society of Japan* 79, p. 044001. DOI: 10.1143/JPSJ.79.044001.

Ueda, Hiroshi and Isao Maruyama (Jan. 2012). "Application of Uniform Matrix Product State to Quantum Phase Transition with a Periodicity Change". In: *Journal of the Physical Society of Japan* 81.Suppl.B, SB065. DOI: 10.1143/JPSJS.81SB.SB065.

Ueda, Hiroshi, Tomotoshi Nishino, and Koichi Kusakabe (2008). "Two-Site Shift Product Wave Function Renormalization Group Method Applied to Quantum Systems". In: *Journal of the Physical Society of Japan* 77. DOI: 10.1143/JPSJ.77.114002.

Verstraete, F. and J. I. Cirac (2004). "Renormalization Algorithms for Quantum-Many Body Systems in Two and Higher Dimensions". In: arXiv: cond-mat/0407066.

Verstraete, F. and J. I. Cirac (2006). "Matrix Product States Represent Ground States Faithfully". In: *Physical Review B - Condensed Matter and Materials Physics* 73, p. 094423. DOI: 10.1103/PhysRevB.73.094423.

Verstraete, F., J. J. García-Ripoll, and J. I. Cirac (2004). "Matrix Product Density Operators: Simulation of Finite-Temperature and Dissipative Systems". In: *Physical Review Letters* 93, p. 207204. DOI: 10.1103/PhysRevLett.93.207204.

Verstraete, Frank, V. Murg, and J I Cirac (Mar. 2008). "Matrix Product States, Projected Entangled Pair States, and Variational Renormalization Group Methods for Quantum Spin Systems". In: *Advances in Physics* 57.2, pp. 143–224. DOI: 10.1080/14789940801912366. arXiv: 0907.2796.

Vidal, G. (2007). "Entanglement Renormalization". In: *Physical Review Letters* 99, p. 220405. DOI: 10.1103/PhysRevLett.99.220405.

Vidal, Guifré (2003). "Efficient Classical Simulation of Slightly Entangled Quantum Computations". In: *Physical Review Letters* 91, p. 147902. DOI: 10.1103/PhysRevLett.91.147902.

Vidal, Guifré (2004). "Efficient Simulation of One-Dimensional Quantum Many-Body Systems". In: *Physical Review Letters* 93, p. 040502. DOI: 10.1103/PhysRevLett.93.040502.

Vidal, Guifre (2010). "Entanglement Renormalization: An Introduction". In: *Understanding Quantum Phase Transitions*. Boca Raton, FL, U.S.A.: CRC Press, pp. 115–137. arXiv: cond-mat/0512165.

Wannier, G.H. (1978). "A Result Not Dependent on Rationality for Bloch Electrons in a Magnetic Field". In: *Physica Status Solidi B* 88, pp. 757–765. DOI: 10.1002/pssb.2220880243.

Wei, H. P., D. C. Tsui, M. A. Paalanen, and A. M. M. Pruisken (1988). "Experiments on Delocalization and University in the Integral Quantum Hall Effect". In: *Physical Review Letters* 61, pp. 1294–1296. DOI: 10.1103/PhysRevLett.61.1294.

Weichselbaum, Andreas (2012). "Non-Abelian Symmetries in Tensor Networks: A Quantum Symmetry Space Approach". In: *Annals of Physics* 327, pp. 2972–3047. DOI: 10.1016/j.aop.2012.07.009.

Wen, X G (1989). "Vacuum Degeneracy of Chiral Spin States in Compactified Space". In: *Physical Review B* 40, 7387(R). DOI: 10.1103/PhysRevB.40.7387.

Wen, X. G. (1990a). "Chiral Luttinger Liquid and the Edge Excitations in the Fractional Quantum Hall States". In: *Physical Review B* 41, p. 12838. DOI: 10.1103/PhysRevB.41.12838.

Wen, X. G. (1991). "Non-Abelian Statistics in the Fractional Quantum Hall States". In: *Physical Review Letters* 66, pp. 802–805. DOI: 10.1103/PhysRevLett.66.802.

Wen, Xiao-gang (1990b). "Topological Orders in Rigid States". In: *International Journal of Modern Physics B* 04.02, pp. 239–271. DOI: 10.1142/S0217979290000139. arXiv: 1011.1669v3.

Wen, Xiao-Gang (1992). "Theory of the Edge States in Fractional Quantum Hall Effects". In: *International Journal of Modern Physics B* 6, pp. 1711–1762. DOI: 10.1142/S0217979292000840.

Wen, Xiao-Gang (Dec. 2017). "Colloquium : Zoo of Quantum-Topological Phases of Matter". In: *Reviews of Modern Physics* 89.4, p. 041004. DOI: 10.1103/RevModPhys.89.041004.

Wen, Xiao-Gang and Yong-Shi Wu (1993). "Transitions between the Quantum Hall States and Insulators Induced by Periodic Potentials". In: *Physical Review Letters* 70, pp. 1501–1504. DOI: 10.1103/PhysRevLett.70.1501.

White, Steven (2005). "Density Matrix Renormalization Group Algorithms with a Single Center Site". In: *Physical Review B* 72, p. 180403. DOI: 10.1103/PhysRevB.72.180403.

White, Steven R. (1992). "Density Matrix Formulation for Quantum Renormalization Groups". In: *Physical Review Letters* 69, pp. 2863–2866. DOI: 10.1103/PhysRevLett.69.2863.

White, Steven R (1993). "Density-Matrix Algorithms for Quantum Renormalization Groups". In: *Physical Review B* 48, pp. 10345–10356. DOI: 10.1103/PhysRevB.48.10345.

White, Steven R. and David A. Huse (1993). "Numerical Renormalization-Group Study of Low-Lying Eigenstates of the Antiferromagnetic $S = 1$ Heisenberg Chain". In: *Physical Review B* 48, pp. 3844–3852. DOI: 10.1103/PhysRevB.48.3844.

Wolf, Michael M, Gerardo Ortiz, Frank Verstraete, and J Ignacio Cirac (2006). "Quantum Phase Transitions in Matrix Product Systems". In: *Physical Review Letters* 97.11. DOI: 10.1103/PhysRevLett.97.110403. arXiv: cond-mat/0512180.

Ye, Jinwu and Subir Sachdev (1998). "Coulomb Interactions at Quantum Hall Critical Points of Systems in a Periodic Potential". In: *Physical Review Letters* 80, pp. 5409–5412. DOI: 10.1103/PhysRevLett.80.5409.

Zaletel, Michael P, Roger S K Mong, and Frank Pollmann (2013). "Topological Characterization of Fractional Quantum Hall Ground States from Microscopic Hamiltonians". In: *Physical Review Letters* 110, p. 236801. DOI: 10.1103/PhysRevLett.110.236801.

Zaletel, Michael P, Roger S K Mong, and Frank Pollmann (2014). "Flux Insertion, Entanglement, and Quantized Responses". In: *Journal of Statistical Mechanics: Theory and Experiment* 2014, P10007. DOI: 10.1088/1742-5468/2014/10/P10007.

Zhu, Wei, Xiao Chen, Yin-Chen He, and William Witczak-Krempa (Nov. 2018). "Entanglement Signatures of Emergent Dirac Fermions: Kagome Spin Liquid and Quantum Criticality". In: *Science Advances* 4.11, eaat5535. DOI: 10.1126/sciadv.aat5535.